Explicit Crack Modeling based Approach for Structural Integrity Assessment of Brittle and Quasi-Brittle Structures

A DISSERTATION
SUBMITTED TO THE FACULTY OF
UNIVERSITY OF MINNESOTA
BY

Gyanender P. Singh

IN PARTIAL FULFILLMENT OF THE REQUIREMENTS
FOR THE DEGREE OF
DOCTOR OF PHILOSOPHY IN MECHANICAL ENGINEERING

Dr. Alex Fok and Dr. Susan Mantell

February 2015

Acknowledgements

I am indebted to my adviser Dr. Alex Fok for giving me the opportunity to work on this project and for his continuous encouragement, guidance and support. I am very grateful to him for the numerous hours he spent with me discussing the various aspects of this work and showing the right directions to move forward. I am also very much indebted to my adviser Dr. Susan Mantell for her continuous guidance and support throughout my stay at University of Minnesota.

I am thankful to all the present and past group members who made my stay a joyful experience. I am especially thankful to Dr. Haiyan Li who very patiently helped me in learning several aspects of the computational and experimental work. Dr. Jianying Li helped me at various stages of this work and guided me to move forward from "stuck-up" situations; I am very thankful to him.

This research was funded by the Department of Energy Office of Nuclear Energy's Nuclear Energy University Programs (NEUP).

I would like to acknowledge Mr. Michael Weston for making fixtures which were used in the experiments required for this work.

I am grateful to my family, particularly my parents, who have been a source of great support and encouragement throughout my life.

Abstract

There is considerable variation in the fracture properties of brittle and quasi-brittle materials. Due to this large variation, probabilistic models are employed for estimating failure of brittle components/structures. However, due to limitations and shortcomings in the models, the predictions are not accurate. The shortcomings include: inability to handle stress concentrations, dependence of empirical constants on loading conditions, incorrect size-effect predictions and limited applications of the model. Although higher design margins can accommodate the inaccuracy in predictions, the cost of manufacturing increases. The work presented herein is directed towards addressing these issues.

An approach based on explicit crack modeling (ECM) for accurately estimating failure in brittle/quasi-brittle components and structures is presented. Factors which govern fracture in a structure (fracture energy, strength of the material, damage behavior of the material, heterogeneity in the material microstructure) are incorporated in the ECM approach. The approach was validated by predicting the failure probability of L-shaped specimens at varying load levels followed by comparison of the predictions with published data. The study showed that the predictions from the ECM approach were not only in good agreement with the published data but were also more accurate than the Weibull model based predictions.

The ECM approach can also predict size effect—the dependence of fracture properties and their statistical variation on the size of the specimen. This capability was

demonstrated through failure prediction of specimens in tensile and flexural tests. Specimens of different sizes were considered and the predicted fracture properties were in good agreement with those obtained experimentally.

The ECM approach for estimating failure of components/structures subjected to complex physical conditions was illustrated through the failure estimation of nuclear reactor graphite components. For modeling stresses in the graphite components subjected to high temperature and neutron irradiation, a constitutive model for evaluating the stresses was constructed and implemented through a user material (UMAT) subroutine in finite element software Abaqus. UMAT was integrated with Extended Finite Element (XFEM) technique for modeling irradiation-induced failure of the components under in-reactor conditions. Component lifetime as well as crack initiation and propagation details were predicted. This type of detailed failure information has the potential to improve design guidelines and standards of brittle components/structures.

Table of Contents

LIST OF TABLES ..... **vi**

LIST OF FIGURES ..... **vii**

NOMENCLATURE ..... **xi**

1. INTRODUCTION **1**

1.1 MOTIVATION 1
1.2 OBJECTIVES AND SCOPE OF RESEARCH 2
1.3 REFERENCES 4

2. BACKGROUND **5**

2.1 PROBABILISTIC APPROACH FOR FAILURE PREDICTION 5
2.2 MATERIAL HETEROGENEITY 14
2.3 REFERENCES 17

3. THE WEIBULL MODEL FOR ESTIMATING FAILURE IN BRITTLE MATERIALS **20**

3.1 WEIBULL MODEL AND WEAKEST LINK THEORY 20
3.2 LIMITATIONS OF WEIBULL PROBABILISTIC MODEL 23
3.3 EXPLICIT CRACK MODELING APPROACH 26
3.4 REFERENCES 28

4. ASSESSMENT OF EXPLICIT CRACK MODELING APPROACH **29**

4.1 EXPLICIT CRACK MODELING BASED APPROACH AND COMPARISON WITH THE WEIBULL MODEL 29
4.2 REFERENCES 37

5. EXPLICIT CRACK MODELING APPROACH FOR PREDICTING SIZE EFFECT **38**

5.1 EARLIER STUDIES ON SIZE EFFECT 38
5.2 METHOD 41
5.3 RESULTS 47
5.4 DISCUSSION AND CONCLUSIONS 55
5.5 REFERENCES 58

6. ESTIMATING STRESSES IN THE VHTR COMPONENTS **60**

6.1 VERY HIGH TEMPERATURE REACTOR SYSTEM 60
6.2 LIMITATIONS OF NUCLEAR GRAPHITE 62
6.3 ASSESSING STRUCTURAL INTEGRITY OF GRAPHITE BRICKS 63
6.4 CONSTITUTIVE MODEL FOR GRAPHITE AND ITS IMPLEMENTATION IN FEM 67
6.5 MODELING RESIDUAL STRESSES IN VHTR GRAPHITE COMPONENTS 72
6.6 REFERENCES 81

7. FAILURE PREDICTIONS OF THE VHTR COMPONENTS **83**

7.1 MONTE CARLO 2D FAILURE ANALYSIS OF A CYLINDRICAL GRAPHITE BRICK 84
7.2 MONTE CARLO 3D FAILURE ANALYSIS OF A CYLINDRICAL GRAPHITE BRICK 93
7.3 MONTE CARLO 2D FAILURE ANALYSIS OF A PRISMATIC REFLECTOR BRICK 102
7.4 MONTE CARLO 3D FAILURE ANALYSIS OF A PRISMATIC REFLECTOR BRICK 110
7.5 FAILURE ESTIMATION OF BRITISH AGR REACTORS 119
7.6 REFERENCES 124

8. CONCLUSIONS **126**

8.1 CONCLUDING REMARKS 126

8.2 CONCLUSIONS 128
8.3 RECOMMENDATIONS 130

BIBLIOGRAPHY 131

APPENDIX A 137

APPENDIX B 138

B.1 MODELING CRACK PROPAGATION USING XFEM 139
B.2 ASSESSING THE VIABILITY OF XFEM 143
Mesh Sensitivity of Crack Propagation Simulation using 2D XFEM 144
B.3 RESULTS AND CONCLUSIONS 147
B.4 REFERENCES 157

List of Tables

Table 4.1: Weibull model parameters for PPEA graphite determined through calibration. 31
Table 4.2: Parameters of the material determined through calibration for explicit crack modeling approach. 34
Table 5.1: Summary of tests used to calibrate the intrinsic fracture properties and those for which predictions were made for bulk behavior. 43
Table 5.2: Fracture properties and associated statistical parameters of the material. 43
Table 5.3: Dimensions of the un-notched graphite specimens subjected to tension. 45
Table 5.4: Dimensions of the un-notched graphite specimens subjected to three-point bending. 45
Table 5.5: Dimensions of the notched graphite specimens subjected to three-point bending. 45
Table 5.6: Details of mesh of the specimen models for tensile test. 45
Table 5.7: Details of mesh of the specimen models for three-point bend test 46
Table 5.8: The peak load, tensile strength and corresponding Weibull modulus for different groups of specimen models subjected to the tensile test. 49
Table 5.9: The peak load, flexural strength and corresponding Weibull modulus for different groups of un-notched specimen models subjected to the three-point-bending test. 50
Table 5.10: Peak load, critical stress intensity factor and corresponding Weibull modulus for different groups of notched specimen models subjected to three-point bending test. 53
Table 7.1: The mean value and Weibull Modulus for strength and critical stress intensity factor. 87
Table 7.2: The predicted times at which a crack initiated, penetrated through half of the thickness and penetrated through all the thickness in the brick. 90
Table 7.3: Fracture toughness, strength and the corresponding crack initiation time for all specimens. 100
Table 7.4: The predicted times at which crack initiates in the brick. 108
Table 7.5: Fracture toughness, strength and the corresponding crack initiation time for all specimens. 116

List of Figures

Figure 2.1: Image showing the heterogeneity in the microstructure of graphite. 14
Figure 3.1: Dimensions of the L-shaped specimen (mm) (source: [9] and a specimen under loading. 23
Figure 3.2: Comparison of Weibull moduli obtained for L-shaped specimen with different radii of curvature (Source: [9]). 24
Figure 4.1: L-shaped specimen under tensile loading. 31
Figure 4.2: Meshed model of the L-shaped specimen (r=4mm) with heterogeneous elements embedded in it..... 32
Figure 4.3: Traction separation curve and the associated fracture parameters. 33
Figure 4.4: Cracked model of a L-shaped specimen (Scale factor: 10). 36
Figure 4.5: Comparison of the predictions of failure probability from the Weibull model, explicit crack modeling approach and experimental data. 36
Figure 5.1: Traction separation curve and the associated fracture parameters. 42
Figure 5.2: Finite element model of the largest specimen under tension. 45
Figure 5.3: The meshed model of a Group-I un-notched specimen under three-point bending. 46
Figure 5.4: A fractured specimen model after three-point bend test. 48
Figure 5.5: Predicted load-displacement curves of the notched specimens under 3-point bending (upper); Load-displacement curves determined experimentally (Li et al. [4]) (lower). 49
Figure 5.6: Variation of the mean tensile strength with the size of the specimens..... 50
Figure 5.7: Variation of the predicted Weibull modulus for tensile strength distribution with the size of the specimens. 51
Figure 5.8: Variation of the experimental Weibull modulus for the tensile strength with the volume of the specimen (evaluated from data given by Brocklehurst [1]). 51
Figure 5.9: Variation of the mean flexural strength with the volume of the specimens... 52
Figure 5.10: Variation of the predicted Weibull modulus for the flexural strength distribution with the size of the specimens. 53
Figure 5.11: Comparison of variation of the mean critical stress intensity factor with the size of the specimens. 54
Figure 5.12: Variation of the predicted Weibull modulus for the critical stress intensity factor distribution with the size of the specimen. 54
Figure 5.13: Schematic diagram showing that the defects in a large specimen (top) span over a larger range of size in comparison to smaller specimens (bottom)..... 56
Figure 5.14: As the number of dice increases the variability in the random variable 'sum of dice' decreases. 57
Figure 6.1: Conceptual design of a GT-MHR core..... 61
Figure 6.2: Lower core internal of HTR-10 (a Pebble Bed test reactor located in China). 62
Figure 6.3: Meshed model of the graphite cylinder section..... 69
Figure 6.4: Variation of irradiation dose (10^{20} n/cm^2) in the cylindrical section with the radial distance after 30 years..... 70

Figure 6.5: Hoop stress distribution after 15 years. 70
Figure 6.6: Axial stress distribution after 15 years. 71
Figure 6.7: Hoop stresses versus time at the inner and outer surfaces. 71
Figure 6.8: Axial stresses versus time at the inner and outer surfaces. 72
Figure 6.9: A full model (top) and a meshed quarter model (bottom) of the HTR graphite brick. 73
Figure 6.10: Assumed distribution of irradiation dose (10^{20} n/cm^2) in the HTR graphite brick at 17th year. 74
Figure 6.11: Assumed variation of dimensional change strain with neutron dose at different temperatures. 75
Figure 6.12: Assumed variation of temperature (°C) in the HTR graphite brick with distance from the core. 76
Figure 6.13: Radial stress distribution after 30 years. 77
Figure 6.14: Hoop stress distribution after 30 years. 77
Figure 6.15: Axial stress distribution after 30 years. 78
Figure 6.16: Maximum principal stress distribution after 30 years. 78
Figure 6.17: Locations of two points of interest (node A and node B). 79
Figure 6.18: Variation of radial stress (S11) with time at two locations. 79
Figure 6.19: Variation of hoop stress (S22) with time at two locations. 80
Figure 6.20: Variation of axial stress (S33) with time at two locations. 80
Figure 7.1: Cross-sectional view of a graphite brick (hollow cylinder). 84
Figure 7.2: Brick model divided into enriched and non-enriched regions. 85
Figure 7.3: Meshed model of the graphite brick (left); boundary conditions on the brick (right). 86
Figure 7.4: Variation of temperature with distance from brick center (top); variation of irradiation dose (x10^{20}n/cm^2) with radial distance at the end of 30 years (bottom). 86
Figure 7.5: Distribution of the maximum principal stress at the end of 5, 10, 15, 20, 25 and 30 years shown in pictures numbered 1, 2, 3, 4, 5 and 6 respectively for case 1 (σ_f = 14.3 MPa, G_{IC} = 92.6 J/m^2). 88
Figure 7.6: Variation of hoop stress with time at the inner and outer surfaces of the brick for specimen 1 (σ_f = 14.3 MPa, G_{IC} = 92.6 J/m^2). 89
Figure 7.7: Crack propagation with time through the thickness of the cylindrical graphite brick model. 90
Figure 7.8: Failure probability of ATR-2E graphite brick vs. time. 92
Figure 7.9: Cylindrical graphite brick model. 93
Figure 7.10: XFEM and non-XFEM domains of brick model. 94
Figure 7.11: Mesh of 3D FE model (left); boundary conditions on the brick (right). 94
Figure 7.12: Variation of temperature with radial distance from brick center (left); variation of irradiation dose (x10^{20}n/cm^2) with radial distance at the end of 20 years (right). 95
Figure 7.13: Variation of strength with irradiation dose [3]. 96
Figure 7.14: Distribution of maximum principal stress at the end of 5, 10, 15, 20, 25 and 30 years, shown in pictures numbered 1, 2, 3, 4, 5 and 6, respectively for Case 1 (σ_f = 13.9 MPa, G_{IC} = 102.5 J/m^2). 97

Figure 7.15: Variation of hoop stress with time at the inner and outer surfaces of the brick for Specimen 1 (σ_f = 13.9 MPa, G_{IC} = 102.5 J/m^2)..... 98
Figure 7.16: Crack propagation with time through a graphite brick model..... 99
Figure 7.17: Failure probability of ATR-2E graphite brick vs. time..... 101
Figure 7.18: Location and dimensional details of prismatic reflector brick considered for failure analysis (source: [2]). 103
Figure 7.19: Prismatic reactor core brick model..... 103
Figure 7.20: Brick model divided into enriched and non-enriched regions. 104
Figure 7.21: Meshed model of the prismatic brick (left); boundary conditions on the brick (right). 104
Figure 7.22: Temperature distribution (left) and irradiation dose distribution (x10^{20}n/cm^2) (right) in the prismatic reactor core brick at the end of 6 years..... 105
Figure 7.23: Distribution of maximum principal stress with ATR-2E graphite at the end of 2, 5, 8, 11, 11.6 and 17 years shown in pictures numbered 1, 2, 3, 4, 5 and 6 respectively for case 1 (σ_f = 15.1 MPa, G_{IC} = 110.3 J/m^2). 106
Figure 7.24: Variation of maximum principal stress with time at the inner and outer surfaces of the brick for specimen 1 (σ_f = 15.1 MPa, G_{IC} = 110.3 J/m^2)..... 107
Figure 7.25: Crack propagation with time through the thickness of a graphite brick model..... 108
Figure 7.26: Failure probability of ATR-2E graphite brick vs. time..... 109
Figure 7.27: A Prismatic reactor core brick model..... 110
Figure 7.28: Mesh of 3D FE model (left) and boundary conditions on the brick (right). 111
Figure 7.29: Temperature distribution (left) and irradiation dose distribution (x10^{20} n/cm^2) (right) in the prismatic reactor core brick at the end of 6 years. 111
Figure 7.30: Variation of strength with irradiation dose [3]..... 112
Figure 7.31: Distribution of maximum principal stress at the end of 1.5, 3.0, 4.5, 6.0, 7.5 and 9.6 years, shown in pictures numbered 1, 2, 3, 4, 5 and 6, respectively for Case 7 (σ_f = 11.7 MPa, G_{IC} = 106.93 J/m^2). 113
Figure 7.32: Variation of maximum principal stress with time at the inner and outer surfaces of the brick for Specimen 7 (σ_f = 11.7 MPa, G_{IC} = 106.93 J/m^2). 114
Figure 7.33: Crack propagation with time through a graphite brick model..... 114
Figure 7.34: Crack on the outer edge of the graphite brick model (Specimen 28)..... 115
Figure 7.35: Failure probability of ATR-2E graphite brick vs. time..... 117
Figure 7.36: AGR reflector brick model..... 120
Figure 7.37: Meshed model of the AGR reflector brick with boundary conditions..... 121
Figure 7.38: Temperature distribution (left) and irradiation dose distribution (x10^{20}n/cm^2) (right) in the AGR reactor core brick at the end of 15 years. 121
Figure 7.39: Maximum principal stress distribution in the AGR brick after 4 years of operation. 122
Figure 7.40: Maximum principal stress distribution in the AGR brick after 18 years of operation. 122
Figure 7.41: Occurrence of crack at the keyway in the AGR brick after 18 years of operation. 123

Figure 7.42: Crack path after 22 years of reactor operation. 124

Nomenclature

Latin Symbols

a	Crack length	mm
C	Calibration	-
D	Damage factor	-
D	Stiffness (matrix) of material	N/m^2
Ď	Mean stiffness in current increment	N/m^2
dV	Infinitesimal volume	m^3
Δ**D**	Increment in stiffness	N/m^2
E	Dynamic Young's modulus	N/m^2
E_C	Creep Young's modulus	N/m^2
f	Filler particle size	-
FEM	Finite element method	-
G	Fracture energy	J/m^2
G_{IC}	Critical fracture energy	J/m^2
k	Filler particle count number	-
K	Stress intensity factor	$N/m^{3/2}$
k_B	Normalized Batdorf crack density coefficient	m^{-3}
K_{IC}	Critical stress intensity factor	$N/m^{3/2}$
m	Weibull modulus (shape parameter)	-
m_G	Weibull modulus corresponding to critical fracture energy	-
m_σ	Weibull modulus corresponding to strength	-
N	Number of defects	-
N	Number of elements in the material	-
n	Number of neutrons	-
n_f	Number of filler particles	-
P	Prediction	-
P_f	Failure probability	-
P_s	Survival probability	-
SDV5	Solution dependent variable which stores the value of irradiation dose	$x10^{24}neutrons/m^2$

SDV8	Solution dependent variable which stores the value of temperature	°C
S_o	Mean pore size	mm
T	Temperature	°C
t	Time	years
V	Volume	-
w	Width of specimen	mm

Greek Symbols

$\boldsymbol{\sigma}$	Stress	N/m^2
σ_f	Strength of material	N/m^2
σ_{th}	Threshold stress	N/m^2
σ_o	Weibull scale parameter	N/m^2
σ_{1eq}	Equivalent uniaxial stress according to failure criterion	N/m^2
$\sigma_{1eq,max}$	Maximum equivalent uniaxial stress over the unit sphere in 3D stress space	N/m^2
σ_{1c}	Mode 1 far-field strength of a flaw	N/m^2
$\boldsymbol{\varepsilon}^{e}$	Elastic strain	-
$\boldsymbol{\varepsilon}^{pc}$	Primary creep strain	-
$\boldsymbol{\varepsilon}^{sc}$	Secondary creep strain	-
$\boldsymbol{\varepsilon}^{th}$	Thermal strain	-
$\boldsymbol{\varepsilon}^{dc}$	Dimensional change strain	-
$\boldsymbol{\varepsilon}^{ith}$	Interaction thermal strain	-
$\boldsymbol{\varepsilon}^{idc}$	Interaction dimensional change strain	-
$\Delta\boldsymbol{\varepsilon}$	Sum of all strains	-
Σ	Stress volume integral	-
γ	Neutron irradiation	$x10^{24}neutrons/m^2$
Ω	Area of solid angle on unit sphere in 3D stress space for which $\sigma_{1eq} \geq \sigma_{1c}$	-
η	Crack density function	m^{-3}
Γ	Gamma function	-

ρ	Mean defect density	m^{-3}
∞	Infinity	-
$\Delta\boldsymbol{\sigma}$	Increment in stress	N/m^2

1. INTRODUCTION

1.1 MOTIVATION

Brittle and quasi-brittle materials include, but are not limited to, ceramics, concrete, graphite and cementitious composite. These materials are used in space shuttle tiles, high temperature glass windows, fuel cells, electronics, automobile components, biomechanics applications, building structures, nuclear reactors and so on. In several applications these structures and components are subjected to severe loading and environmental conditions, and the structural integrity is put to test.

The failure of brittle/quasi-brittle components and structures is dependent on their fracture properties. Due to irregularity in the microstructure, there is variation in the fracture properties of the material. Deterministic approaches to predict failure do not work well and probabilistic approaches are used [1]. Typically, stresses are predicted using a suitable constitutive model which defines the relationship between the stresses and strains, followed by employing a statistical model to evaluate the failure probability based on the stress distribution. The Weibull model is one of the most extensively used models to estimate the failure probability in brittle and quasi-brittle components/structures. However, the Weibull model has its own limitations and shortcomings: it does not handle stress concentrations well and overestimates the failure probability; and the Weibull modulus which should be a constant has been found to depend on the stress gradient [2] [3]. To accommodate the uncertainties arising due to inaccuracy in the predictions, higher design margins must be taken. The resulting design

margins increase the cost of manufacturing and the compromised design may affect the efficiency and performance of the components/structures while in-operation/in-service.

1.2 OBJECTIVES AND SCOPE OF RESEARCH

An approach based on explicit crack modeling (ECM) is presented herein for estimating failure in brittle and quasi-brittle components/structures. The approach incorporates the factors which govern fracture (fracture energy, strength of the material, damage behavior of the material and heterogeneity in the material microstructure) at a fundamental level. Because the fracture governing factors are included in the ECM approach, it has the capability to estimate failure more accurately than currently existing probabilistic models. In addition the ECM approach can predict the statistical variation in fracture properties and the effect of specimen size on the fracture properties.

This dissertation is divided into eight chapters. A review of the prominent models for estimating failure in brittle/quasi-brittle components and structures is presented in chapter 2. This chapter presents the current state of the art in probabilistic modeling of failure including a review of the Weibull model, Bartdorf model, Evans model and Burchell model. The Weibull model is the most extensively used model and is based on the weakest-link theory. The weakest-link theory states that the strength of a chain cannot be greater than the strength of the weakest link in the chain. Since, in brittle materials, failure can be assumed to be a result of unstable propagation of the most critical flaw, the weakest-link theory can be used to model the failure probability of brittle materials. Chapter 3 presents the formulation of the Weibull model based on the weakest-link theory. The shortcomings of the Weibull model, factors which lead to these shortcomings

and the subsequent implications are presented in this chapter. The chapter also introduces the reader to the ECM approach.

Chapter 4 presents the validation of the ECM approach. The validation was performed by estimating the failure probabilities of L-shaped specimens subjected to tensile loading. The failure probability predictions obtained through the ECM approach were compared with 1) the failure probabilities obtained from the Weibull model and also with 2) the failure probabilities determined from the published experimental data. The results established greater accuracy and capability of the ECM approach over the Weibull probabilistic model.

It has been found that the fracture properties and variation in these properties depend on the size of specimen used in the standard mechanical tests. This phenomenon is termed as “size effect”. ECM was employed to predict the size effect. Details of the study are presented in chapter 5.

The ECM approach for predicting failure of components/structures subjected to complex physical conditions was illustrated through a failure analysis of nuclear reactor core graphite bricks. The work is presented in chapters 6 and 7. The work involved implementation of the constitutive model of graphite in commercial FE software Abaqus for modeling stresses in the bricks. Stresses were determined under in-reactor conditions, i.e., high temperature and neutron irradiation. The constitutive model was implemented through the user-material subroutine UMAT. For modeling fracture in the graphite bricks, UMAT was used in conjunction with the Extended Finite Element Method (XFEM) and the failure probability was determined based on the fracture simulation

results. Chapter 8 presents the conclusions from the work and recommendations for future work.

1.3 REFERENCES

1. N.N. Nemeth and R.L. Bratton, Statistical Models for Fracture Relevant to Nuclear-Grade Graphite: Review and Recommendations, NASA/TM-2011-215805.
2. B.C. Mitchell, J. Smart, S.L. Fok and B.J. Marsden, The Mechanical Testing of Nuclear Graphite, Journal of Nuclear Materials, 322, 126-137, 2003.
3. H. Li and A.S.L. Fok, An Analytical Study on the Effects of Strain Gradient on the Fracture Statistics of the Quasi-Brittle Materials, Journal of Nuclear Materials, 394, 2009, 136-143.
4. J.E. Brocklehurst, Fracture in Polycrystalline Graphite, Chemistry and Physics of Carbon, New York, NY, 13, 146–272, 1977.

2. BACKGROUND

As science and technology is advancing, materials are being used in more than ever challenging environment and operating conditions. This advancement has led not only to the development of new materials which are suited for these applications but has also given rise to a need to know more accurately about the performance of materials which have been in use for several decades. Brittle and quasi-brittle materials are being used for practically unlimited number of applications ranging from cooking appliances to computer chips to biomedical devices. For reliable usage of the devices, components and structures made of these materials, it is important to assess their structural integrity.

2.1 PROBABILISTIC APPROACH FOR FAILURE PREDICTION

The failure of a component/structure caused by fracture is governed by the stress state and the fracture properties of the material. When the stresses exceed the strength of material cracks develop and start propagating, ultimately leading to a catastrophic failure of the component/structure. Thus, a conservative estimation of the failure time can be made by calculating the time at which the stresses exceed the strength of the material. However, this deterministic approach does not work well for brittle and quasi-brittle components/structures because the fracture properties of these materials (strength, fracture toughness) vary greatly [1]. Therefore, probabilistic approaches are employed to characterize the failure of brittle and quasi-brittle components/structures.

The weakest-link theory is the basis of several statistical models developed to predict and explain failure in the brittle and quasi-brittle structures. The theory represents a material through a chain made of individual links joined together in series. Since

breakage of a single link is sufficient to break the entire chain, the chain is only as strong as its weakest link. This concept is analogous to the failure of a brittle component/structure in which the weakest microcrack extends and propagates catastrophically leading to failure of the entire component/structure. Thus, according to the weakest link theory a structure is only as strong as the weakest flaw present in the structure.

The most extensively used model based on the weakest-link theory is the Weibull model [2]. A brittle structure contains flaws or microcracks distributed randomly throughout its volume. When the structure is subjected to mechanical loads a critically-loaded microcrack causes failure of the structure. The critically-loaded microcrack is oriented in such a way that the stress level experienced by the crack exceeds its critical strength. It may be noted here that this critically-loaded crack may not necessarily lie in the region experiencing maximum stress. Weibull assumed a power function to describe the distribution of these critically loaded microcracks in the structure. The details of formulation of the Weibull model based on the weakest-link theory are presented in chapter 3; here only a brief review is presented. The model predicts the failure probability of a structure as:

$$P_f = 1 - \exp\left[-\int_V \left\langle \frac{\sigma - \sigma_{th}}{\sigma_o} \right\rangle^m \frac{dV}{v}\right]$$

where σ is the local stress, σ_{th} is the threshold stress below which no fracture will occur in the structure, σ_o is the scale parameter and m is the shape parameter of the distribution. Generally the parameter σ_{th} is ignored, thus reducing the number of parameters that need

to be determined empirically, and also leading to a conservative estimation of the failure probability which is expressed as:

$$P_f = 1 - \exp\left[-\int_V \left\langle \frac{\sigma}{\sigma_o} \right\rangle^m \frac{dV}{v}\right]$$

Although stresses can be calculated analytically for simple geometries, for most cases stresses have to be determined numerically. The evaluated stress distribution is then used to calculate the failure probability through the Weibull model. This is a popular approach and is extensively used for failure probability predictions in various fields of engineering including aerospace, civil, nuclear and electrical engineering. However, the Weibull model has its shortcomings; one of the shortcomings is that the so-called Weibull modulus, which is considered a material property, is actually dependent on the stress gradient [3].

Mitchell et al. [3] conducted tensile tests on L-shaped specimens to understand the effect of strain-gradient on the Weibull modulus. The specimens were taken from different billets of graphite and also from different sections within a billet. It was found that the specimens with sharp corner (radius ≈ 0 mm) failed at lower load and exhibited a higher Weibull modulus (59). For other radii (1 mm, 2 mm and 4 mm), the Weibull moduli were found to be much lower (29, 21 and 26). Another criticism of the Weibull model is that the model does not handle stress concentrations well and overestimates the failure probability of structures with high stress concentrations.

When Weibull proposed the model he also gave a procedure to calculate probability of failure for multiaxial stress states: averaging the tensile stresses in all directions and using the average stress value to evaluate the failure probability [2] [4].

However, this procedure has been questioned by some investigators. The Batdorf model [5] [6] is another prominent model for failure estimation of brittle structures and is also based on the weakest-link theory. The model assumes that the microcracks are randomly oriented, do not interact with each other, are planar and can be of varying size. Unlike the Weibull model, the Batdorf model plausibly incorporates multiaxial stress states and describes the physical mechanism responsible for the failure of the material. The failure probability of a component/structure is given as:

$$P_f = 1 - \exp\left\{ - \int_V \left[\int_0^{\sigma_{1eq,max}} \frac{\Omega(\boldsymbol{\sigma}, \sigma_{1c})}{4\pi} \frac{d\eta}{d\sigma_{1c}} d\sigma_{1c} \right] dV \right\}$$

where σ_{1c} is the mode 1 crack strength, η is the crack density function, $\boldsymbol{\sigma}$ represents the multiaxial stress state, V is the volume of the component, σ_{1eq} is the mode 1 equivalent stress which depends on the failure criterion chosen, the stress state and orientation of the crack and $\sigma_{1eq,max}$ represents the maximum equivalent stress that a randomly oriented crack can experience. The integrand in the above expression for failure probability is a product of two terms. The term $\Delta V \frac{d\eta}{d\sigma_{1c}} d\sigma_{1c}$ represents the probability of the existence of a crack having strength between σ_{1c} and $\sigma_{1c}+d\sigma_{1c}$. The other term $\frac{\Omega(\boldsymbol{\sigma},\sigma_{1c})}{4\pi}$ represents the probability that the existing crack is oriented such that the effective stress σ_{1eq} is greater than the critical strength σ_{1c} of the crack. The crack density function η is given as:

$$\eta = \frac{k_B \sigma_{1c}^m}{\sigma_o^m}$$

where k_B is the normalized Batdorf crack density coefficient and is a function of the mixed-mode fracture criterion chosen and m is the Weibull modulus. The parameters k_B and m are determined empirically. The Batdorf model has been implemented in

CARES/Life (Ceramics Analysis and Reliability Evaluation of Structures/Life) software developed by NASA for performing reliability analysis [7]. The Batdorf model has also been applied for predicting fracture in composite materials [8].

Another statistical model for predicting brittle fracture is the Evans model [9]. The model is based on the Poisson postulates and the weakest-link theory. The failure probability predicted by the model is given as:

$$P_f = 1 - \exp\left[-\int_V \int_0^{\sigma} g(\sigma) d\sigma \, dV\right]$$

where V is the volume of the component, σ is the observed fracture strength and g(σ)dσ is the number of flaws in a unit volume having strength between σ and σ+dσ. The function g(σ) is obtained by fitting polynomials to the experimental data as has been described by Matthews et al. [10]. Chao et al. [11] have shown the predictions from the Evans model and the Batdorf model to be the same. Furgiuele et al. [12] have shown analytically that the two models are in fact identical.

Freudenthal [13] proposed a fracture model purely based on probabilistic reasoning that fracture happens due to the presence of a critical number of defects. The model, named as the Uniform Defect model, assumes that defects are uniformly distributed over the volume of the material and that their occurrence is governed by the Poisson postulates. If fracture happens when at least *N* defects are present then the failure probability is given as:

$$P_f = 1 - \frac{[\Gamma(N+1) - \Gamma(\rho V, N+1)]}{\Gamma(N+1)}$$

where ρ is the mean density of defects and V is the volume of the component.

Li and Fok [14] used a deterministic model to predict the failure process in quasi-brittle materials subjected to different strain gradients. The authors assumed a bilinear stress-strain response of the material and, using the simple beam theory, showed that the flexural strength was greater than the tensile strength: the stress-retention capability of the material following damage initiation led to an increase in the peak bending moment and thus a bend strength that was seemingly higher than the tensile strength. Through statistical analysis, the authors also demonstrated an increase in the Weibull modulus of the failure loads with increasing strain gradients, as was found through the experiments.

Le et al. [15, 16-19] have presented a nano-mechanics based probabilistic theory for the strength and life-time prediction of quasi-brittle structures. The theory employs the rate process theory for modeling fracture at the nano level. Breaking of the atomic bonds at the nano level is characterized by a jump of the interatomic potential over the thermal activation energy barriers and distribution of the thermal energies amongst atoms. The authors have justified that at the atomic level the failure of the bonds is quasi-stationary, i.e., the frequency of the bond breakage is much smaller than the frequency of atomic vibrations. Based on this justification, the authors assert that the probability of failure of the interatomic bonds is proportional to the failure frequency of bonds.

The failure probability of a nano-element is expressed as:

$$P_f \propto C_T c^2 \sigma^2$$

where $C_T = H_T \gamma_1 \int_{\alpha_o}^{\alpha_c} \alpha k_a^2(\alpha) d\alpha$ and $H_T = e^{-Q_o/kT}(\delta_a l_a^2/E_1 h)$.

δ_a: atomic spacing, h: Planck constant = 6.626 x 10^{-34} Js, k: Boltzmann constant = 1.381 x 10^{-23} J/K, Q_o: activation energy at no stress, T: absolute temperature, σ: macroscale stress on the structure, E_1: elastic modulus of the nano-element, γ_1: geometry constant, α:

relative crack length = crack length/characteristic size of the nano-element; α_o, α_c: initial and critical relative crack length, $k_a(\alpha)$: dimensionless stress intensity factor, c: nano-macro stress concentration factor.

The authors used a hierarchical model (model with combination of chain models and fiber bundle models) to relate the strength distribution of a nano-scale element to that of a representative volume element (RVE) at the macro-scale. For quasi-brittle materials the probability distribution of strength transitions from Gaussian to Weibull distribution with increase in the size of the structure. The authors incorporated this transition and evaluated the cumulative distribution function (cdf) of one RVE as:

$$P_1(\sigma_N) = 1 - e^{-\left(\frac{\sigma_N}{s_o}\right)^m} \quad (\sigma_N < \sigma_{gr})$$

$$P_1(\sigma_N) = P_{gr} + \frac{r_f}{\delta_G\sqrt{2\pi}} \int_{\sigma_{gr}}^{\sigma_N} e^{-\left(\sigma' - \mu_G\right)^2 / 2\delta_G{}^2} d\sigma' \quad (\sigma_N > \sigma_{gr}).$$

σ_N: nominal strength, m: Weibull modulus, s_o: scale parameter of the Weibull tail, μ_G: mean of the Gaussian core, δ_G: standard deviation of the Gaussian core, r_f: scaling parameter required to normalize the grafted cdf so that $P_1(\infty)=1$, P_{gr}: grafting probability = $1-\exp[-(\sigma_{gr}/s_o)^m]$, σ_{gr}: grafted strength, i.e., the strength corresponding to the conjunction point of Weibull and Gaussian distribution on the strength cdf curve.

The authors considered only structures with so-called positive geometry, i.e., the structures in which the critical stress intensity factor monotonically increases with increase in the crack length; these structures fails as soon as a macro-crack initiates from one RVE. In these structures, the weakest link model is applicable and based on this model the failure probability of a structure is expressed as:

$$P_f(\sigma_N) = 1 - \prod_{i=1}^{N}\left[1 - P_1\left(\langle s(\mathbf{x_i})\rangle \sigma_N\right)\right]$$

where $P_1(\sigma)$: strength cdf of one RVE, $s(\mathbf{x_i})$: field of dimensionless maximum principal stress in the structure and N: number of RVEs in the structure. For a sufficiently large structure tail of the strength cdf of one RVE is important; so, $P_1(\sigma)=(\sigma/s_o)^m$. Therefore failure probability of a large structure can be expressed as:

$$P_f(\sigma_N) = 1 - \exp\left[-\int_V \langle s(\mathbf{x_i})\rangle^m \frac{dV(\mathbf{x})}{V_o}\left(\frac{\sigma_N}{s_o}\right)^m\right]$$

where V_o: volume of one RVE.

The strength distribution was related to the lifetime distribution of the structure using a power law based relation between the nano-crack growth rate and the macro-scale stress intensity factor. The power relation is expressed as:

$$\dot{a} = Ae^{-Q_o/kT}K^n$$

where $\dot{a}$: nano-crack growth rate, A: constant, Q_o: activation energy at no applied stress, k: Boltzmann constant, T: absolute temperature, K: macro-scale stress intensity factor. The lifetime (λ) distribution of one RVE was obtained as:

$$\text{for } \lambda < \lambda_{gr} \ : \ P_1(\lambda) = 1 - e^{-\left(\frac{\lambda}{s_\lambda}\right)^{\bar{m}}}$$

$$\text{for } \lambda > \lambda_{gr} \ : \ P_1(\lambda) = P_{gr} + \frac{r_f}{\delta_G\sqrt{2\pi}}\int_{\gamma\lambda_{gr}^{1/(n+1)}}^{\gamma\lambda^{1/(n+1)}} e^{-\left(\lambda' - \mu_G\right)^2/2{\delta_G}^2 d\lambda'}.$$

$$\text{where } \gamma = \beta\sigma_o^{\frac{n}{n+1}}, \qquad \lambda_{gr} = \beta^{-1}\sigma_o^{-n}\sigma_{N,gr}^{n+1}, \qquad s_\lambda = s_o^{n+1}\beta^{-(n+1)}\sigma_o^{-n},$$

$$\bar{m} = \frac{m}{n+1}, \qquad \beta = [r(n+1)]^{\frac{1}{n+1}}, \qquad r: \text{loading rate}$$

σ_o: constant = $F_o/{l_o}^2$, F_o: load level chosen for lifetime testing, l_o: material length scale and λ_{gr}: grafted lifetime, i.e., the lifetime corresponding to the conjunction point of

Weibull and Gaussian distribution on the distribution curve. The lifetime distribution for the structure was evaluated from the RVE lifetime distribution and is expressed as:

$$P_f(\sigma_N) = 1 - \prod_{i=1}^{N}[1 - P_1(\langle \sigma_o s(\mathbf{x_i})\rangle, \lambda)]$$

where s(**x**) is the dimensionless stress field. The lifetime distribution of a large structure was obtained as:

$$P_f(\lambda) = 1 - \exp\left[-\int_V \langle s(\mathbf{x_i})\rangle^{n\bar{m}} \frac{dV(\mathbf{x})}{V_o}\left(\frac{\lambda}{s_\lambda}\right)^m\right]$$

where s_o: scale parameter of the Weibull tail. The Weibull modulus for the strength and lifetime distribution are related through a simple relation involving the exponent of the power-law for the crack growth as:

$$\bar{m} = \frac{m}{n+1}.$$

This simple relation leads to a major benefit of this theory: the lifetime distribution statistics ($\bar{m}$) can be determined by few tests of the mean size effect (which provide the value of m) and crack propagation tests (which provide the value of exponent n). Thus, without determining the lifetime histograms, which involves a time-consuming and expensive process, lifetime distribution can be obtained for a structure.

Several studies focused on modeling failure of a component/structure have been conducted in the past. Often the component/structure is assumed to have homogeneous properties [20-22]. This approach does not consider the heterogeneity present in the microstructure of the material which gives rise to the spatial variation in the material properties and may play a significant role in the fracture process. Figure 2.1 shows the heterogeneity found in graphite, a quasi-brittle material.

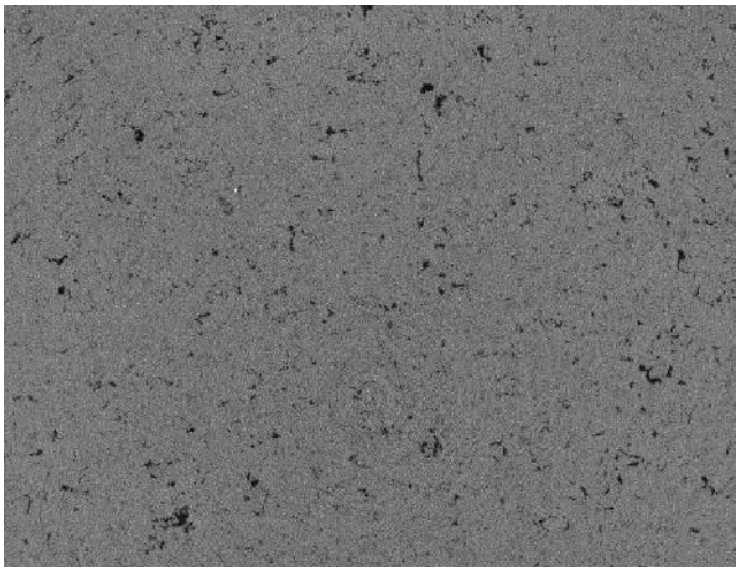

Figure 2.1: Image showing the heterogeneity in the microstructure of graphite.

2.2 MATERIAL HETEROGENEITY

Burchell et al. [23] asserted that the pores in graphite, a quasi-brittle material, can interact with the stress field and cause localized stress intensification, thus causing crack initiation even at pores that have lower stresses but are more favorably oriented. The pores can also affect the already propagating cracks, either arresting or accelerating their propagation. Therefore, material heterogeneity can affect the failure characteristics, making it imperative to include heterogeneity to accurately model failure of brittle and quasi-brittle components/structures. Berre et al. [24] investigated the effect of porosity on the Young's modulus and tensile strength of graphite. Material properties derived from nanoindentation were incorporated in the numerical modeling based on micro-computed tomography (CT) images of graphite; reduction in Young's modulus as well as the tensile strength with increasing porosity was accurately predicted. Thus, provided the

distribution of heterogeneity and their effect on the mechanical properties are known, the distribution of the latter within a component can be established.

Burchell et al. [23] [25] presented an approach to calculate the failure probability which combines fracture mechanics based failure criteria and microstructural description of a quasi-brittle material, thus accounting for heterogeneity in the material. The material's microstructure is assumed to be comprised of cubic particles, each of which has a plane of weakness/cleavage plane and pores are assumed to be randomly scattered in the material. Thus, the model has two stochastic parameters: randomly distributed pores and randomly oriented cleavage planes in the cubic particles. The model assumes log-normal distribution of the pores, and crack initiates either at the pore or very close to the pore. The probability that the size of the defect lies between a and a+da is f(a)da; f(a) is expressed as:

$$f(a) = \alpha \, x \exp\left[-\frac{1}{2}\left(\frac{\ln 2a - \ln S_o}{\ln S_d}\right)^2\right]$$

where α is a constant, a is the crack half-length, S_o is the mean pore size and S_d is a constant related to the spread in the data. The failure probability of a component containing NV pores (N is the number of pores per unit volume and V is the specimen volume) is given as:

$$P_{fa} = 1 - \left[1 - \int_0^{\infty} f(a).P_f(\sigma, a)da\right]^{2NV}$$

where σ is the stress at the crack tip, P_f is the probability that failure of n_f filler particles ahead of the crack tip (with initial size 2a) will occur due to propagation of the crack tip. In the model P_f has been approximated as:

$$\ln P_f \cong n_f \int_0^k \ln \left[\frac{4}{\pi} \cos^{-1} \left(\frac{K_{IC}}{\sigma \sqrt{\pi(a + kf)}} \right)^{\frac{1}{3}} \right] dk$$

where k denotes the k^{th} filler particle, K_{IC} is the critical stress intensity factor and f is the filler particle size.

In another work, Berre et al. [26] demonstrated the use of X-ray micro-computed tomography (CT) to model the microstructure of Gilsocarbon graphite, incorporating the heterogeneity as multi-phases in the material. Based on the gray scale values in different voxels of the 3D image, corresponding mechanical properties were assigned to the different regions in the material model. The authors assert that the multi-phase model leads to more accurate representation of the material when compared to the one where only binary phases, pores and solid material, are considered. This technique was used by the authors to perform failure analysis of graphite with different levels of porosity [27]. The stress-strain curves corresponding to different porosity levels were evaluated and the tensile strength was determined.

Yang et al. [28] compared the failure in homogeneous and heterogeneous models of a quasi-brittle material. For incorporating heterogeneity, instead of deriving properties from the microstructure, the elements of the finite element model were randomly assigned different properties generated from a Weibull distribution. The failure was simulated by explicit crack modeling under uniaxial tension. The potential crack paths were formed by inserting cohesive elements with tension and shear softening laws moderated by the spatially varying Weibull random fields. It was found that the cracks in the heterogeneous models were more realistic and closely represented the complicated fracture process, while the homogeneous models showed incorrect crack patterns and

load-displacement curves with strong dependence on mesh density. The approach has the advantage of being computationally inexpensive, thus making it applicable to a wide range of problems on structural heterogeneity.

2.3 REFERENCES

1. H. Schiffers, G. Keist, G. Haag and W. Hammer, Analysis of Stress and Deformation of Reactor Graphite, 1977.
2. W. Weibull, A Statistical Theory of The Strength of Materials, Ingeniors Vetenskaps Akademiens, Hadlingar, 151, (1939).
3. B.C. Mitchell, J. Smart, S.L. Fok and B.J. Marsden, The Mechanical Testing of Nuclear Graphite, Journal of Nuclear Materials, 322, 126-137, 2003.
4. W. Weibull, The Phenomenon of Rupture in Solids, Ingeniors Vetenskaps Akademiens, Hadlingar, 153, (1939).
5. S.B. Batdorf and J.G. Crose, A Statistical Theory for the Fracture of Brittle Structures Subjected to Non-uniform Polyaxial Stresses, Journal of Applied Mechanics, 41(2), 459-464, 1974.
6. N.N. Nemeth and R.L. Bratton, Statistical Models for Fracture Relevant to Nuclear-Grade Graphite: Review and Recommendations, NASA/TM-2011-215805.
7. National Aeronautics and Space Administration (NASA) Glenn Research Center, USA, http://www.grc.nasa.gov/WWW/StructuresMaterials/MLP/software/cares-life/index.html, last accessed January 12, 2015.
8. H. Mahiou and A. Beakou, Local Stress Concentration and the Prediction of Tensile Failure in Unidirectional Composites, Composites Science and Technology, 57(12), 1661-1672, 1998.
9. A.G. Evans and R.L. Jones, Evaluation of a Fundamental Approach for the Statistical Analysis of Fracture, Journal of the American Ceramic Society, 61(3-4), 156-160, 1978.
10. J.R. Matthews, F.A. McClintock and W.J. Shack, Statistical Determination of Surface Flaw Density in Brittle Materials, Journal of the American Ceramic Society, 59(7-8), 304-308, 1976.
11. L.Y. Chao and D.K. Shetty, Equivalence of Physically Based Statistical Fracture Theories for Reliability Analysis of Ceramics in Multiaxial Loading, Journal of the American Ceramic Society, 73(7), 1917-1921, 1990.
12. F.M. Furgiuele and A. Lamberti, On the Equivalence of Two Weakest-Link Fracture Statistics Formulations, International Journal of Fracture, 51, R15-R20, 1991.

13. A.M. Freudenthal Statistical Approach to Brittle Fracture, in Fracture 2, Edited by H. Liebowitz, Academic Press, New York, 1969.

14. Li, H. and Fok, A.S.L., "An Analytical Study on the Effects of Strain Gradient on the Fracture Statistics of the Quasi-Brittle Materials", *Journal of Nuclear Materials*, Vol. 394, 2009, 136-143.

15. J. Le, Z.P. Bažant and M.Z. Bazant, Unified Nano-Mechanics Based Probabilistic Theory of Quasi-brittle and Brittle Structures: I. Strength, Static Crack Growth, Lifetime and Scaling, Journal of the Mechanics and Physics of Solids, 59, 1291-1321, 2011.

16. J. Le, Z.P. Bažant and M.Z. Bazant, Subcritical Crack Growth Law and its Consequences for Lifetime Statistics and Size Effect of Quasibrittle Structures, Journal of Physics D: Applied Physics, 42, 214008, 2009.

17. Z.P. Bažant and J. Le, Size Effect on Strength and Lifetime Probability Distributions of Quasibrittle Structures, Sādhanā, 37(1), 17-31, 2012.

18. J. Le, J. Eliáš and Z.P. Bažant, Computation of Probability Distribution of Strength of Quasibrittle Structures Failing at Macrocrack Initiation, Journal of Engineering Mechanics, 138(7), 888-899, 2012.

19. J. Le and Z.P. Bažant, Finite Weakest-Link Model of Lifetime Distribution of Quasibrittle Structures under Fatigue Loading, Mathematics and Mechanics of Solids, 19(1), 56-70, 2014.

20. Z. Zou, S.L. Fok, B.J. Marsden and S.O. Oyadiji, Numerical Simulation of Strength Test on Graphite Moderator Bricks Using a Continuum Damage Mechanics Model, Engineering Fracture Mechanics, 73, 318-330, 2006.

21. X.P. Xu and A. Needleman, Numerical Simulations of Fast Crack Growth in Brittle Solids, J. Mech. Phys. Solids, 42(9), 1397-1434, 1994.

22. L. Shi, H. Li, Z. Zou, A.S.L. Fok, B.J. Marsden, A. Hodgkins, P.M. Mummery and J. Marrow, Analysis of Crack Propagation in Nuclear Graphite Using Three-Point Bending of Sandwitched Specimens, Journal of Nuclear Materials, 372(2-3), 141-151, 2008.

23. T. D. Burchell, A Microstructurally Based Fracture Model for Polygranular Graphites, Carbon, 34(3), 297-316, 1996.

24. C. Berre, S.L. Fok, B.J. Marsden, L. Babout, A. Hodgkins, T.J. Marrow and P.M. Mummery, Numerical Modeling of the Effects of Porosity Changes on the Mechanical Properties of Nuclear Graphite, Journal of Nuclear Materials, 352, 1-5, 2006.

25. T. Burchell, T. Yahr and R. Battiste, Modeling the Multiaxial Strength of H-451 Nuclear Grade Graphite, Carbon, 45, 2570-2583, 2007.

26. C. Berre, S.L. Fok, B.J. Marsden, P.M. Mummery, T.J. Marrow and G.B. Neighbour, Microstructural Modelling of Nuclear Graphite Using Multi-Phase Models, 380, 46-58, 2008.

27. C. Berre, S. L. Fok, P. M. Mummery, J. Ali, B. J. Marsden, T. J. Marrow and G. B. Neighbour, Failure Analysis of the Effects of Porosity in Thermally Oxidised Nuclear Graphite Using Finite Element Modelling, Journal of Nuclear Materials, 381(1-2), 1-8, 2008.

28. Z.J. Yang, X.T. Su, J.F. Chen and G.H. Liu, Monte Carlo Simulation of Complex Cohesive Fracture in Random Heterogeneous Quasi-Brittle Materials, International Journal of Solids and Structures, 46, 3222-3234, 2009.

3. THE WEIBULL MODEL FOR ESTIMATING FAILURE IN BRITTLE MATERIALS

Brittle/quasi-brittle materials, which include ceramics, glasses, metallic carbides, graphite and concrete, show large variation in the fracture properties. Due to this large variation it is difficult to predict the failure of components and structures made of these materials precisely. Engineers and scientists use probabilistic approaches to estimate failure in these components. The Weibull model is one of the most extensively used probabilistic models. In this chapter a discussion about the Weibull model and its limitations and shortcomings, which lead to inaccuracy in the predictions, are presented. The discussion is followed by a concise presentation of an alternative approach based on explicit crack modeling (ECM).

3.1 WEIBULL MODEL AND WEAKEST LINK THEORY

Weibull's probabilistic model is based on the weakest-link theory. The weakest-link theory was first formulated by Peirce in 1926 [1]. According to this theory, the strength of a chain is determined by the strength of its weakest link. Consequently, the survival of the chain requires the survival of all the links in the chain. Since, in brittle materials, failure can be assumed to be a result of unstable propagation of the most critical flaw, the weakest-link theory can be used to model the failure probability of brittle materials.

Let the survival probability of a unit volume of material under stress state σ be $p_s(\sigma)$. According to the weakest-link model, the survival probability of an element having volume ΔV is $p_s(\sigma)^{\frac{\Delta V}{v}}$, where v is unit volume. For a brittle structure made up of N elements, the probability of survival, P_s, can be expressed as:

$$P_s = p_s(\sigma_1)^{\frac{\Delta V_1}{v}} p_s(\sigma_2)^{\frac{\Delta V_2}{v}} \dots p_s(\sigma_N)^{\frac{\Delta V_N}{v}} \qquad (3.1)$$

where $p_s(\sigma_i)$ denotes the survival probability of a unit volume in stress state σ_i and ΔV_i denotes the volume of the i^{th} element. Equation (3.1) can be rewritten as:

$$P_s = \exp\left[\sum_{i=1}^{N} \ln\{p_s(\sigma_i)\}\frac{\Delta V_i}{v}\right] \qquad (3.2)$$

For a continuous stress field with $\Delta V_i \to 0$, equation (3.2) can be expressed as:

$$P_s = \exp\left[\int_V \ln\{p_s(\sigma_i)\}\frac{dV}{v}\right] \qquad (3.3)$$

Weibull ([2], [3]) proposed the following function for $p_s(\sigma)$:

$$p_s(\sigma) = \exp\left\{-\left\langle\frac{\sigma - \sigma_{th}}{\sigma_o}\right\rangle^m\right\} \qquad (3.4)$$

where σ_{th}, σ_o and m are three empirical parameters [4], and $\langle\rangle$ are the Macaulay operators, indicating that only tensile stresses contribute towards the failure of brittle structures. σ_{th} is the threshold stress below which no failure can occur, m is the Weibull modulus that controls the variation of the failure stress, and σ_o is related to the strength per unit volume of material. The Weibull model has been extensively used for brittle materials [5]. For ease of calculation, σ_{th} is often neglected, which also makes the predictions conservative. Thus, equation (3.4) becomes:

$$p_s(\sigma) = \exp\left\{-\left\langle\frac{\sigma}{\sigma_o}\right\rangle^m\right\} \qquad (3.5)$$

Substituting (3.5) into (3.3) leads to:

$$P_s = \exp[-\int_V \left\langle \frac{\sigma}{\sigma_o} \right\rangle^m \frac{dV}{v}] \qquad (3.6)$$

Equation (3.6) is valid for the case of uniaxial stress only. For more complex loadings, i.e., when multi-axial stresses are present, one needs to consider the combined effect of these stresses on the survival of the structure. A method suggested for handling multi-axial stresses in fracture statistics is the Barnett-Freudenthal approximation [6, 7]. This approximation is also known as the Principle of Independent Actions (PIA) [8]. It states that the principal stresses that cause failure of the material act independently of each other. Therefore, the total survival probability of an element is the product of its survival probabilities when acted upon by the principal stresses individually. It follows that, for a material element with the principal stresses σ_1, σ_2, and σ_3, the survival probability is:

$$p_s = p_s(\sigma_1)\, p_s(\sigma_2)\, p_s(\sigma_3) \qquad (3.7)$$

Using equations (3.6) and (3.7), the survival probability of a structure under multi-axial stresses is expressed as:

$$P_s = \exp[-\int_V \{\left\langle \frac{\sigma_1}{\sigma_o} \right\rangle^m + \left\langle \frac{\sigma_2}{\sigma_o} \right\rangle^m + \left\langle \frac{\sigma_3}{\sigma_o} \right\rangle^m \frac{dV}{v}\}] \qquad (3.8)$$

To avoid numerical problems involved in raising the stresses to a very high power and in dealing with very large volumes, equation (3.8) can be rewritten as:

$$P_s = \exp(-\left\langle \frac{\sigma_{nom}}{\sigma_o} \right\rangle^m \frac{V}{v} \Sigma) \qquad (3.9)$$

where σ_{nom} is a nominal stress (usually the highest stress in the structure) and V is the total volume of the structure. Σ is the stress-volume integral and is defined as:

$$\Sigma = \int (\sum_{i=1}^{i=3} \left\langle \frac{\sigma_i}{\sigma_{nom}} \right\rangle^m) \frac{dV}{V} \qquad (3.10)$$

It can be noted here that Σ only depends on the shape of the structure and the normalized stress distribution within it; it does not depend on the actual load level or volume of the structure.

3.2 LIMITATIONS OF WEIBULL PROBABILISTIC MODEL

Dependence of Weibull Parameters on Strain Gradient

The Weibull model, although extensively used for predicting the failure probability of brittle components, has limitations. The empirical parameters σ_o and m are assumed to be material constants but it has been reported based on experiments that these parameters depend on the strain gradients. Mitchell et al. [9] performed tensile tests on L-shaped specimens with different radii of curvature (r = 4mm, 2mm, 1mm and ≈0mm) as shown in Figure 3.1.

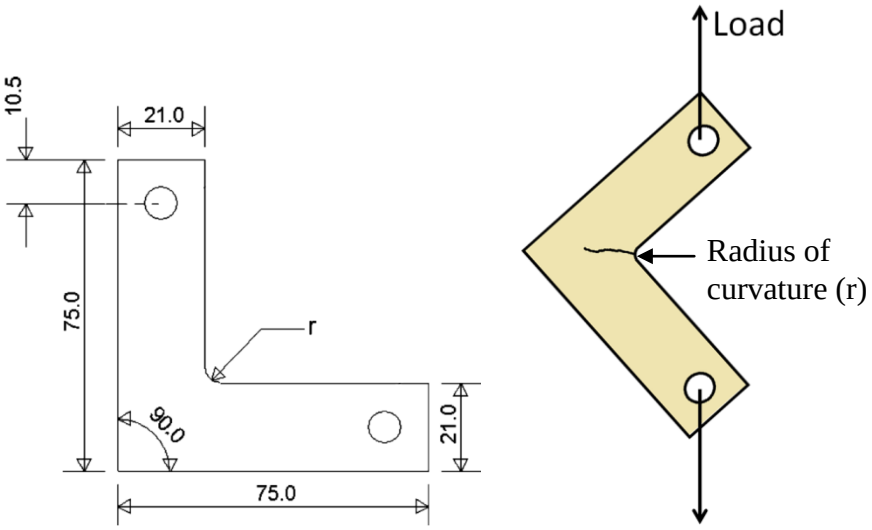

Figure 3.1: Dimensions of the L-shaped specimen (mm) (source: [9] and a specimen under loading.

For each radius of curvature, 42 specimens were tested. The peak load, corresponding probability of failure and Weibull modulus were determined for each set of tests. Figure 3.2 shows the failure probability vs. load data and the corresponding Weibull modulus. As the radius of curvature decreased (strain gradient became greater) the Weibull modulus increased from 25.8 to 54.4.

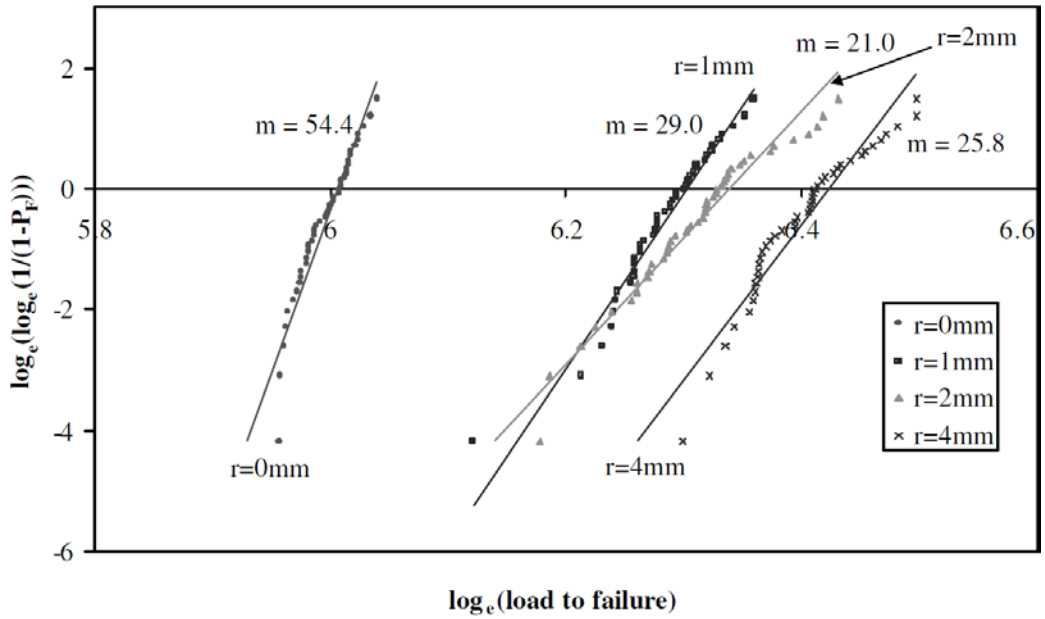

Figure 3.2: Comparison of Weibull moduli obtained for L-shaped specimen with different radii of curvature (Source: [9]).

Li and Fok [10] used a deterministic model to show that as the strain gradient increases the Weibull moduli for the strength also increases. The authors assumed a bilinear stress-strain response of the material to model damage initiation and evolution. Different values of critical strain (strain at which damage initiates) were generated based on the Weibull distribution to incorporate the randomness in the fracture property of the material. Various levels of strain gradients were assumed to model the changing radius of curvature in the L-shaped specimens. The model was solved analytically for the failure load using the beam theory. It was found that the specimen with higher strain gradient

showed a higher Weibull modulus for the failure load. Using a similar method, the failure loads in a tensile test and a pure bending test were evaluated. The Weibull modulus for the failure loads in the bending test was found to be greater (9.4) than that obtained for the tensile test (6.9) for which there was no strain gradient in the specimens.

Inconsistencies between Weibull Model based Predictions about Size Effect and Experimental Results

The Weibull model is often used to explain the effect of size on the fracture properties of brittle materials. According to the Weibull model, as the size of a specimen increases the probability of a strength-limiting flaw being present in the specimen increases, and therefore the strength of the specimen decreases. The relation describing the variation of strength with change in effective volume (size) is given as:

$$\frac{\sigma_2}{\sigma_1} = \left(\frac{V_1}{V_2}\right)^{\frac{1}{m}}$$

where 1 and 2 denote specimens with different sizes. Experimental evidences contradictory to this trend have been found, thus, raising questions about the Weibull model's capability to predict the size effect.

Brocklehurst [11] conducted tensile and four-point bend tests on IM1-24 graphite to measure the effect of specimen volume on the tensile and bend strength, respectively. It was found that for specimens which had a volume greater than 1 cm^3, the bend strength decreased with an increase in the volume of the specimen. But specimens with volume less than 1 cm^3 showed the opposite trend: the bend strength increased with an increase in the size of the specimen. The tensile strength also showed a continuous increase with an increase in the specimen diameter, which ranged from 2.5 mm to 30 mm. However, for

specimens with diameters greater than 10 mm the increase in strength with specimen size was not significant.

Strizak [12] conducted tensile tests on two different graphites: H-451 and IG-110. Specimens with diameters of 6.35, 9.53, 15.88 and 25.40 mm were used for the tests. It was found that for both materials the tensile strength increased with an increase in the specimen size.

Overestimation of Failure Probability

The Weibull model overestimates the failure probability for components with stress concentrations. It happens because the Weibull stress function $(\sigma/\sigma_o)^m$ has the stress raised to the m^{th} power which increases greatly as the stress increases.

Limited Applications of the Model

The Weibull model is applicable only to structures which fracture catastrophically as soon as a crack occurs. However, in some cases the structure may not fail immediately after the development of a crack. An example of this type of structure is the dam. After the occurrence of the first crack in the dam, significant time may elapse before the structure fails completely. The Weibull model cannot estimate the failure probability of structures of this type.

3.3 EXPLICIT CRACK MODELING APPROACH

Due to the limitations and shortcomings of the Weibull model, its predictions for the failure probability of components/structures are often not accurate. Uncertainties in the predictions require designers to take higher safety margins which increase the cost of

manufacturing of the components. Therefore, an alternative approach capable of accurately predicting failure probability is desirable.

An approach for predicting the failure probability in brittle and quasi-brittle components based on explicit modeling of cracking is presented herein. It entails the following steps:

1) Construct constitutive model(s) for modeling stresses in the component/structure under the operating conditions.

2) Generate finite element (FE) models of the component/structure which incorporate heterogeneity found in the material properties. The heterogeneity can be incorporated by assigning randomly either (a) different but uniform material properties to each model or (b) different properties to the elements within each model.

3) Simulate fracture in the FE models using a suitable numerical technique and evaluate failure probability based on the results.

The probability of failure is evaluated from the results of the fracture simulations as:

$$\text{Failure probability (time t)} = \frac{\text{Number of specimens failed uptil time t}}{\text{Total number of specimens}} \qquad (3.11)$$

This approach for predicting the failure probability is illustrated through simulating the failure of graphite bricks of a nuclear reactor in chapter 4.

3.4 REFERENCES

1) F. T. Peirce, “The Weakest Link” Theorems of the Strength of Long and of Composite Specimens, J. Textile Inst., 17, 355-368, 1926.
2) W. Weibull, A Statistical Theory of The Strength of Materials, Ingeniors Vetenskaps Akademiens, Hadlingar, No. 151, 1939.
3) W. Weibull, A Statistical Distribution Function of Wide Applicability”, Journal of Applied Mechanics, 18, 293-297, 1951.
4) Z. P. Bazant and J. Planas, Fracture and Size Effect in Concrete and Other Quasibrittle Materials, CRC Press, 1998.
5) C. Lu, R. Danzer and F.D. Fischer, Failure Statistics of Brittle Materials: Weibull or Normal Distribution, Physical Review E., 65, 067102, 2002.
6) A. M. Freudenthal, Statistical Approach to Brittle Fracture, Fracture, Academic Press, 2, 591-619, 1969.
7) R. L. Barnett, C. L. Connors, P. C. Hermann and J. R. Wingfield, Fracture of Brittle Materials Under Transient Mechanical and Thermal loading, U.S. Air Force Flight Dynamics Laboratory, AFFDL-TR-66-220, 1967.
8) P. Stanley, H. Fessler and A.D. Sivill, An Engineer’s Approach to the Prediction of Failure Probability of Brittle Components, The University of Nottingham.
9) Mitchell, B.C., Smart J., Fok S.L., and Marsden, B.J., The Mechanical Testing of Nuclear Graphite, Journal of Nuclear Materials, 322, pp 126-137, 2003.
10) S. L. Fok and J. Smart, The Accuracy of Failure Predictions Based on Weibull Statistics, Journal of European Ceramic Society, 15, 905 – 908, 1995.
11) J.E. Brocklehurst, Fracture in Polycrystalline Graphite, Chemistry and Physics of Carbon, New York, NY, 13, 146–272, 1977.
12) J.P. Strizak, The Effect of Volume on the Tensile Strength of Several Nuclear-Grade Graphites, The Status of Graphite Development for Gas Cooled Reactors, IAEA–TECDOC–690, 233–241, 1991.

4. ASSESSMENT OF EXPLICIT CRACK MODELING APPROACH

This chapter presents an assessment and validation of the explicit crack modeling (ECM) approach. The work involved estimation of the failure probabilities of the L-shaped specimens subjected to tensile loading. The failure probability predictions obtained through the ECM approach were compared with 1) the failure probabilities obtained from the Weibull model and 2) the failure probabilities determined from the published experimental data. In addition to validating the ECM approach, the results established greater accuracy and capability of the approach over the Weibull probabilistic model.

4.1 EXPLICIT CRACK MODELING BASED APPROACH AND COMPARISON WITH THE WEIBULL MODEL

A study was conducted with the objective to illustrate the application of the ECM approach for predicting the probability of failure of a brittle/quasi-brittle structure and compare the ECM approach based predictions with published experimental data. The predictions from the ECM approach were also compared with the Weibull model based predictions to compare the accuracy of the two approaches.

As discussed earlier in chapter 3, the Weibull model approach involves evaluating the stress distribution in a specimen subjected to loading. The stress distribution is then used to calculate the failure probability of the specimen as described through equations:

$$P_s = \exp\left(-\left\langle\frac{\sigma_{nom}}{\sigma_o}\right\rangle^m \frac{V}{v}\Sigma\right) \qquad (3.9)$$

$$\Sigma = \int \left(\sum_{i=1}^{i=3} \left\langle \frac{\sigma_i}{\sigma_{nom}} \right\rangle^m\right) \frac{dV}{V} \qquad (3.10)$$

where σ_{nom} is a nominal stress (usually the highest stress in the structure), V is the total volume of the structure and Σ is the stress-volume integral. For a simple geometry, the stresses can be evaluated analytically; but for a complex geometry, it is difficult to get an analytical solution and the stresses are evaluated numerically. The numerically evaluated stress-volume integral can be written as:

$$\Sigma = \frac{1}{V_{Total}} \sum_{k=1}^{ne} \sum_{i=1}^{np} \left(\left(\left(\frac{\langle \sigma_I \rangle}{\sigma_{nom}} \right)^m + \left(\frac{\langle \sigma_{II} \rangle}{\sigma_{nom}} \right)^m + \left(\frac{\langle \sigma_{III} \rangle}{\sigma_{nom}} \right)^m \right) V_{ik} \right) \qquad (4.1)$$

where ne is the number of elements in the finite element model, np is the number of integration points per element, V_{ik} is the volume associated with the i^{th} integration point of the k^{th} element and V_{Total} is the total volume of the structure. Equation 4.1 is applicable to any general problem. Stresses were evaluated numerically for the L-shaped specimens using the commercial finite element software Abaqus. A Fortran program was written which took the results file from Abaqus as input to evaluate the stress-volume integral, the nominal stress and the failure probability. The stress volume integral obtained numerically using Equation 4.1 was substituted in Equation 3.9 to calculate the probability of failure.

L-shaped specimens made of PPEA graphite were selected as the quasi-brittle structures for analysis. These specimens were considered to be subjected to tensile loading as shown in Figure 4.1. The models of the specimens were meshed with CPE4 (continuum, plane–strain, bilinear, 4-node) elements. The FE model of the specimen with

radius of curvature 4 mm had 5300 elements while the one having radius of curvature 1 mm had 7800 elements.

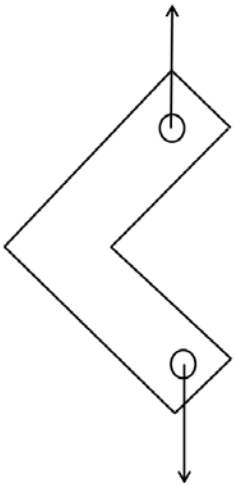

Figure 4.1: L-shaped specimen under tensile loading.

In the first phase, the Weibull parameters of graphite m and σ_o were determined by calibration. The calibration was performed by setting the parameters such that the predicted failure probability of L-shaped specimens with a certain radius of curvature for different levels of load matched with the failure probability determined from experiments conducted by Mitchell et al. [1]. The calibration was performed using the specimens with radius of curvature 4 mm. The values of the parameters determined through calibration are shown in Table 4.1. Thereafter, the calibrated Weibull parameters were employed to predict the failure probability for specimens with radius of curvature 1 mm subjected to different levels of load.

Table 4.1: Weibull model parameters for PPEA graphite determined through calibration.

Weibull modulus m (shape parameter)	σ_o (scale parameter)
26	13.95 MPa

The evaluation of the failure probability through the ECM approach involved simulation of crack initiation and propagation. Thirty FE models of the L-shaped specimens were generated. Heterogeneity was implemented in the FE models by assigning random fracture properties to the elements along the expected crack path. The random fracture properties were generated based on the Weibull distribution. The elements along the expected path of the crack propagation were assigned these properties as shown in Figure 4.2.

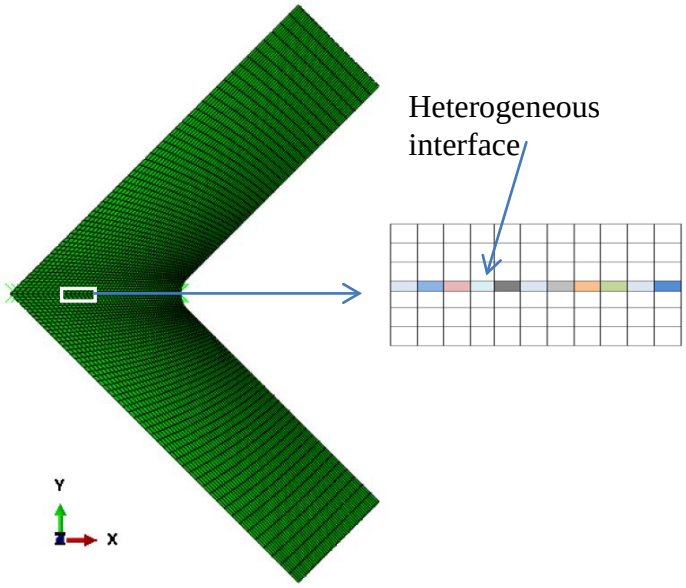

Figure 4.2: Meshed model of the L-shaped specimen (r=4mm) with heterogeneous elements embedded in it.

The Continuum Damage Mechanics (CDM) model [2] was used to simulate fracture in these FE models. The CDM model relates the tractions with the displacements at the crack surfaces and includes a stress based criterion which determines the damage initiation and a fracture mechanics based criterion which dictates the crack formation. Figure 4.3 shows the traction-separation curve for crack surfaces and the associated fracture properties. The word “intrinsic” is used to indicate grain-level property, thus,

differentiating it from the bulk property. The model has been implemented in Abaqus through its User Element subroutine (UEL) by Zou et al. [2].

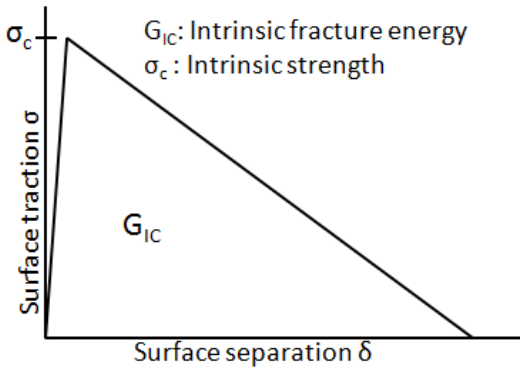

Figure 4.3: Traction separation curve and the associated fracture parameters.

The intrinsic strength was set as 17.9 MPa based on reference [4]. In the first phase, the fracture energy and the Weibull moduli for the intrinsic properties of graphite (G_{IC}, m_σ and m_G) were determined by calibration. The calibration of the Weibull modulus for the intrinsic strength (m_σ) was performed through the simulation of four-point bend test on rectangular specimens: m_σ was selected such that the Weibull modulus for the bulk flexural strength obtained from the simulations matched with the Weibull modulus obtained from the experiments conducted by Mitchell et al. [1]. The calibration of G_{IC} and m_G was performed by simulating the failure of L-shaped specimens with radius of curvature 4 mm: the failure load (peak load) and the corresponding Weibull modulus obtained from the simulations were matched with those obtained from experiments [1]. The values of the parameters determined through the calibration are shown in Table 4.2. Thereafter, the calibrated parameters were employed to predict the failure probability of specimens with radius of curvature 1 mm subjected to different levels of load.

Table 4.2: Parameters of the material determined through calibration for explicit crack modeling approach.

Intrinsic fracture energy (G_{IC})	Intrinsic Weibull modulus, m_σ	Intrinsic Weibull modulus, m_G
130 J/m^2	10	24

The predictions of the failure probability of L-shape specimens with radius of curvature 1 mm for different levels of load were made through the Weibull model and the ECM approach. The predictions were then compared with the failure probability determined from the experimental data [1].

Results

Figure 4.4 shows the simulated fracture in a L-shaped specimen model and Figure 4.5 shows the predictions of failure probability (P_f) for different load levels obtained from 1) the Weibull model, 2) experiments [1] and 3) the ECM approach. The experimental data fit well with the Weibull distribution and the corresponding Weibull modulus was found to be 29. The data obtained through the ECM approach lie close to the experimental data and the corresponding Weibull modulus was found to be 29. The Weibull modulus for the predictions obtained from the Weibull model was found to be 26 as expected. It can be seen from Figure 4.5 that the Weibull data lie quite apart from the experimental data, over-predicting the probability of failure for a each level of load. This overestimation of the failure probability by the Weibull model is due to the stress concentration in the specimen. It may be noted that the L-shaped specimen, for which these predictions were made, had radius of curvature (r) 1 mm. Thus, the specimen had a higher stress concentration than the specimen which was used for calibration of the Weibull parameters (r=4 mm).

On the other hand, the explicit crack modeling approach based predictions successfully incorporated the effect of the sharp corner in the specimen and the predictions matched well with the experimental results. As discussed earlier in chapter 3, due to an increase in the strain gradient the Weibull modulus also increased. The ECM approach captured this increment in the Weibull modulus: the predicted data had a Weibull modulus of 29. This capability of the ECM approach to predict the effect of the strain gradient on the variation in the failure load (characterized by the Weibull modulus) can be attributed to the fundamental physical basis of this approach: factors which govern fracture in a structure (fracture energy, strength of the material, damage behavior of the material, heterogeneity in the material microstructure) are incorporated within the ECM approach. On the other hand, the Weibull model cannot inherently account for changes in the variation of the failure load with changes in the strain gradient.

The inaccuracy in the Weibull model predictions for the L-shaped specimens can be also attributed to the violation of the basic assumption of the model. The model is based on the weakest-link theory which states that a brittle structure fails due to failure of the weakest element in the structure. This assumption was violated because the stress concentration in the L-shaped specimen (arising from the sharp corner) forced the crack to initiate at the corner and propagation of the crack was not catastrophic.

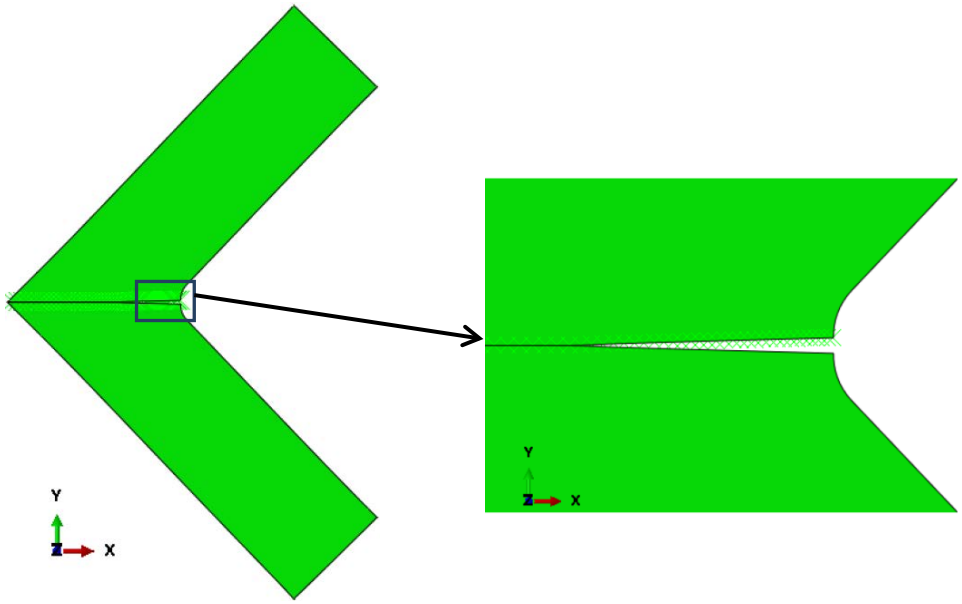

Figure 4.4: Cracked model of a L-shaped specimen (Scale factor: 10).

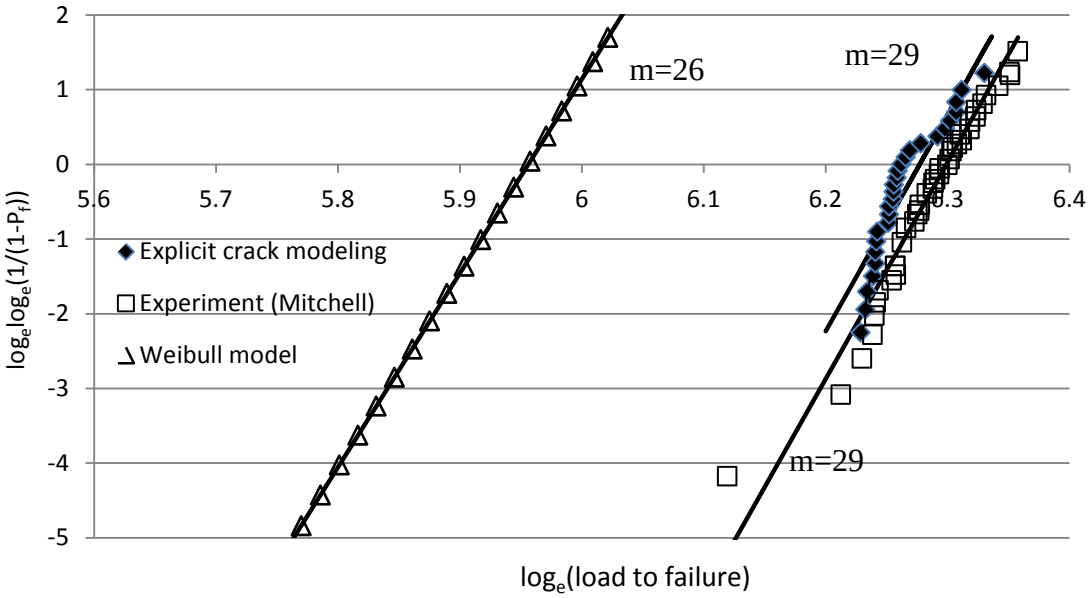

Figure 4.5: Comparison of the predictions of failure probability from the Weibull model, explicit crack modeling approach and experimental data.

Conclusions

The following conclusions can be drawn from the above discussion:

1. The explicit crack modeling approach gives the correct failure probability even when stress concentration exists while the Weibull model based approach overestimates the failure probability.

2. The explicit crack modeling approach has the capability to correctly predict the variation in the failure load (Weibull modulus) with changes in the strain gradient by incorporating randomness in the fracture properties of brittle materials within a specimen.

3. The explicit crack modeling approach provides detailed information about the failure in brittle/quasi-brittle materials: the crack initiation and propagation can be predicted. The Weibull model does not provide such information.

4.2 REFERENCES

1. B.C. Mitchell, J. Smart, S.L. Fok and B.J. Marsden, The Mechanical Testing of Nuclear Graphite, Journal of Nuclear Materials, 322, 126-137, 2003.
2. Z. Zou, S.L. Fok, S.O. Oyadiji, and B.J. Marsden, Failure Predictions for Nuclear Graphite Using a Continuum Damage Mechanics Model, Journal of Nuclear Materials, 324, 116-124, 2004.
3. Abaqus Documentation, Simulia Dassault Systemes, RI, USA.
4. T.L. Albers, High Temperature Properties of Nuclear Graphite, Journal of Engineering for Gas Turbines and Power, 131/064501-1, 2009.

5. EXPLICIT CRACK MODELING APPROACH FOR PREDICTING SIZE EFFECT

The fracture properties of a material are determined through standard tests such as the tensile test, 3-point bend test and 4-point bend test. It has been observed that the value of the property determined through these tests is dependent on the size of the specimen used in these tests. Although Weibull model is often used to predict the effect of specimen size on fracture properties, it has shortcomings as discussed in chapter 3: a) the Weibull modulus, which is supposed to be a material property, has been found to depend on the type of loading, b) the model overestimates the failure probability for structures having stress concentration and c) in some cases the strength has been found to increase with the size of the specimen which is contradictory to the Weibull model predictions about size effect. In chapter 3 and 4 explicit crack modeling approach was presented and established as a more accurate way to estimate failure in brittle/quasi-brittle materials. This chapter presents a study which demonstrates the ability of the explicit crack modeling technique to predict the effect of specimen size on the apparent fracture properties through the examples of standard mechanical tests.

5.1 EARLIER STUDIES ON SIZE EFFECT

Brocklehurst conducted tensile and four-point bend tests on IM1-24 graphite to measure the effect of specimen volume on the tensile and bend strength, respectively [1]. It was found that for specimens which had a volume greater than 1 cm^3, the bend strength

decreased with an increase in the volume of the specimen. For specimens with volume less than 1 cm^3, the opposite trend was observed. The tensile strength showed a continuous increase with an increase in the specimen diameter, which ranged from 2.5 mm to 30 mm. However, for specimen with diameters greater than 10 mm the increase in strength with specimen size was not significant.

Similar tensile and four-point bend tests were conducted by Price (1976) on over 2000 specimens of H-451 graphite [2]. For the tensile tests, specimens of two different sizes, 724 mm^3 (6.4 mm diameter) and 9847 mm^3 (12.8 mm diameter) were used. These specimen sizes were not found to have any significant impact on the tensile strength: the smaller specimens were only 3% stronger than the larger specimens. The flexural strength was found to be 1.4-1.6 times greater than the tensile strength, though. It was also noted that the flexural specimens showed a higher Weibull modulus (13.6 and 15.8) than the tensile specimens (8.1 and 10.7). Strizak (1991) conducted tensile tests on two different graphites: H-451 and IG-110 [3]. Specimens with diameters of 6.35 mm, 9.53, 15.88 and 25.40 mm were used for the tests. It was found that for both materials the tensile strength increased with the specimen size. In a recent study, Li et al. [4] conducted three-point bend tests on notched NBG-18 graphite specimens of three different sizes. The mean fracture toughness (critical stress intensity factor) and the associated Weibull modulus were evaluated for each group of specimens. The fracture toughness was found to be highest for the group with the largest specimens, and decreased monotonically with a decrease in the size of the specimens. It has been found that the mechanical properties of graphite depend on its grain size. The grain sizes for H-451, IG-110, NBG-18 and IM1-24 graphite are 0.5 mm, 0.02 mm, 1.5 mm and 0.5 mm respectively.

Similar to graphite, ceramics also show size effects in their fracture properties. Quinn (1990) [5] reported three-point and four-point bend tests conducted on over 1200 ceramic specimens at seven different laboratories. The flexural specimens were machined into several sizes and were made of two different ceramic materials: 1500 sintered alumina and reaction-bonded silicon nitride (RBSN). Both materials showed a reduction in their flexural strength with an increase in the effective volume of the specimens, with alumina showing a greater reduction compared to RBSN. Similar results on the flexural strength of ceramics have been found by others [6] [7].

Li and Fok [8] used a deterministic model to predict the failure process in quasi-brittle materials subjected to different strain-gradients. The authors assumed a bilinear stress-strain response of the material and, using the simple beam theory, showed that the flexural strength was greater than the tensile strength: the stress-retention capability of the material following damage initiation led to an increase in the peak bending moment and thus a bend strength that was seemingly higher than the tensile strength. Through statistical analysis, they also demonstrated an increase in the Weibull modulus of the failure loads with increasing strain-gradients, as was found in experiments. However, they did not consider the size effect.

In this chapter the ability of explicit crack modeling approach for predicting the size effect in brittle materials is illustrated through several examples of standard tests. Continuum damage mechanics (CDM) model [9] [10] [11] was to simulate the fracture process. Variations in the fracture properties were considered by performing a Monte Carlo analysis which incorporated material heterogeneity within each specimen. The obtained results were compared with those from the experimental studies. The viability of

XFEM technique for predicting fracture in heterogeneous specimen models is yet to be established. So, instead of XFEM cohesive element method, which is also an explicit crack modeling method, was used for simulating fracture.

5.2 METHOD

The work presented herein involved simulation of standard mechanical tests, i.e. uniaxial tensile test and three-point bend test, to predict the tensile and flexural strengths, as well as the fracture toughness and their statistical distributions. The failure tests were modeled using the commercial finite element (FE) software Abaqus coupled with a continuum damage mechanics model. The continuum damage mechanics model relates the tractions with the displacements at the crack surfaces. The model includes a stress based criterion which determines damage initiation and a fracture mechanics based criterion which dictates crack formation. The model was implemented in Abaqus through its User Element subroutine (UEL) [12].

The specimens were assumed to be made of IM1-24 graphite [13, 14]. To account for the variation in the bulk fracture properties of graphite, the intrinsic heterogeneity in the material was incorporated into the finite element (FE) models of the graphite specimens by assigning randomly generated fracture properties to the user elements individually. The element size along the fracture path was fixed to be approximately equal to the grain size of IM1-24 graphite, i.e. 0.5 mm. The fracture properties (strength and the critical energy release rate) were generated using a Weibull distribution [15] [16] in MATLAB. The Weibull distribution is a special case of the generalized extreme value distribution. The probability density function for this distribution is expressed as:

$$f(x) = \alpha\beta^{-\alpha}x^{\alpha-1}\exp[(-x/\beta)^{\alpha}]$$

where

α = shape parameter of the distribution, and

β = scale parameter of the distribution.

Figure 5.1 shows the traction-separation curve for crack surfaces and the associated fracture properties. The maximum traction represents the intrinsic strength and the area of the traction-separation curve the intrinsic fracture energy. The systematic approach used to determine the effect of size on the fracture properties is shown in Table 5.1. In the first phase, the Weibull scale and shape parameters for the intrinsic properties of IM1-24 graphite (σ_c, m_σ, G_{IC} and m_G) were determined by calibration; see the C cells in Table 5.1. The calibration of the parameters was performed by simulating tensile tests and three-point bend tests (notched beams) on medium-sized specimens and matching the Weibull parameters for bulk fracture properties obtained from simulations with those obtained from experiments. Thereafter, the calibrated intrinsic parameters were employed to predict the distributions of bulk strength and bulk fracture toughness for other sizes of specimens. The P cells in Table 5.1 correspond to the tests for which predictions were made. Table 5.2 shows the intrinsic properties of IM1-24 graphite determined by calibration.

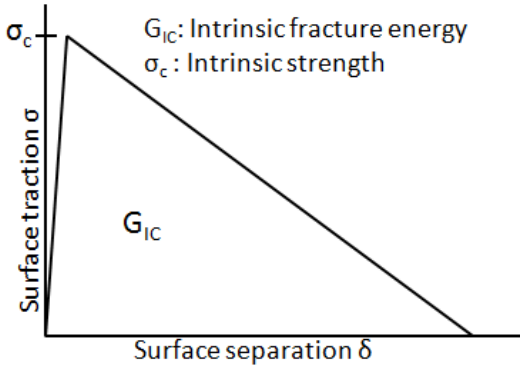

Figure 5.1: Traction separation curve and the associated fracture parameters.

Table 5.1: Summary of tests used to calibrate the intrinsic fracture properties and those for which predictions were made for bulk behavior.

Tensile test	Small	P
	Medium	C_σ
	Large	P
3-Point bending test (notched)	Small	P
	Medium	C_G
	Large	P
3-Point bending test (un-notched)	Small	P
	Medium-I	P
	Medium-II	P
	Large	P

C_σ: Calibration for intrinsic σ_c and m_σ
C_G: Calibration for intrinsic G_{IC} and m_G.
P: Prediction

Table 5.2: Fracture properties and associated statistical parameters of the material.

Intrinsic strength, σ_c (MPa)	Intrinsic fracture energy, G_{IC} (J/m^2)	Weibull modulus, m_σ	Weibull modulus, m_G
25	154	3	15

For modeling the size effect on the tensile strength of graphite, specimens with three different sizes were considered; see Table 5.3. The largest, medium and smallest specimen models were meshed with 40,000, 1600 and 100 CPE4 (continuum, plane–strain, bilinear, 4-node) elements, respectively. Figure 5.2 shows the finite element model of the largest specimen. As mentioned earlier, the strength and critical strain energy release rate varied among the elements along the assumed crack path, these being generated based on a Weibull distribution to account for the effect of material

heterogeneity of graphite on its fracture behavior. Medium-sized specimen models (Group II) were used to perform the calibration of Weibull parameters for the intrinsic fracture properties of IM1-24 graphite.

For modeling the size effect on the flexural strength of graphite, un-notched beam specimens subjected to three-point bending were simulated. Four different sizes were considered, with widths of 50, 25, 10 and 2.5 mm. The dimensions of these models are provided in detail in Table 5.4. Group I contained the largest specimens; Group II contained the next smaller specimens; and so forth. The specimen models had the same shape: the length to width and width to thickness ratios were constant for all the groups. Figure 5.3 shows the model of a Group-I specimen. The cohesive elements were inserted along the mid line of the model, again with fracture properties of the elements randomly generated based on a Weibull distribution.

For modeling the size effect on the fracture toughness of graphite, notched beam specimens under three-point bending were simulated. Three different sizes were considered, with widths of 50, 20 and 10 mm. The dimensions of the notched specimens are provided in detail in Table 5.5. Similar to the un-notched specimens, the cohesive elements were inserted along the mid line of the notched specimen models, with random fracture properties of the cohesive elements generated based on a Weibull distribution.

All the beam specimen models were meshed with CPE4 (continuum, plane–strain, bilinear, 4-node) elements. The number of elements and nodes used for meshing the models in each group are shown in tables 7.6 and 7.7. For each test and specimen size detailed in tables 7.3 to 7.5, 30 models with different material distributions were created for the Monte Carlo analysis.

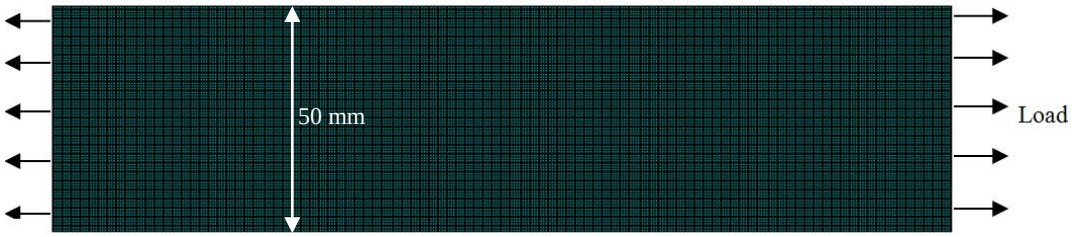

Figure 5.2: Finite element model of the largest specimen under tension.

Table 5.3: Dimensions of the un-notched graphite specimens subjected to tension.

Group	Width w (mm)	Thickness b (mm)
I	50	25
II	10	5
III	2.5	1

Table 5.4: Dimensions of the un-notched graphite specimens subjected to three-point bending.

Group	Total length L (mm)	Width w (mm)	Thickness b (mm)	Load Span S (mm)
I	220	50	25	200
II	110	25	12.5	100
III	45	10	5	40
IV	12	2.5	1.25	10

Table 5.5: Dimensions of the notched graphite specimens subjected to three-point bending.

Group	Total length L (mm)	Width w (mm)	Thickness b (mm)	Notch depth a (mm)	Load Span S (mm)
I	220	50	25	21	200
II	110	20	10	8	100
III	45	10	5	4	40

Table 5.6: Details of mesh of the specimen models for tensile test.

	Group I	Group II	Group III
Number of elements	40000	1600	100

Number of nodes	40501	1701	126

Table 5.7: Details of mesh of the specimen models for three-point bend test

	Un-notched Specimens				Notched Specimens		
	Group I	Group II	Group III	Group IV	Group I	Group II	Group III
Number of elements	8410	3838	1359	407	8410	3444	1359
Number of nodes	8547	3958	1443	463	8547	3321	1443

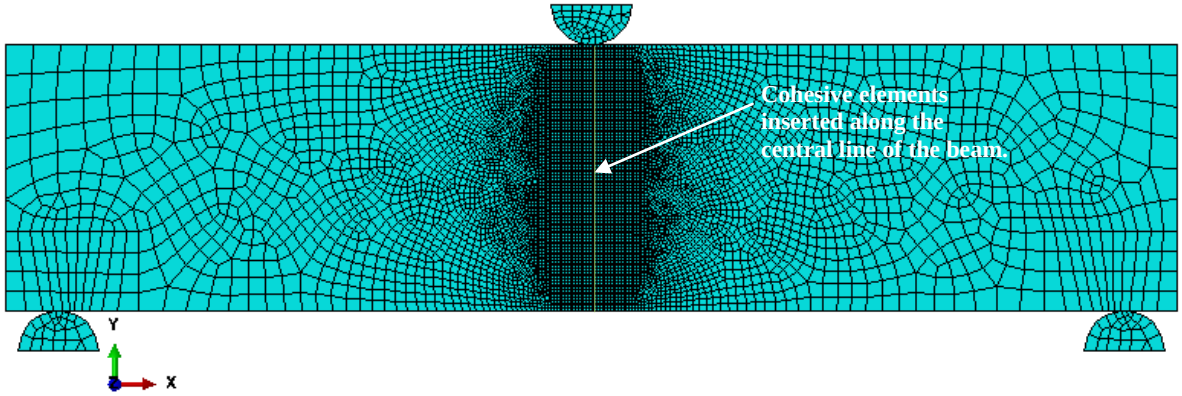

Figure 5.3: The meshed model of a Group-I un-notched specimen under three-point bending.

The flexural strengths of the un-notched specimens were determined using Euler beam theory and the peak loads. The fracture toughness, K_{IC} (MPa√m), was calculated according to Equations 1 and 2 [17]:

$$K_{IC} = g \times \left[P_{max} \times S \times \frac{10^{-6}}{b w^{\frac{3}{2}}} \right] \times \frac{3 \times \left(\frac{a}{w}\right)^{\frac{1}{2}}}{2 \times \left(1-\frac{a}{w}\right)^{\frac{3}{2}}} \qquad (1)$$

$$g = 1.9381 - 5.0947\left(\frac{a}{w}\right) + 12.386\left(\frac{a}{w}\right)^{2} - 19.2142\left(\frac{a}{w}\right)^{3} + 15.7747\left(\frac{a}{w}\right)^{4} - 5.1270\left(\frac{a}{w}\right)^{5} \qquad (2)$$

where:

P_{max} = the peak load during the test,

S = the load span of the beam,

a = the initial crack length in the beam,

b = the thickness of the beam and

w = the width of the beam.

There were a few assumptions made in modeling the tests. In the experiments, the crack rarely occurred along a straight line. However, in the present simulations the crack was set to propagate along a straight line. This simplified the failure modeling while allowing the finite element model to capture the effect of heterogeneity in the material. For the three-point bend tests on un-notched beams, convergence could not be obtained due to the very rapid propagation of the crack right after its initiation. The maximum load reached prior to the onset of instability was taken as the failure load.

5.3 RESULTS

The FE models were analyzed using Abaqus Standard [12]. Figure 5.4 shows the fracture in an un-notched Group-III specimen under 3-point bending. Figure 5.5 shows the load-displacement curves for the notched beams subjected to three-point bending obtained numerically. Figure 5.5 also shows the corresponding load-displacement curves obtained experimentally by Li et al. [4]. Table 5.8 shows the predicted mean values and standard deviations of the peak loads and strengths for the different groups of specimens subjected to tension. The table also shows the values of the Weibull modulus for the strength distribution. The corresponding results for the three-point bend test of un-notched specimens are shown in Table 5.9.

Figure 5.6 shows the variation of the predicted mean tensile strength with the size of the specimen and its comparison with the experimental results from Brocklehurst (1977) [1]. It was predicted that the mean tensile strength did not change appreciably with an increase in the specimen size. Experimentally, however, the tensile strength reduced with a decrease in specimen size. The variation of the predicted Weibull modulus for the tensile strength distribution with the specimen size is shown in Figure 5.7. The corresponding experimental Weibull modulus was evaluated from the standard deviation data presented by Brocklehurst [1] using the method given by Gong et al. [18]. The results are given in Figure 5.8. It can be noticed from Figures 5.7 and 5.8 that the Weibull modulus increases with the size of the specimen.

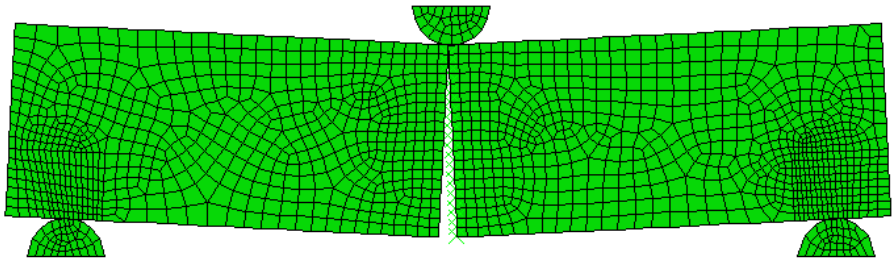

Figure 5.4: A fractured specimen model after three-point bend test.

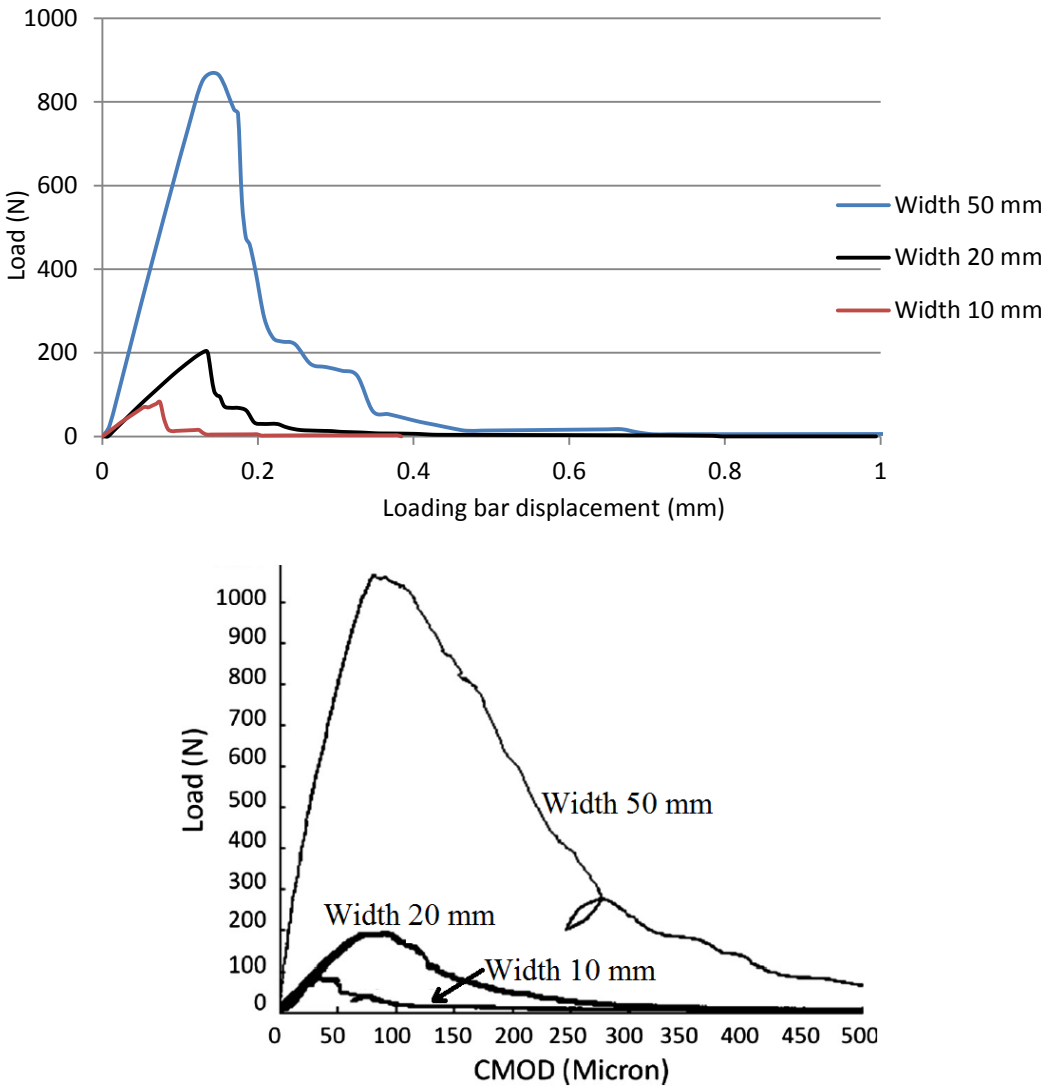

Figure 5.5: Predicted load-displacement curves of the notched specimens under 3-point bending (upper); Load-displacement curves determined experimentally (Li et al. [4]) (lower).

Table 5.8: The peak load, tensile strength and corresponding Weibull modulus for different groups of specimen models subjected to the tensile test.

Group	Peak load (P_{max}) Mean, Std (N)	Tensile strength (σ_t) Mean, Std (MPa)	Weibull modulus (m) (95% confidence interval)
I (largest)	23322.15, 1334.82	19.5, 1.1	21.2 (15.77, 28.48)
II	939.8, 92.9	18.8, 1.9	9.6 (7.48, 12.31)
III (smallest)	61.0, 12.7	18.7, 4.1	5.1 (3.9, 6.58)

Table 5.9: The peak load, flexural strength and corresponding Weibull modulus for different groups of un-notched specimen models subjected to the three-point-bending test.

Group	Peak load (P_{max}) Mean, Std (N)	Flexural strength (σ_b) Mean, Std (MPa)	Weibull modulus (m) (95% confidence interval)
I (largest)	5538.6, 418.9	26.6, 2.0	15.5 (11.8, 20.5)
II	1455.8, 153.7	28.0, 3.0	11.2 (8.4, 14.7)
III	255.6, 35.9	30.7, 4.3	7.55 (5.8, 9.8)
IV (smallest)	19.1, 3.2	36.7, 6.1	7.4 (5.6, 9.8)

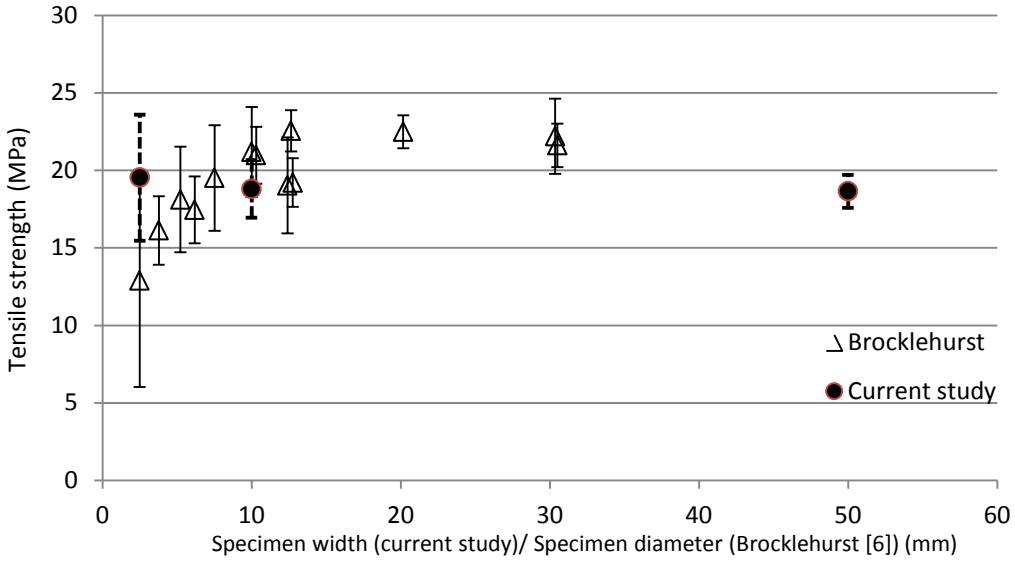

Figure 5.6: Variation of the mean tensile strength with the size of the specimens.

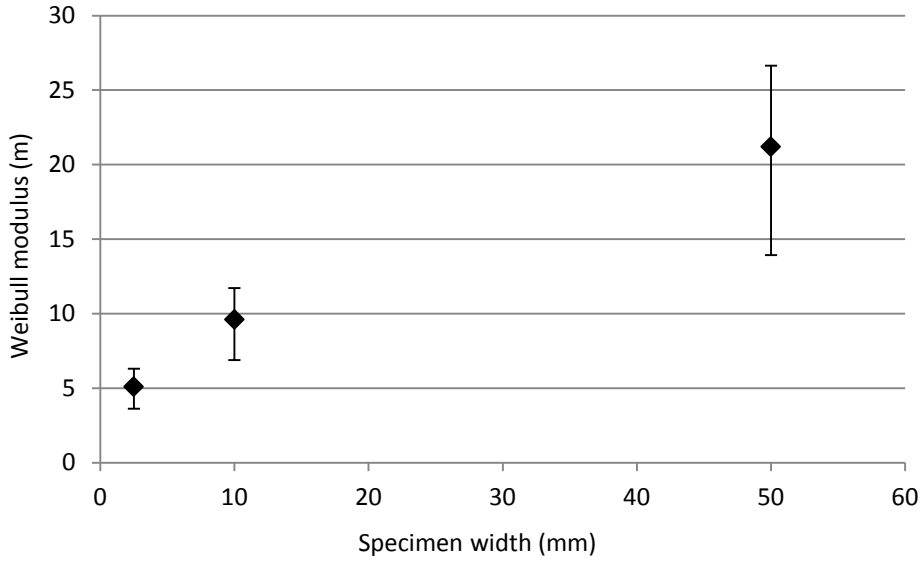

Figure 5.7: Variation of the predicted Weibull modulus for tensile strength distribution with the size of the specimens.

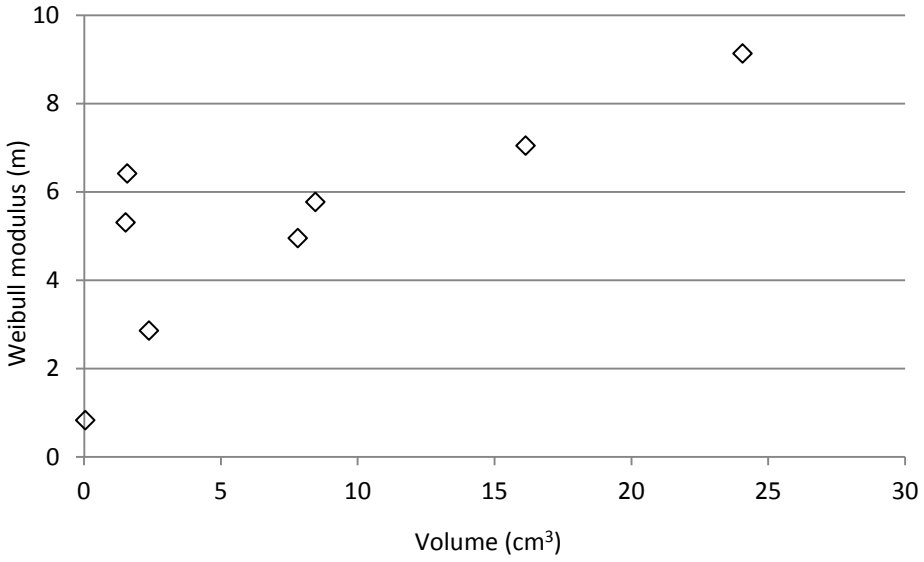

Figure 5.8: Variation of the experimental Weibull modulus for the tensile strength with the volume of the specimen (evaluated from data given by Brocklehurst [1]).

Figure 5.9 shows that the predicted mean flexural strength of the specimens decreased with an increase in their size. The results from the experimental work

conducted by Brocklehurst (1977) [1] are also provided for comparison. It can be noticed from Figure 5.9 that, while the general agreement between predictions and experiments were good, the reduction in the predicted flexural strength was greater when the size was smaller, and the effect diminished with further increases in the specimen size. In contrast, experimentally, the smaller specimens did not show a significant size effect. Variation in the predicted Weibull modulus for the flexural strength distribution with the size of the specimens is shown in Figure 5.10. Similar to that for the tensile strength distribution, the predicted Weibull modulus for the flexural strength seemed to increase with an increase in the specimen size. Data from Brocklehurst [1], however, did not show a clear trend for the standard deviation or Weibull modulus for the flexural strength with specimen size.

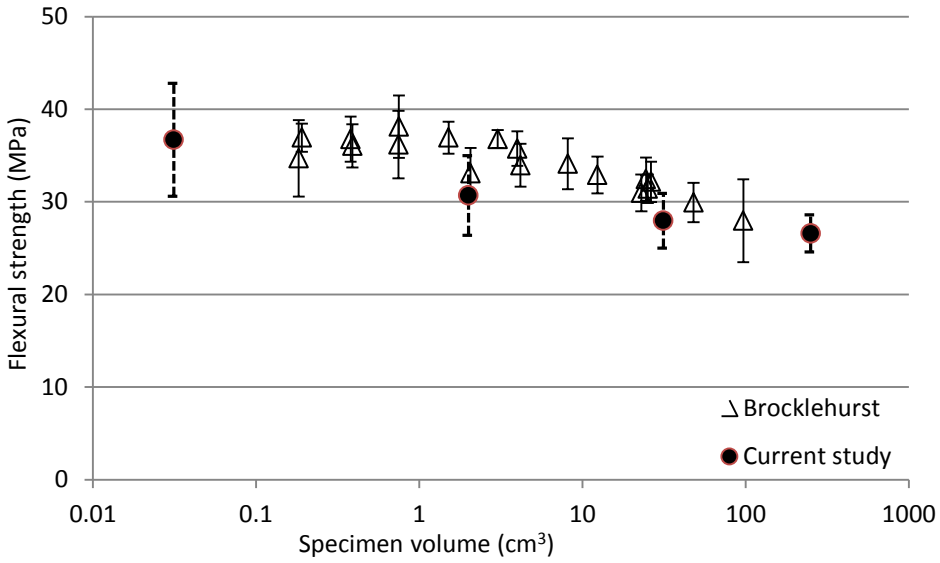

Figure 5.9: Variation of the mean flexural strength with the volume of the specimens.

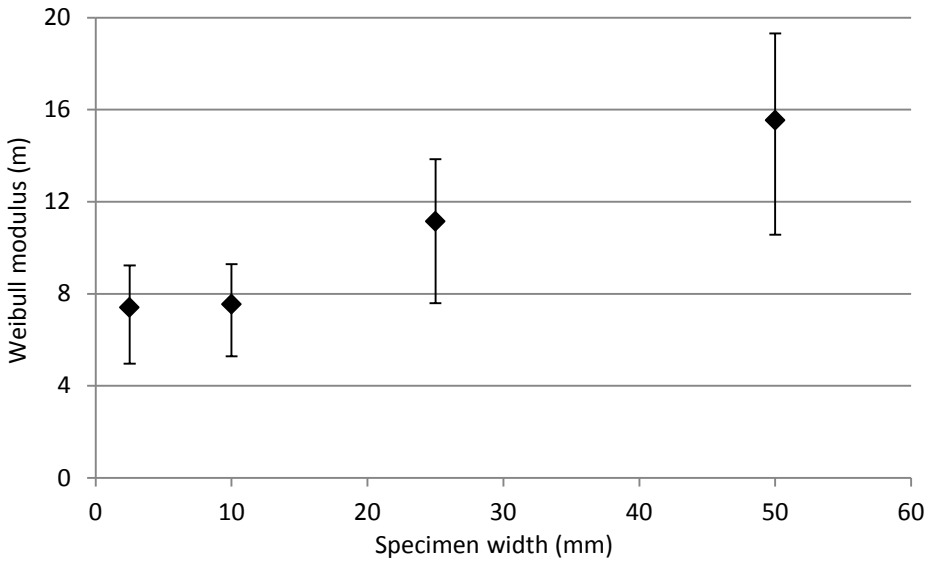

Figure 5.10: Variation of the predicted Weibull modulus for the flexural strength distribution with the size of the specimens.

Table 5.10 shows the predicted mean values of the peak loads and critical stress intensity factors for the three groups of notched specimens subjected to three-point bend test. The table also shows the corresponding values of the Weibull modulus for the critical stress intensity factor distribution. Figures 5.11 and 5.12 show that the predicted mean critical stress intensity factor and the associated Weibull modulus increased with the size of the specimens. The results from the experimental work conducted by Li et al. [4] are also provided in Figure 5.11 for comparison. The results indicated that there was more randomness in the critical stress intensity factor for the smaller specimens.

Table 5.10: Peak load, critical stress intensity factor and corresponding Weibull modulus for different groups of notched specimen models subjected to three-point bending test.

Group	Peak load (P_{max}) Mean, Std (N)	Critical stress intensity factor (K_{IC}) Mean, Std (MPa$\sqrt{m}$)	Weibull modulus (m) (95% confidence interval)
I (large)	1082.7, 57.9	1.59, 0.08	20.34 (15.6, 26.54)
II (medium)	196.67, 14.45	1.42, 0.10	18.3 (13.77, 24.29)
III (small)	71.4, 5.7	1.17, 0.09	12.1 (9.44, 15.41)

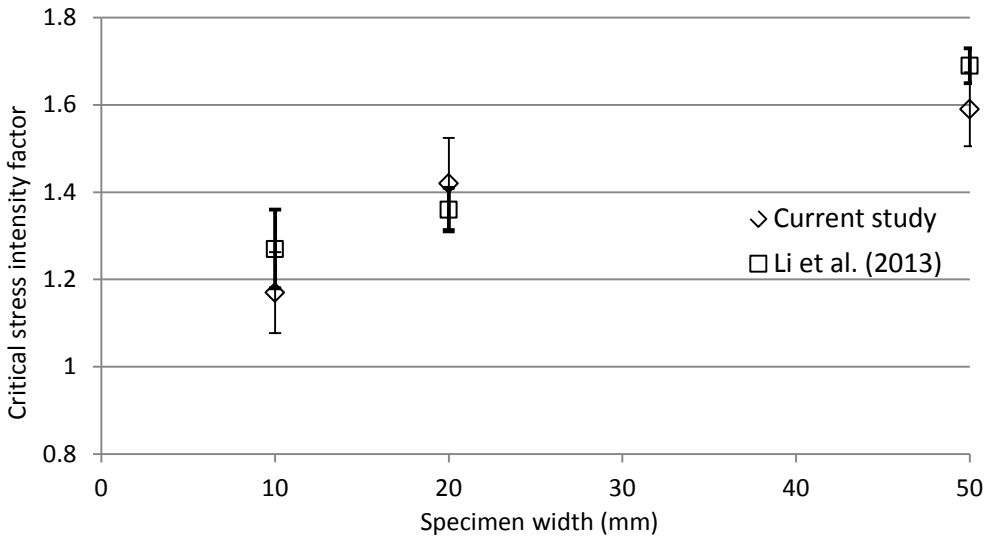

Figure 5.11: Comparison of variation of the mean critical stress intensity factor with the size of the specimens.

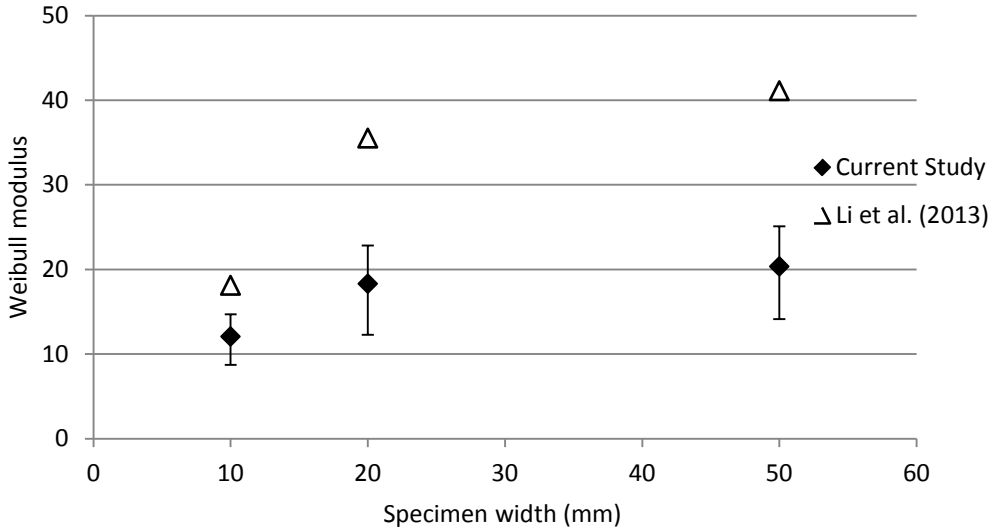

Figure 5.12: Variation of the predicted Weibull modulus for the critical stress intensity factor distribution with the size of the specimen.

5.4 DISCUSSION AND CONCLUSIONS

A numerical Monte Carlo approach based on continuum damage mechanics has been presented to study the effects of specimen size and material heterogeneity on the fracture properties of nuclear graphite. Tensile tests and three-point bend tests on graphite specimens of different sizes were simulated, and the fracture properties and their statistical variations were determined based on simple theories of mechanics and linear-elastic fracture mechanics.

It was found that the size of the specimens affected the predicted fracture properties significantly for the case of flexural testing, with the effect depending on the fracture property being considered as well as on the size range of the graphite specimens. The predicted tensile strength did not change significantly with an increase in the specimen size; whereas, experimentally, the smaller specimens showed lower tensile strengths. The predicted flexural strength decreased with an increase in the specimen size. This was in agreement with the experimental findings by Brocklehurst (1977). However, the numerical study showed that the size effect was more pronounced for specimens of smaller sizes, whereas the opposite was true with the experimental findings by Brocklehurst (1977). The Weibull modulus showed an increasing trend with an increase in the size of the specimens for both tensile and bend tests, indicating a reduction in the scatter of the results as the specimens become larger.

The fracture toughness (critical stress intensity factor) was found to increase with an increase in the size of the specimen. A similar trend was observed for the corresponding Weibull modulus for its distribution. This result was in accord with the experimental results obtained by Li et al. [4].

Defects of different sizes are present in the specimens and they give rise to the variation in fracture properties. In all the tests, the Weibull modulus increased with an increase in the size of the specimens. The increase in Weibull modulus with specimen size can be attributed to a decrease in the variability of the size of the defects which govern failure. As shown in Figure 5.13, the defects in a large specimen span over a larger range of size in comparison to smaller specimens. Thus, for larger specimens there is a greater probability for them to have the larger defects, and their failure, which will be governed by these defects only, will have a narrower distribution. In contrast, each of the smaller specimens will contain only a small portion of the entire defect population. Therefore, their failure will depend on the small as well as large defects, thus exhibiting a greater scatter and, hence, smaller Weibull modulus.

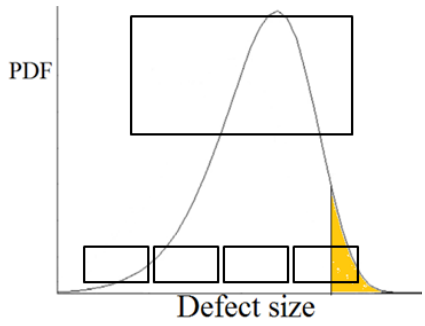

Figure 5.13: Schematic diagram showing that the defects in a large specimen (top) span over a larger range of size in comparison to smaller specimens (bottom).

It was also noted that if a greater variability was introduced to the flaw size distribution by decreasing the Weibull modulus for the intrinsic strength values assigned to the elements, it led to an increase in the variability of the bulk strength, i.e., the Weibull modulus corresponding to the bulk strength decreased.

When the strain gradient of the specimen increases, the number of elements, that fail prior to the load reaching its peak value, also increases. As a result, the variability in the failure load decreases. This fact can be illustrated with the help of a simple analogy of dice rolling. Each die represents an element, and the sum of the numbers represents the total strength. As can be noted from Figure 5.14, when the number of dice increases the probability distribution curve becomes narrower, i.e., the probability density distribution becomes more 'concentrated' at the mean value and the spread (variability) decreases.

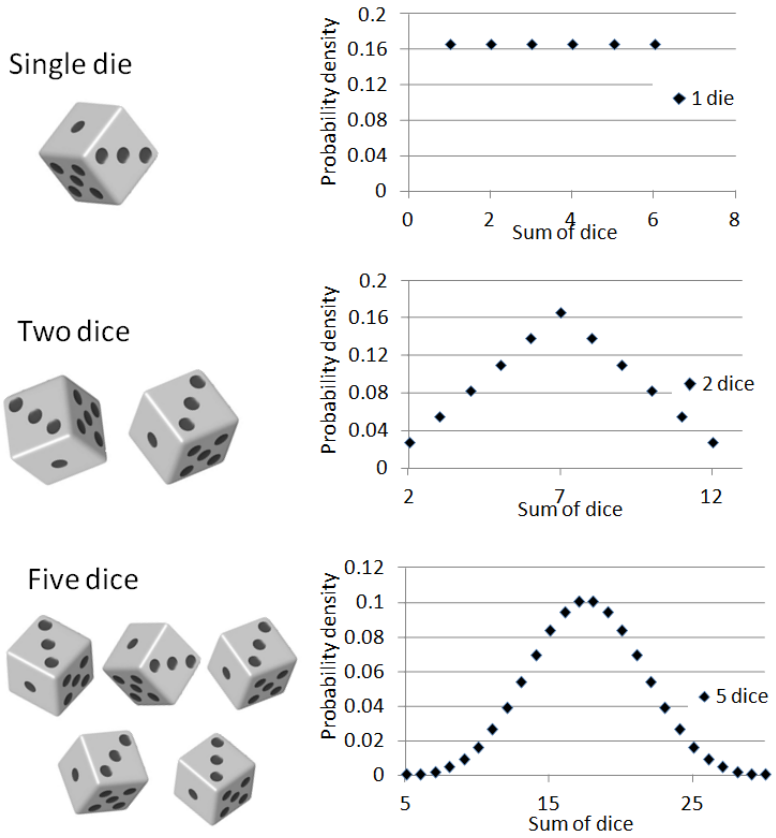

Figure 5.14: As the number of dice increases the variability in the random variable 'sum of dice' decreases.

The numerical approach presented herein seems to be able to reproduce the size effect in nuclear graphite. As mentioned previously, using the simple beam theory, Li and Fok [8] showed that the post-peak stress-retention capability of quasi-brittle materials such as nuclear graphite could produce a bend strength that was higher than the tensile strength. The effect was similar to that of plasticity in metals. By using a Monte Carlo analysis, they also showed that the Weibull modulus changed with the strain gradient: the higher the strain gradient, the higher the Weibull modulus, as found in experiments. However, their simulation used specimens that had uniform material properties, even though each specimen was given different properties generated randomly. The predicted increase in the Weibull modulus with the strain gradient was also much lower than that found experimentally. The current work extended their approach by taking into account the material heterogeneity in nuclear graphite. Not only can the new approach simulate the effect of strain gradients, it can also reproduce the effect of the specimen size on the bend strength, as well as the critical stress intensity factor. However, the predicted Weibull modulus for the notched beams was still too low. Therefore, further studies need to be carried out to make refinements to the approach. The expected outcome of such studies is a better understanding about the effect of component size on fracture properties, leading to more accurate failure predictions.

5.5 REFERENCES

1. J.E. Brocklehurst, Fracture in Polycrystalline Graphite, Chemistry and Physics of Carbon, New York, NY, 13, 146–272, 1977.
2. R.J. Price, Statistical Study of the Strength of Near-Isotropic Graphite, General Atomic Project 3224 (GA–A13955 and UC–77), 1976.

3. J.P. Strizak, The Effect of Volume on the Tensile Strength of Several Nuclear-Grade Graphites, The Status of Graphite Development for Gas Cooled Reactors, IAEA–TECDOC–690, 233–241, 1991.
4. H. Li, J. Li, G. Singh and A. Fok, Fracture Behavior of Nuclear Graphite NBG-18, Carbon, 60, 46-56, 2013.
5. G. Quinn, Advanced Structural Ceramics: A Round Robin, Journal of the American Ceramic Society, 73(8), 2374-2384, 1990.
6. K. Matsusue, K. Takahara, and R. Hashimoto, Strength Evaluation of Hot-Pressed Silicon Nitride at Room Temperature, Yogyo Kyokaishi, 90(4), 168, 1982.
7. Y. Katayama and Y. Hattori, Effects of Specimen Size on Strength of Sintered Silicon Nitride, Journal of American Ceramic Society, 65(10), C-164-C-165, 1982.
8. H. Li and A.S.L. Fok, An Analytical Study on the Effects of Strain Gradient on the Fracture Statistics of the Quasi-Brittle Materials, Journal of Nuclear Materials, 394, 136-143, 2009.
9. D.S. Dugdale, Yielding of Steeel Sheets Containing Slits, Journal of Mechanics and Physics of Solids, 8, 100-108, 1960.
10. G.I Barenblatt, The Mathematical Theory of Equilibrium of Cracks in Brittle Fracture, Advances in Applied Mechanics, 7, 55-129, 1962.
11. Z. Zou, S.L. Fok, S.O. Oyadiji, and B.J. Marsden, Failure Predictions for Nuclear Graphite Using a Continuum Damage Mechanics Model, Journal of Nuclear Materials, 324, 116-124, 2004.
12. Abaqus Documentation, Simulia Dassault Systemes, RI, USA.
13. T. Burchell, Neutron Irradiation Damage in Graphite and Its Effects on Properties, Oak Ridge National Lab, Oak Ridge, TN, USA.
14. J.M. Vidal and T.J. Mays, Mechanical Properties and Oxidation of Nuclear Graphites, University of Bath, UK.
15. W. Weibull, A Statistical Theory of the Strength of Materials, Proc. Royal Swedish Academy of Eng. Sci., 151, 1-45, 1939.
16. W. Weibull, A Statistical Distribution Function of Wide Applicability, Journal of Applied Mechanics, 18, 293-297, 1951.
17. ASTM, Standard Test Method for Determination of Fracture Toughness of Graphite at Ambient Temperature, ASTM-D7779-11, 2012.
18. G. Jianhong and Y. Li, Relationship between the Estimated Weibull Modulus and the Coefficient of Variation of the Measured Strength for Ceramics, J. Am. Ceram. Soc., 82(2), 449-452, 1999.

6. ESTIMATING STRESSES IN THE VHTR COMPONENTS

This chapter extends the application of the explicit crack modeling approach to estimating failure in Very High Temperature Reactor (VHTR) core components which are made of graphite – a quasi-brittle material. For modeling fracture in the VHTR components, the stress distribution as a function of time is required. This chapter presents the development, verification and implementation of the constitutive model of graphite for modeling stresses in the VHTR components.

6.1 VERY HIGH TEMPERATURE REACTOR SYSTEM

It is expected that by the end of 2050 the world population will increase from the current 7 billion to 9 billion [1]. With the increase in population the energy needs of the world will also increase. The nuclear industry provides for 16% of the total electricity [2], having the largest share among the nongreen-house gas emitting sources. In an effort to continue to expand the capability of nuclear energy systems to provide energy in a clean, sustainable, cheap and safe manner, Generation IV nuclear energy systems are being planned by the Generation IV International Forum (GIF) which is represented by 10 major nations of the world. Generation IV nuclear energy systems not only refer to the nuclear reactors but they also include the energy conversion systems and the necessary facilities for the entire fuel cycle from ore extraction to final waste disposal [3]. These nuclear energy systems are expected to be in operation around 2040.

The Very High Temperature Reactor System (VHTR) is one of the six future reactor systems selected by GIF. The VHTR system uses a thermal neutron spectrum and a uranium cycle for power generation. Although the system can produce electricity, it is primarily aimed at high temperature process heat applications such as coal gasification and thermo-chemical hydrogen production with superior efficiency. In a VHTR, the coolant outlet temperature will be 1000°C or higher, thus allowing more efficient electricity generation and better conditions for process heat applications [4].

The VHTR system design is based on the two current High Temperature Gas-Cooled Reactor (HTGR) systems: Gas Turbine – Modular Helium Reactor (GT-MHR) and Pebble Bed Modular Reactor (PBMR). The design of GT-MHR is also known as the prismatic design. Figures 6.1 and 6.2 show the designs of the cores of these two types of reactors.

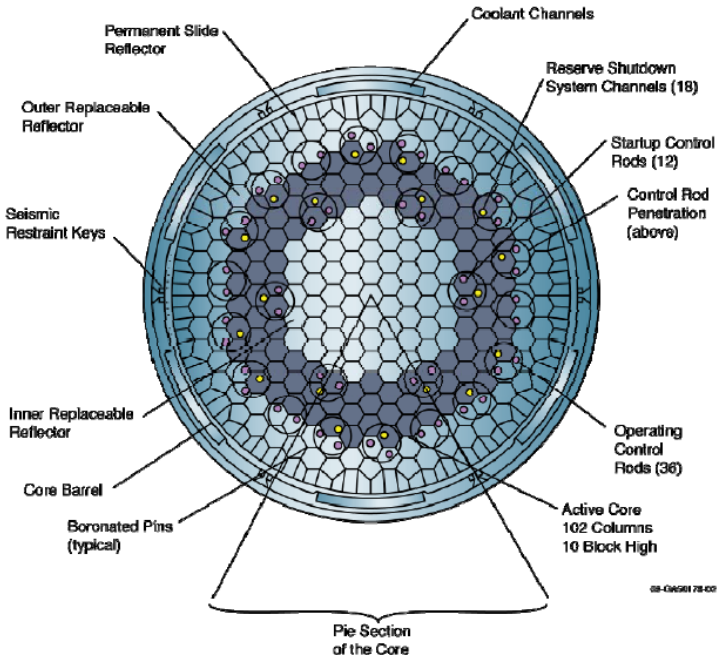

Figure 6.1: Conceptual design of a GT-MHR core.

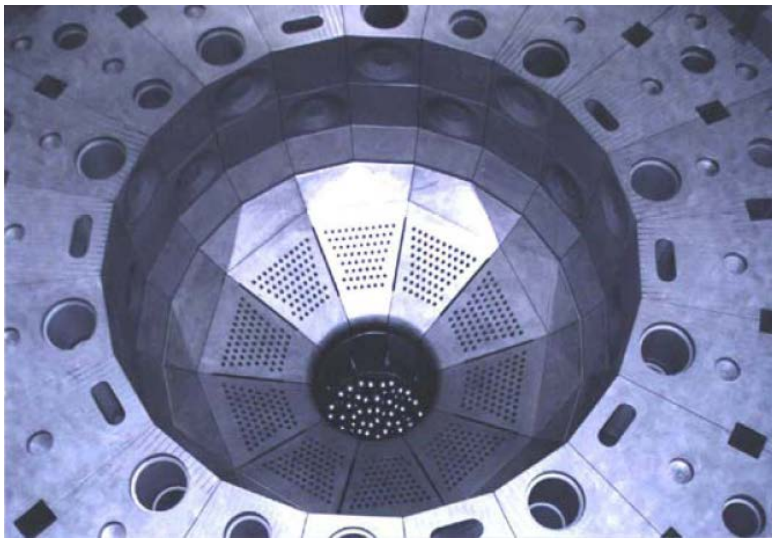

Figure 6.2: Lower core internal of HTR-10 (a Pebble Bed test reactor located in China).

6.2 LIMITATIONS OF NUCLEAR GRAPHITE

A major portion of the reactor core is made up of graphite, which is a polycrystalline material having excellent mechanical and thermal properties at high temperature, making it suitable for several engineering applications. Depending on the reactor design, hexagonal (for the prismatic reactor core) or trapezoidal (for the pebble-bed reactor core) graphite bricks will be stacked together to form the reactor core. These graphite bricks not only act as structural components but also provide path for control rods and coolant gases. Therefore, the structural integrity of these graphite bricks is very important.

When graphite is exposed to fast neutrons released during the fission process, its dimensions and physical properties (Young's modulus, coefficient of thermal expansion, creep coefficient, etc.) change. In some gas-cooled reactors, the graphite also undergoes radiolytic oxidation. Due to non-uniform exposure to neutron irradiation, the dimensional changes and changes in physical properties are also non-uniform, which leads to the

build-up of stresses and possible fracture in the graphite bricks. These in turn can lead to problems with movement of control rods and leakage of coolant gases [6]. In the pebble bed reactor, the problem is more serious as the core structure cannot be replaced. Thus, it becomes imperative to assess the integrity of graphite bricks under irradiation.

6.3 Assessing Structural Integrity of Graphite Bricks

Several research studies have been conducted in the past with a focus on assessing the structural integrity of graphite bricks used in nuclear reactors. Smith [7] conducted a study directed towards improving the accuracy of finite-element based stress analysis of a multiple-holed moderator graphite brick of the HTGR. Using a code named TWOD, graphite bricks with multiple holes were analyzed for the stresses. The stress analysis incorporated thermal strains, irradiation-induced strains and seismic loads. Graphite was considered to be a linear viscoelastic material with its properties dependent on the temperature and irradiation. The study presented the limitations of various approximation techniques commonly used for performing the stress analysis.

Smith and Pelessone [7] presented a method named as consistent linearization for performing the viscoelastic analysis using the finite element method (FEM). The authors illustrated the method by conducting a stress analysis of a graphite fuel brick of the HTGR under irradiation. The Kelvin-Maxwell viscoelastic model was employed to simulate the mechanical response of graphite. Besides elastic strain, the model included steady-state and transient creep strains due to irradiation and thermal creep strain.

Iyoku et al. [8] developed a code for performing stress analysis of graphite bricks in the High-Temperature Engineering Test Reactor (HTTR). The code, named as

VIENUS, incorporated the visco-elastic behavior of graphite and considered the influence of both irradiation and temperature on the material properties. VIENUS was verified for accuracy by comparing its predictions with the irradiation test results of Peach Bottom fuel elements. The study also established that the irradiation induced creep strain and the dimensional change strain were the two most important parameters which influenced the stresses.

Yu et al. [6] used FEM to compute the stresses in a HTR-10 (a test reactor of the pebble bed design) reflector brick and evaluated the failure probability using the Weibull model [10] [11]. The dependence of physical properties, including the thermal conductivity, thermal expansion coefficient, creep coefficient and elastic modulus, on temperature and fast neutron dose was incorporated in the FE code. The failure probability was evaluated as a function of time under the normal conditions of operation as well as during the cold shutdown conditions. It was reported that the failure probability of the graphite brick after 20 years of operation was 2.3×10^{-12} under the normal operating conditions and 4.7×10^{-11} under the cold shutdown conditions. The details of the constitutive law and the material properties used in the analysis were not provided.

Li et al. [12] conducted an analytical study for evaluating the axial and hoop stresses in a hypothetical cylindrical moderator brick as a function of time. The effect of the irradiation creep strain, dimensional change strain and elastic strain on the stresses was included. It was found that in the outer region of the brick the hoop and the axial stresses were compressive in nature initially but gradually turned tensile and thereafter continued to increase. In the inner region of the brick the stresses were tensile initially, gradually turned compressive and thereafter continued to increase in magnitude. The

nature of the stresses (tensile/compressive) changed after a period of about 20 years. The analytical results were compared with the finite element results and were found to be in good agreement.

Tsang et al. [13] presented a constitutive model which describes the complex behavior of graphite under irradiation and high temperature. The model included the elastic strain ($\boldsymbol{\varepsilon}^{e}$), primary ($\boldsymbol{\varepsilon}^{pc}$) and secondary ($\boldsymbol{\varepsilon}^{sc}$) creep strains, thermal strain and dimensional change strain ($\boldsymbol{\varepsilon}^{dc}$). Besides these strains, the interaction thermal strain ($\boldsymbol{\varepsilon}^{ith}$) and interaction dimensional change strain ($\boldsymbol{\varepsilon}^{idc}$), which are caused by creep, were also included in the model. The elastic strain was obtained from the total strain ($\boldsymbol{\varepsilon}^{total}$) which was expressed as the sum of all these strains. The stresses ($\boldsymbol{\sigma}$) and their increments ($\Delta\boldsymbol{\sigma}$) were obtained using the elastic strain according to Hooke's law of linear elasticity. The following equations show the mathematical relations between strains and stresses.

$$\boldsymbol{\varepsilon}^{total} = \boldsymbol{\varepsilon}^{e} + \boldsymbol{\varepsilon}^{pc} + \boldsymbol{\varepsilon}^{sc} + \boldsymbol{\varepsilon}^{dc} + \boldsymbol{\varepsilon}^{th} + \boldsymbol{\varepsilon}^{idc} + \boldsymbol{\varepsilon}^{ith} \tag{6.1}$$

$$\boldsymbol{\sigma} = \mathbf{D}\boldsymbol{\varepsilon}^{e} \tag{6.2}$$

$$\Delta\boldsymbol{\sigma} = \check{\mathbf{D}}\Delta\boldsymbol{\varepsilon}^{e} + \Delta\mathbf{D}\boldsymbol{\varepsilon}^{e} \tag{6.3}$$

where $\mathbf{D}$ is the stiffness of the material, $\check{\mathbf{D}}$ is the stiffness before the increment and $\Delta\mathbf{D}$ is the increment in the stiffness. The model was solved for stresses in a one-eighth section of a three-dimensional cylindrical brick using the finite element software Abaqus and its User Material subroutine UMAT. A turnaround in the stresses (tensile to compressive and vice versa), as observed in the analytical solution by Li et al. [12], was observed. It was also found that there was a rapid increase in the magnitude of the hoop stresses during reactor shutdown.

Mohanty et al. [14] developed a code for performing coupled thermal-structural analysis of graphite core components under high temperature and irradiation conditions. Some preliminary results of the stress analysis for a prismatic fuel brick have been presented in [14]. Temperature variation has not been considered in the work presented.

Wang et al. [15] used the code INET-GRA3D developed by the Institute of Nuclear Energy Technology (INET), which was capable of performing three-dimensional analysis, to evaluate the structural integrity of a side reflector HTR brick. The code was based on the user subroutine of the commercial software MSC.MARC. The stress analysis included the thermal strain, primary and secondary creep strains and irradiation-induced dimensional change strain. The effect of irradiation and temperature on material properties was also included in the analysis. A series of sensitivity tests were conducted for addressing the uncertainties in the failure predictions that arose from the limited irradiation test data, temperature conditions and creep parameters. The results of the sensitivity tests indicated that the temperature conditions and creep parameters affected the failure probability appreciably. Two different materials, ASR-1RS and ATR-2E, were considered and it was confirmed that the maximum shrinkage strain was not the only important factor which determined the service lives of the graphite components.

Mohanty et al. [16] also performed a stress analysis of a HTGR prismatic graphite reflector brick. The material of the brick was assumed to be H-451 graphite. The irradiation and temperature conditions were based on the GT-MHR (Gas Turbine-Modular Helium Reactor). Primary irradiation-creep strain, which is negligible in comparison to the secondary irradiation-creep strain, was neglected. Finer details like dowel pins and holes were not considered in the geometry of the brick. Two temperatures

were considered in the analysis: 600°C and 900°C, and temperatures were assumed to remain constant. The stresses were predicted for the time duration of 7 years. Based on the comparison of the numerically-evaluated maximum stress with the strength of the irradiated graphite, the study concluded that the reflector brick may be able to survive for at least two fueling cycles, with each cycle 3 years long.

6.4 CONSTITUTIVE MODEL FOR GRAPHITE AND ITS IMPLEMENTATION IN FEM

A constitutive model for the irradiation behavior of nuclear graphite under high temperature and irradiation was constructed and implemented as User Material (UMAT) subroutines in the commercial finite element software Abaqus. The strain components of the model included the irradiation-induced dimensional change strain, thermal strain, creep strain and elastic strain. Changes in the dimensions and material properties (Young's modulus, creep coefficient, coefficient of thermal expansion, etc.) with irradiation dose and temperature were based on the existing data for nuclear graphite available in the literature. The UMAT was verified by comparing the numerical predictions for the stresses in a cylindrical AGR (Advanced Gas-Cooled Reactor) graphite brick with the analytically evaluated stresses.

Constitutive Model

The constitutive model for the irradiation behavior of nuclear graphite was constructed using the following equations:

$$\Delta\boldsymbol{\varepsilon}^{total} = \Delta\boldsymbol{\varepsilon}^{e} + \Delta\boldsymbol{\varepsilon}^{pc} + \Delta\boldsymbol{\varepsilon}^{sc} + \Delta\boldsymbol{\varepsilon}^{dc} + \Delta\boldsymbol{\varepsilon}^{th} \qquad (6.4)$$

$$\boldsymbol{\sigma} = \mathbf{D}\boldsymbol{\varepsilon}^{e} \qquad (6.5)$$

$$\Delta\boldsymbol{\sigma} = \check{\mathbf{D}}\Delta\boldsymbol{\varepsilon}^{e} + \Delta\mathbf{D}\boldsymbol{\varepsilon}^{e} \quad (6.6)$$

$$\boldsymbol{\varepsilon}^{pc} = 4.0 \exp(-4\gamma)\int_0^{\gamma} \frac{\sigma}{E_c}\exp(4\gamma')d\gamma' \quad (6.7)$$

$$\boldsymbol{\varepsilon}^{sc} = 0.23\int_0^{\gamma} \frac{\sigma}{E_c}d\gamma' \quad (6.8)$$

$$\boldsymbol{\varepsilon}^{dc} = F(\gamma,T) \quad (6.9)$$

$$\boldsymbol{\varepsilon}^{th} = \alpha(\gamma,T)(T - T_o) \quad (6.10)$$

$$E = H(\gamma,T) \quad (6.11)$$

$$E_c = I(\gamma,T) \quad (6.12)$$

where Equation 6.4 shows that the total strain consists of the elastic strain ($\boldsymbol{\varepsilon}^{e}$), primary creep strain ($\boldsymbol{\varepsilon}^{pc}$), secondary creep strain ($\boldsymbol{\varepsilon}^{sc}$), dimensional change strain ($\boldsymbol{\varepsilon}^{dc}$) and thermal strain ($\boldsymbol{\varepsilon}^{th}$). In Equations 6.5 and 6.6, **D** is the stiffness matrix of the material defined by the Young's modulus and Poisson's ratio, and $\check{\mathbf{D}}$ is the mean value of **D** in the current increment. These relations were used to define the Jacobian matrix ($\mathbf{C} = \partial\Delta\boldsymbol{\sigma}/\partial\Delta\boldsymbol{\varepsilon}$). The Jacobian was used in the UMAT to calculate the increment in stresses $\Delta\sigma$ and update the stresses in each increment of time. Equations 6.7 and 6.8 define the primary and secondary creep strain, respectively. As shown in Equations 6.9 to 6.12, the dimensional change strain, thermal strain, dynamic Young's Modulus and creep Young's Modulus are functions of irradiation dose (γ) and temperature (T). The dependence of the coefficient of thermal expansion (α), Young's modulus (E) and creep Young's modulus (E_c) on irradiation dose and temperature was also incorporated.

Verification of UMAT

Verification of the UMAT was performed by comparing the stresses predicted for a cylindrical AGR (Advanced Gas-Cooled Reactor) graphite brick with the analytically

evaluated stresses available in the literature [12]. To reduce the computational cost, only a section of the cylinder was considered based on symmetry. Figure 6.3 shows the meshed model of the graphite cylinder section.

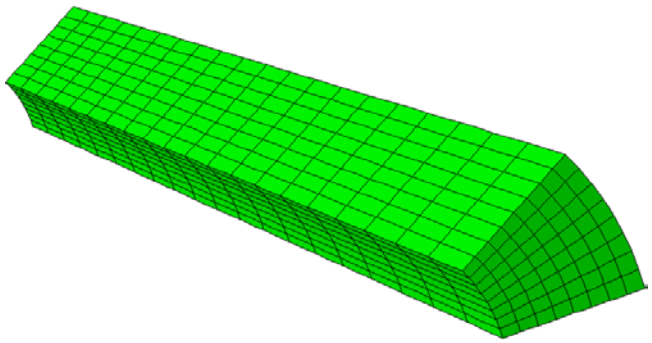

Figure 6.3: Meshed model of the graphite cylinder section.

The FE model of the cylinder section comprised 6345 nodes and 1280 C3D20 elements, which are 3D quadratic isoparametric elements with 20 nodes. Boundary conditions were applied to enforce symmetry about the longitudinal axis. The temperature was kept constant while the irradiation dose increased linearly with time. The irradiation dose level was highest at the inner surface of the cylinder and it decreased linearly with the radial distance as shown in Figure 6.4. The primary creep strain was neglected as it was very small relative to the secondary creep strain. The brick was considered to operate for 30 years.

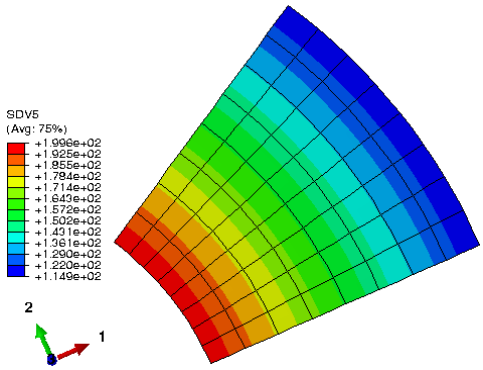

Figure 6.4: Variation of irradiation dose (10^{20} n/cm^2) in the cylindrical section with the radial distance after 30 years.

The model was analyzed using Abaqus/Standard and the results are shown in Figures 6.5 to 6.9. Figures 6.5 and 6.6 show the hoop and axial stress distributions, respectively, within the cylinder after 15 years.

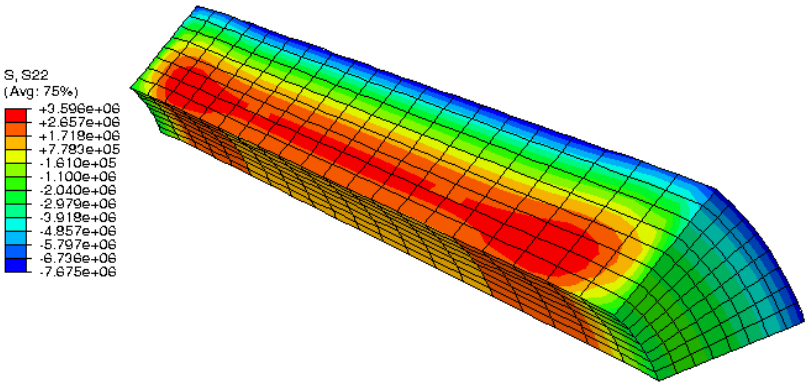

Figure 6.5: Hoop stress distribution after 15 years.

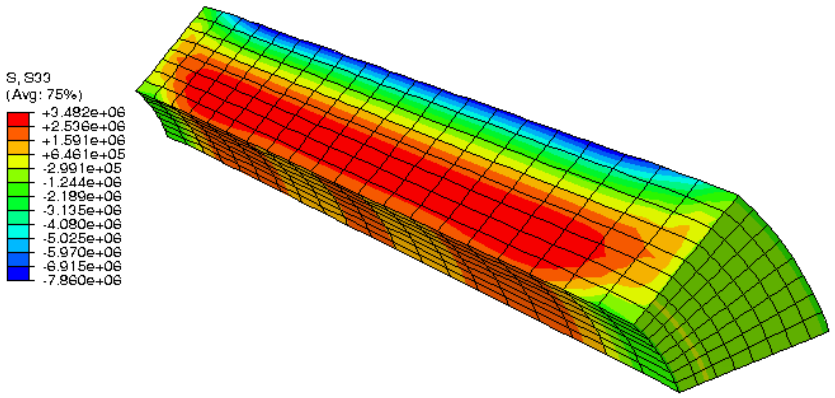

Figure 6.6: Axial stress distribution after 15 years.

Figures 6.7 and 6.8 show the curves of the hoop and axial stress versus time, respectively, at the inner and outer surfaces of the cylinder. The figures also show the comparison of the numerically predicted stresses with the analytically evaluated stresses.

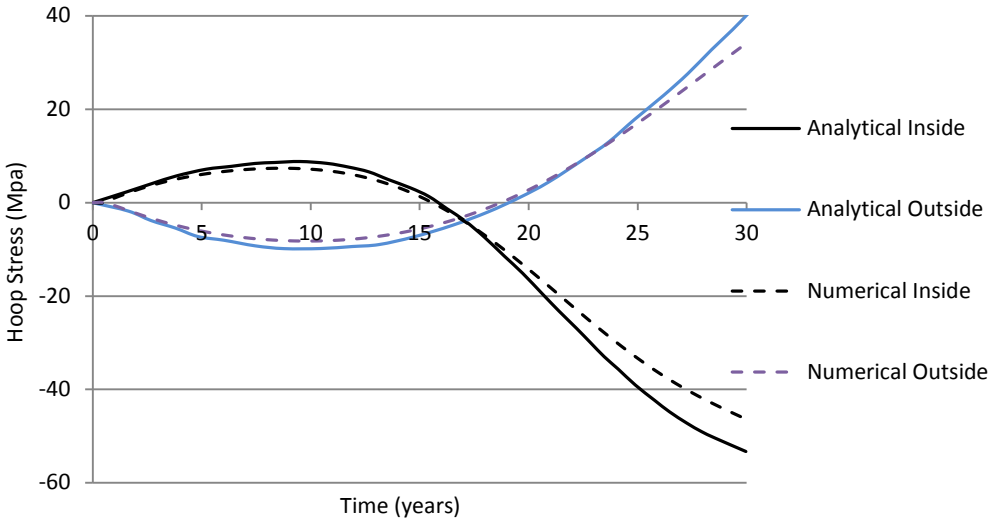

Figure 6.7: Hoop stresses versus time at the inner and outer surfaces.

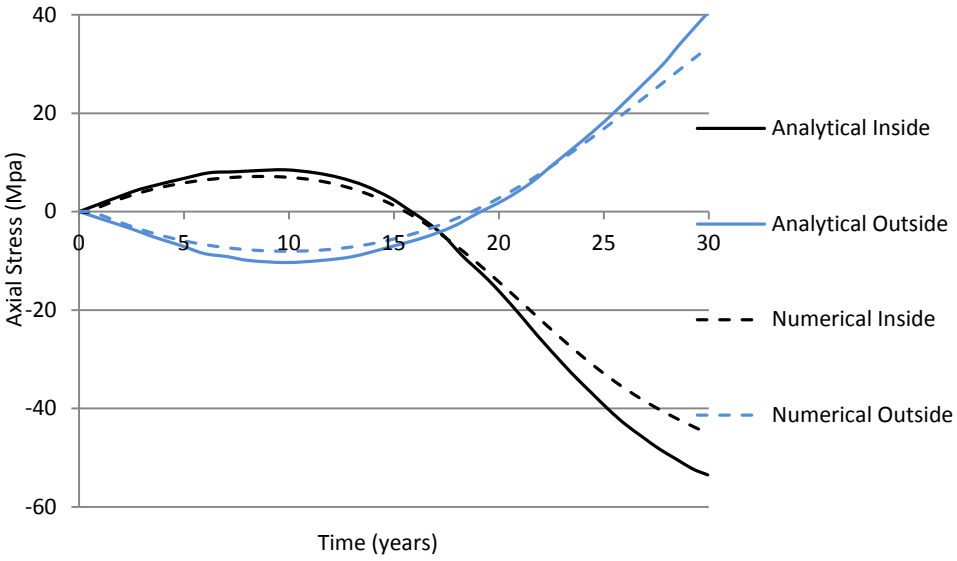

Figure 6.8: Axial stresses versus time at the inner and outer surfaces.

As can be seen from the figures, the numerically predicted stresses using the UMAT were found to be in good agreement with the analytically evaluated stresses, thus, establishing the capability of the developed UMAT to evaluate stresses accurately in nuclear graphite bricks subjected to irradiation and high temperature.

6.5 Modeling Residual Stresses in VHTR Graphite Components

The developed UMAT was employed to carry out a stress analysis for a HTR brick. Considering the symmetry of the HTR graphite brick, only a quarter of the brick was analyzed to minimize the computational cost (see Figure 6.9). The HTR brick model was meshed with the C3D20R element, which is a 3D quadratic isoparametric element with 20 nodes with reduced integration. The model contained 17398 nodes and 3640 elements. Boundary conditions to enforce symmetry about the horizontal and vertical

mid-planes were applied. Also, one of the corner nodes near the center of the core was constrained in all directions to avoid rigid body motion.

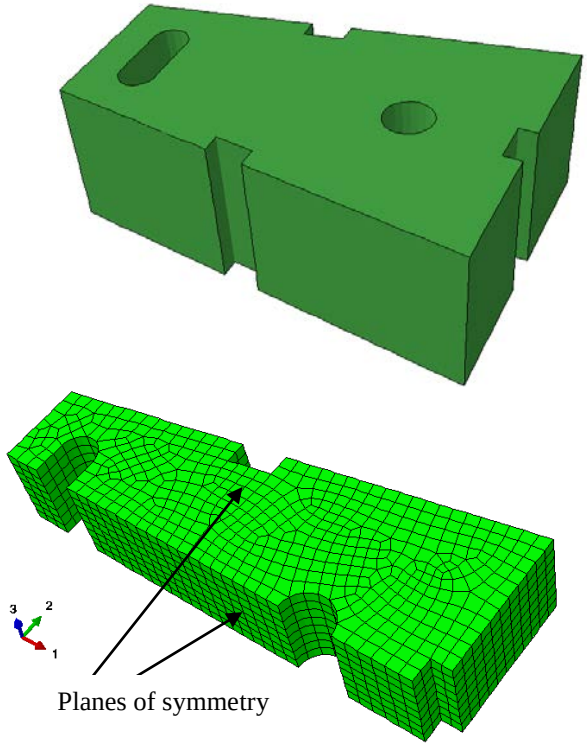

Figure 6.9: A full model (top) and a meshed quarter model (bottom) of the HTR graphite brick.

Load and Boundary Conditions

The brick was subjected to load and boundary conditions which represented those in the HTR. Due to the unavailability of data in the literature, some assumptions were made, as explained later. The equations for the model are given below:

$$\gamma = (p_1 + p_2 x)t \tag{6.13}$$

$$T = (q_1 + q_2 x) \tag{6.14}$$

$$\alpha = a_1\gamma^2 + a_2\gamma + a_3 \tag{6.15}$$

$$\boldsymbol{\varepsilon}^{dc} = (b_1\gamma^5 + b_2\gamma^4 + b_3\gamma^3 + b_4\gamma^2 + b_5\gamma + b_6)\, f_\varepsilon \tag{6.16}$$

$$\text{where } f_\varepsilon = c_4T^2 + c_5T + c_6 \tag{6.17}$$

$$Y = (d_1\gamma^5 + d_2\gamma^4 + d_3\gamma^3 + d_4\gamma^2 + d_5\gamma + d_6)\, f_Y \tag{6.18}$$

$$\text{where } f_Y = (e_1T^5 + e_2T^4 + e_3T^3 + e_4T^2 + e_5T + e_6) \tag{6.19}$$

$$\boldsymbol{\varepsilon}^c = 0.23\int_0^\gamma \frac{\sigma}{E_c} d\gamma' \tag{6.20}$$

$$E_c = (f_1\gamma^5 + f_2\gamma^4 + f_3\gamma^3 + f_4\gamma^2 + f_5\gamma + f_6) \tag{6.21}$$

$$\boldsymbol{\varepsilon}^{th} = \alpha\Delta T \tag{6.22}$$

The neutron dose (γ) at any point in the brick was assumed to be a function of time (t) and the distance from the center of the core, as shown in Equation 6.13 where x represents the radial distance from the core center, and t represents time and p and q are constants. Irradiation dose was assumed to decrease linearly with distance and increase linearly with time. It was assumed that the reactor would operate for 30 years.

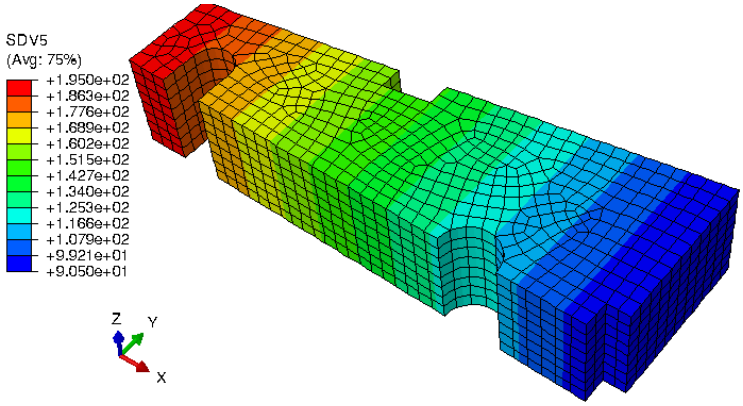

Figure 6.10: Assumed distribution of irradiation dose (10^{20} n/cm^2) in the HTR graphite brick at 17th year.

A temperature (T) gradient was also assumed to be present in the HTR graphite brick, as given by Equation 6.14. Temperature was highest at the face closest to the core

center and decreased linearly with distance from it. The dependence of the coefficient of thermal expansion (α) on the dose and temperature was considered. The relation was obtained by fitting a quadratic curve to the experimental data available in [17]. Similarly, the dependence of the dimensional change strain ($\boldsymbol{\varepsilon}^{dc}$) on dose at 600°C was obtained by fitting a polynomial curve of 5th degree to the data presented in [18]. The dimensional change strains at temperatures 380°C and 1200°C were obtained from [19] and [20]. However, since the data at other temperatures was available for low dose only, the temperature dependence of the dimensional change strain had to be extrapolated.

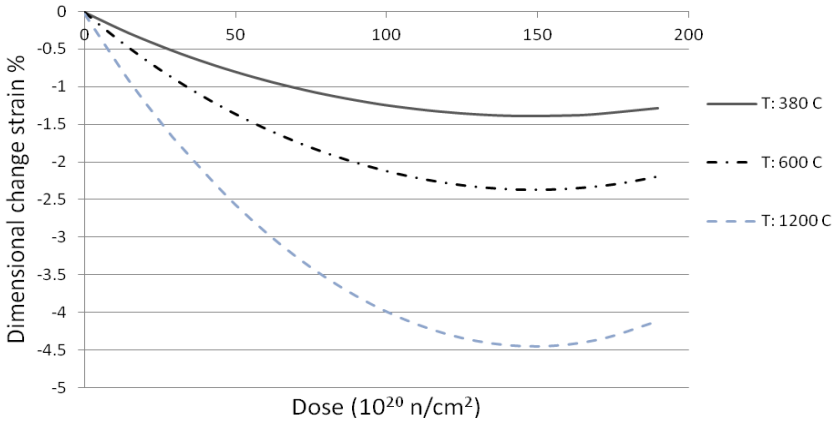

Figure 6.11: Assumed variation of dimensional change strain with neutron dose at different temperatures.

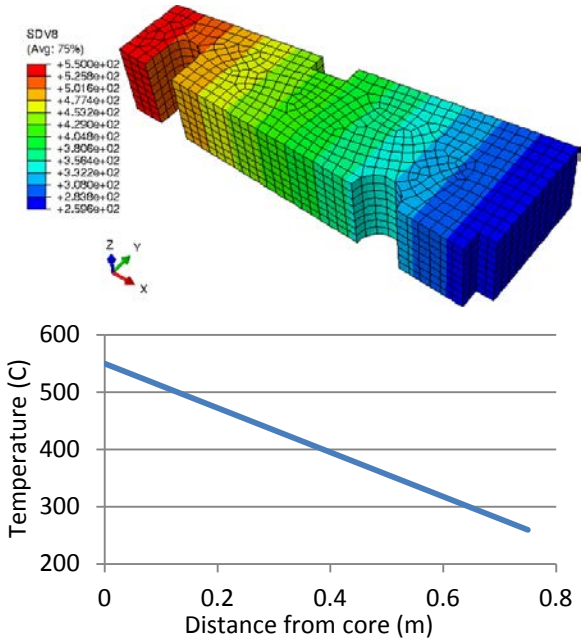

Figure 6.12: Assumed variation of temperature (°C) in the HTR graphite brick with distance from the core.

Young's modulus's (Y) variation with dose was based on the data presented in [18], while the temperature dependence of Young's modulus (f_Y) was taken from [21]. 5th order polynomial curves were used to fit both sets of data. The combined dependence is shown in Equations 6.16 and 6.19. Creep strain (ε^C) variation with dose was also considered in the analysis. However, due to insufficient data for either IG 110 or IG 11, candidate graphites for the HTR, the creep strain data of graphite used in the Advanced Gas-cooled Reactor (AGR) were used. The dependence of the creep strain and creep Young's modulus (E_c) on dose is shown in Equations 6.20 and 6.21, respectively. The relation of thermal strain to temperature is shown in Equation 6.22. The values of the constants involved in equations 6.13-6.22 are given in Appendix A.

Results

The brick model was analyzed using Abaqus/standard and the results are shown in Figures 6.13 to 6.21. Figures 6.13, 6.14, 6.15 and 6.16 show the radial, hoop, axial and maximum principal stress distributions, respectively, within the HTR brick after 30 years of irradiation.

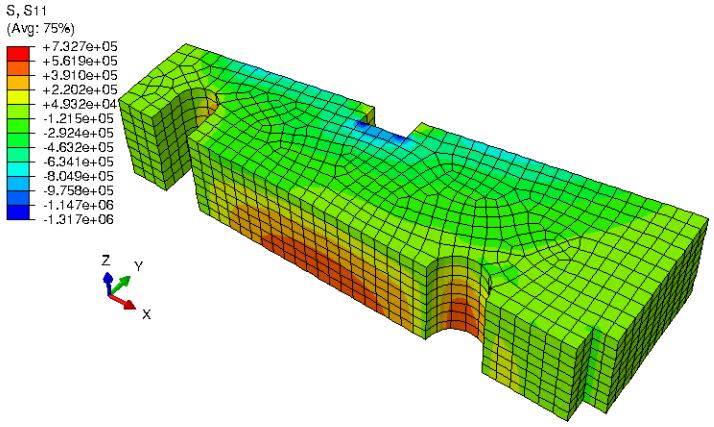

Figure 6.13: Radial stress distribution after 30 years.

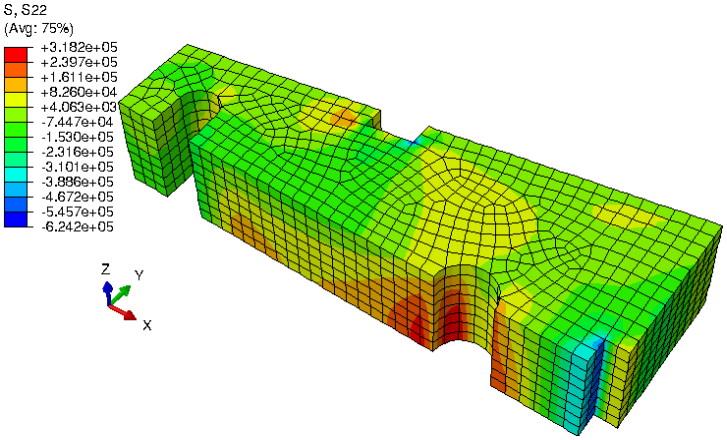

Figure 6.14: Hoop stress distribution after 30 years.

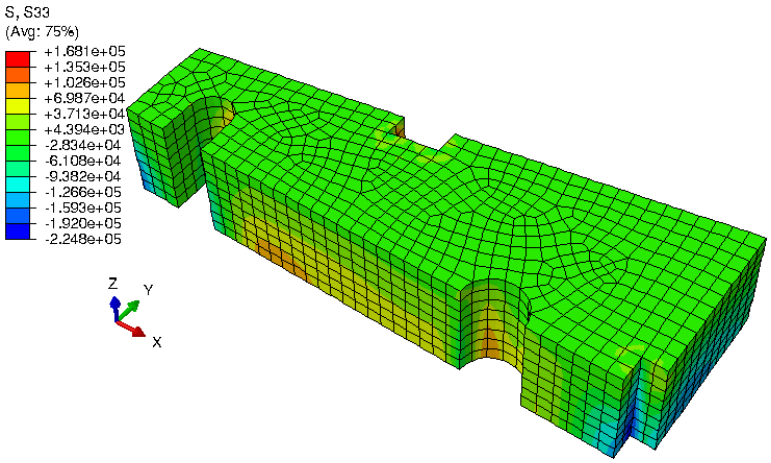

Figure 6.15: Axial stress distribution after 30 years.

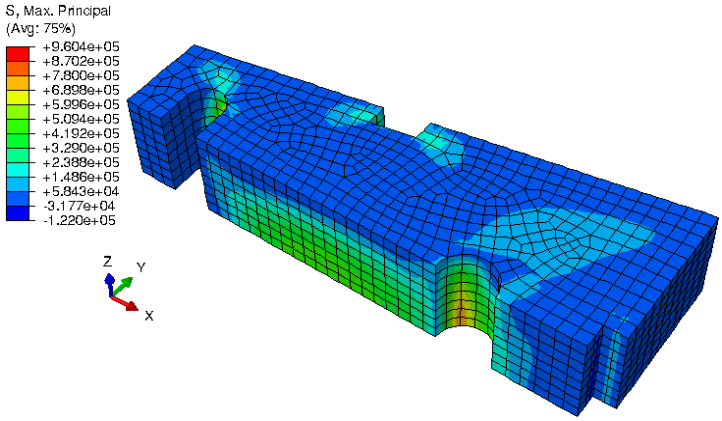

Figure 6.16: Maximum principal stress distribution after 30 years.

It was found that the radial stresses ranged from 0.73 MPa in tension to 0.13 MPa in compression. The hoop stresses ranged from 0.32 MPa in tension to 0.62 MPa in compression and the axial stresses ranged from 0.17 MPa in tension to 0.22 MPa in compression. The maximum principal stress ranged from 0.96 MPa in tension to 0.12 MPa in compression. The stresses were found to be high in the regions of sharp edges and corners, which indicated stress concentration. The variations of the radial, hoop and axial stresses with time at two different locations (node A and node B in Figure 6.17) on the brick are shown in Figures 6.18 to 6.20. For node A, the radial and hoop stresses were

found to be compressive throughout the operation of the reactor, while the axial stresses turned from compressive to tensile after about 15 years. For node B, on the other hand, the radial, hoop and axial stresses were tensile throughout the operation of the reactor.

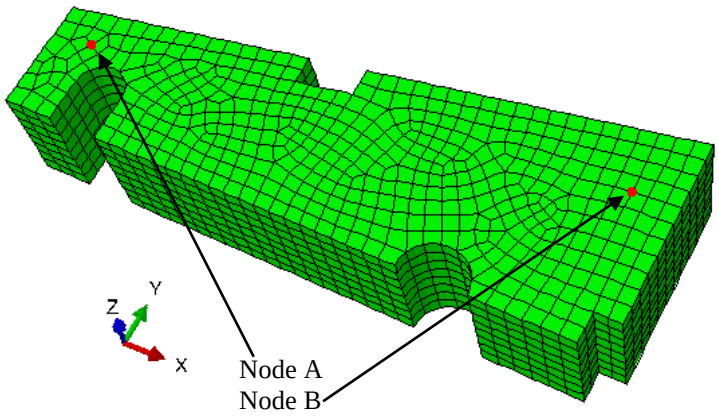

Figure 6.17: Locations of two points of interest (node A and node B).

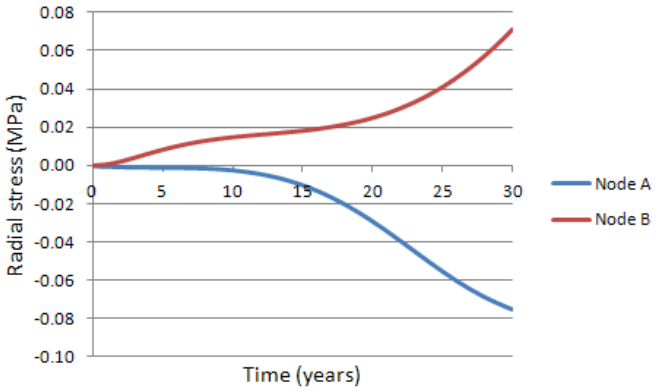

Figure 6.18: Variation of radial stress (S11) with time at two locations.

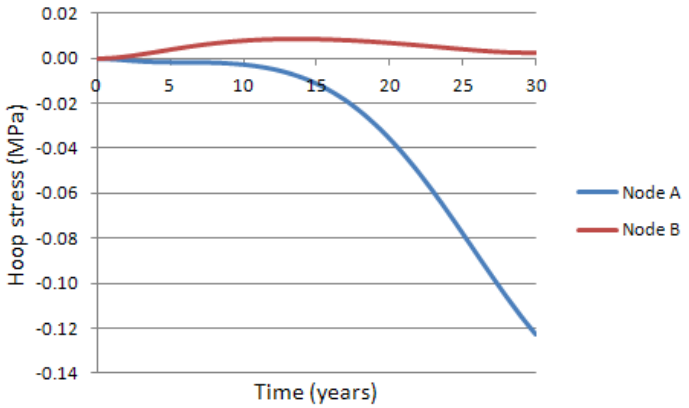

Figure 6.19: Variation of hoop stress (S22) with time at two locations.

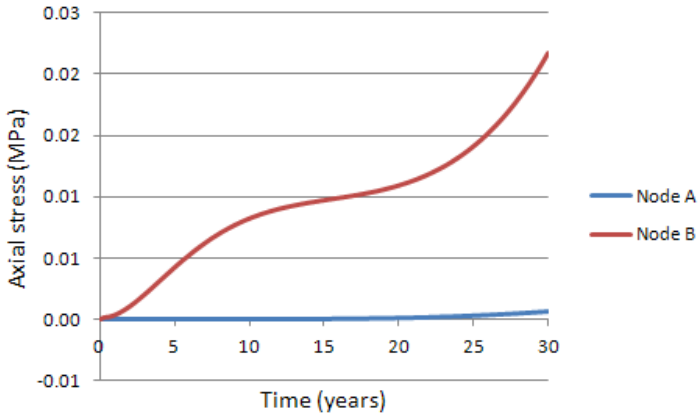

Figure 6.20: Variation of axial stress (S33) with time at two locations.

6.6 REFERENCES

1) http://www.prb.org/pdf12/2012-population-data-sheet_eng.pdf, last accessed on February 18, 2015.

2) http://www.ge-energy.com/nuclear, last accessed on February 18, 2015.

3) A Technology Roadmap for Generation IV Nuclear Energy Systems, US DOE Nuclear Energy Research Advisory Committee, Generation IV International Forum, GIF-002-00, 12/2002.

4) D. Chapin, S. Kiffer and J. Nestell, The Very High Temperature Reactor – A Technical Summary, MPR Associates Inc. Engineers, 06/2004.

5) A. C. Kadak, A Future for Nuclear Energy – Pebble Bed Reactors, MIT, 04/2004.

6) S. Yu, H. Li, C. Wang and Z. Zhang, Probability assessment of graphite brick in the HTR – 10, Nuclear Engineering and Design, 227, 133–142, 2004.

7) P. D. Smith, R.M. Sullivan, A.C. Lewis and H.J. Yu, The Accuracy of Finite-Element Models for the Stress Analysis of Multiple-Holed Moderator Blocks, International Conference on Structural Mechanics in Reactor Technology, GA-A16234, Paris, France, August 17-21, 1981.

8) P. D. Smith and D. Pelessone, Consistent Linearization Method for Finite-Element Analysis of Viscoelastic Materials, International Conference on Structural Mechanics in Reactor Technology, Chicago, USA, August 22-26, 1983.

9) T. Iyoku, M. Ishihara and H. Shirai, Development of Thermal/Irradiation Stress Analytical Code 'VIENUS' for HTTR Graphite Block, Journal of Nuclear Science and Technology, 28(10), 921-931, 1991

10) W. Weibull, A Statistical Theory of the Strength of Materials, Proc. Royal Swedish Academy of Eng. Sci., 151, 1-45, 1939.

11) W. Weibull, A Statistical Distrribution Function of Wide Applicability, Journal of Applied Mechanics, 18, 293-297, 1951.

12) H. Li, A. Fok and B. J. Marsden, An Analytical Study on the Irradiation – Induced Stresses in Nuclear Graphite Moderator Bricks, Journal of Nuclear Materials, 372, 164–170, 2008.

13) D. K. L. Tsang and B. J. Marsden, The Development of a Stress Analysis Code for Nuclear Graphite Components in Gas-Cooled Reactors, Journal of Nuclear Materials, 350, 208-220, 2006.

14) S. Mohanty, R. Jain, S. Majumdar, T. J. Tautges and M. Srinivasan, Coupled Field Structural Analysis of HTGR Fuel Brick Using Abaqus, Proceedings of ICAPP 2012, Paper # 12352, Chicago, USA, June 24-28, 2012

15) W. Haitao, S. Libin, W. Hongtao, S. Li and Z. Zhensheng, Research on Structural Integrity of Graphite Core Internals in HTR-PM, Proceedings of HTR 2010, Paper 251, Prague, Czech Republic, October 18-20, 2010.

16) S. Mohanty, M. Saurindranath and M. Srinivasan, Constitutive Modeling and Finite Element Procedure Development for Stress Analysis of Prismatic High Temperature Gas Cooled Reactor Graphite Core Components, Nuclear Engineering and Design, 260, 145-154, 2013.

17) H. Wang, X. Zhou, L. Sun, J. Dong and S. Yu, The effect of stress levels on the coefficient of thermal expansion of a fine – grained isotropic nuclear graphite, Nuclear Engineering and Design, 239, 484 – 489, 2009.

18) S. Ishiyama, T.D. Burchell, J.P. Striazak and M. Eto, The effect of high fluence neutron irradiation on the properties of a fine – grained isotropic nuclear graphite, Journal of Nuclear Materials, 230, 1 -7, 1996.

19) H. Matsuo, Effect of high temperature neutron irradiation on dimensional change and physical properties of nuclear graphite for HTGR. JAERI-M87-207.

20) I.G. Lebedev, O.G. Kochkarev and Y.S.Virgil'ev, Radiation – Induced change in the properties of isotropic structural graphite, Atomic energy, 93(1), 589 – 594, 2002.

21) T. Konishi, M. Eto and T. Oku, High temperature Young's Modulus of IG – 110 Graphite, JAERI-M86-192.

7. FAILURE PREDICTIONS OF THE VHTR COMPONENTS

When the stresses in the nuclear reactor graphite bricks reach the critical limit, i.e., strength of the material, cracks develop and start propagating. These cracks can have serious implications on the safe operation of the reactor: misalignment in the bricks caused by cracking can significantly check the ability of the bricks to serve as a structure and provide passageway for the coolant gases and control rods. Thus, it is important to estimate failure in these bricks. This chapter presents the application of the explicit crack modeling (ECM) approach for estimating failure in the VHTR graphite bricks. Two different geometries of the bricks were considered: cylindrical and prismatic. Both two-dimensional and three-dimensional models were employed for the purpose of understanding the advantages and limitations of either of them.

The methodology for estimating failure in the bricks included Monte Carlo analysis which involved simulation of crack initiation and propagation in specimens having varying fracture properties. Specimen models with different fracture properties were created to account for the randomness that exists in the fracture properties of graphite. The fracture properties distribution was based on the Weibull distribution. The results of the Monte Carlo analysis were used to evaluate the probability of failure of the brick as a function of time. The crack initiation and propagation in the brick was performed by employing the developed material subroutine UMAT in conjunction with the Extended Finite Element technique (XFEM). Prior to this work, a study was conducted to assess the viability of XFEM for modeling fracture in graphite. The details of the study are presented in Appendix B.

7.1 MONTE CARLO 2D FAILURE ANALYSIS OF A CYLINDRICAL GRAPHITE BRICK

A cylindrical graphite brick, which is a representative of an AGR (Advanced Gas-Cooled Reactor) brick, was modeled using Abaqus (see Figure 7.1). The brick was considered to be made of ATR-2E graphite and subjected to high temperature and irradiation conditions. Thirty different random values of strength (σ_f) and critical stress intensity factor (K_{IC}) were generated based on the Weibull distribution (Table 7.2) for performing the Monte Carlo analysis. The mean values of the strength and fracture toughness for generating their random values were obtained from the literature [1] and are shown in Table 7.1.

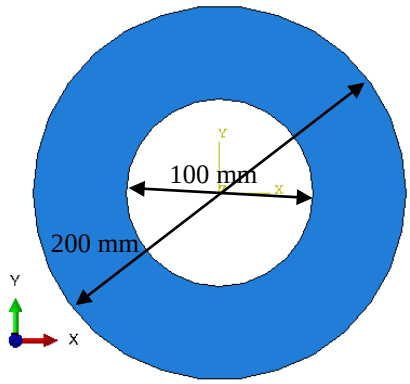

Figure 7.1: Cross-sectional view of a graphite brick (hollow cylinder).

Stresses and Fracture Prediction

The model was divided into XFEM and non-XFEM domains as shown in Figure 7.2. The XFEM domain is the region in which the nodes' degrees of freedom are enriched with special displacement functions to allow for the presence of discontinuities in the elements. The XFEM domain limits the occurrence of cracking within this region of the

brick. Therefore, it prevents multiple cracking in the brick model so as to be in accord with real-life observations.

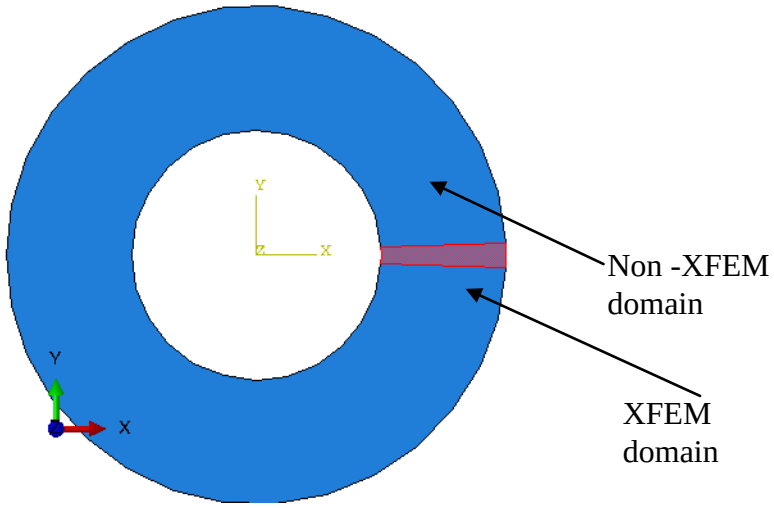

Figure 7.2: Brick model divided into enriched and non-enriched regions.

The model was meshed with 1248 CPS4 elements as shown in Figure 7.3. Figure 7.3 also shows the nodes constrained in the x- or y- directions. The temperature was assumed to decrease linearly from 550°C at the inner surface to 300°C at the outer surface (see Figure 7.4). The irradiation dose was assumed to decrease linearly from the inner surface to the outer surface of the brick and increase linearly with time as shown through Equation (7.1), where 'a' and 'b' are constants (9.6 and 58.7, respectively) and 'r' and 't' are radial distance (m) and time (years) respectively.

$$\text{dose} = (a - br)t \qquad (7.1)$$

The dose distribution in the graphite brick at the end of 30 years is shown in Figure 7.4.

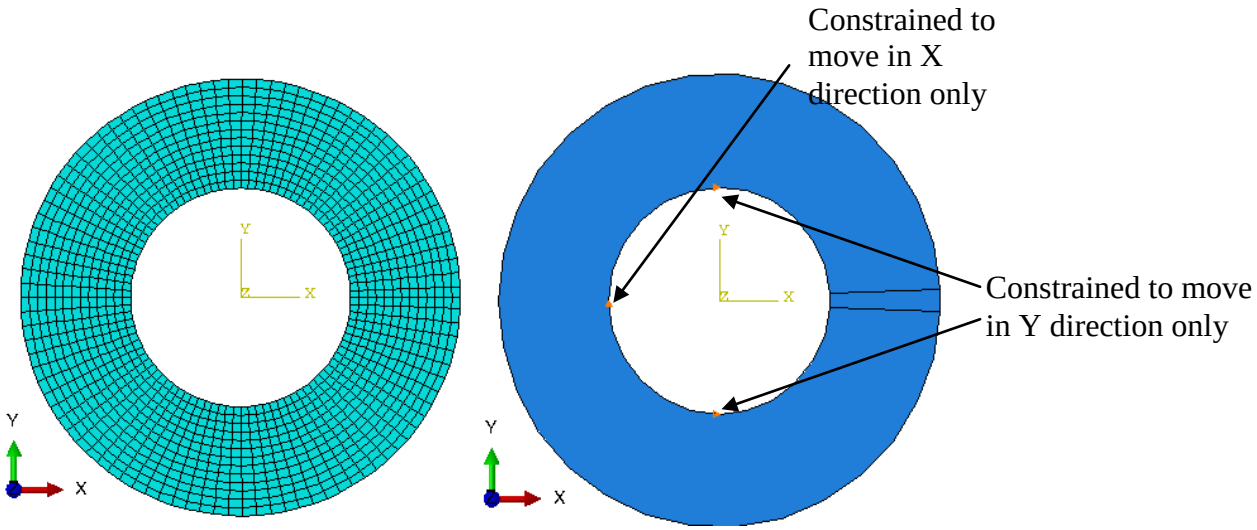

Figure 7.3: Meshed model of the graphite brick (left); boundary conditions on the brick (right).

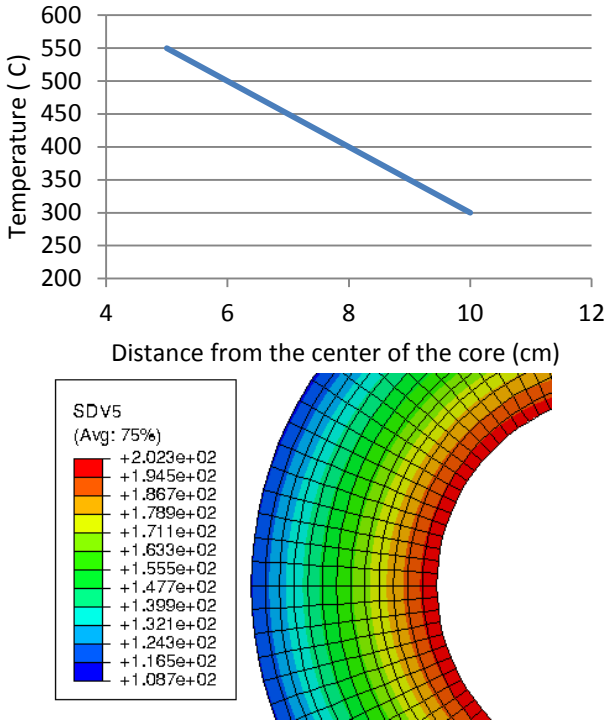

Figure 7.4: Variation of temperature with distance from brick center (top); variation of irradiation dose ($x10^{20}$n/cm^2) with radial distance at the end of 30 years (bottom).

The constitutive model for the brick included the irradiation creep strain, thermal strain, dimensional change strain, and elastic strain. The material data for ATR-2E were obtained from the work conducted by Haag [1]. These included the variations of the

dimensional change strain, coefficient of thermal expansion and Young's Modulus with dose and temperature. The creep modulus was assumed to be a constant.

To simulate fracture of the brick, the maximum principal stress criterion was selected as the damage initiation criterion. The incorporated damage evolution law was based on the fracture energy and the softening law was assumed to be linear. The mean values and the corresponding Weibull moduli of σ_f and K_{IC} used for generating the random values are given in Table 7.1. The critical fracture energy (G_{IC}) was calculated from the stress intensity factor K_{IC} using the Irwin relationship:

$$G = (1-\upsilon^2)\frac{K^2}{E} \qquad (7.2)$$

where υ and E are Poisson's ratio and Young's Modulus (for virgin graphite), respectively. The variation of fracture energy and strength with irradiation was not considered in the 2D analysis.

Table 7.1: The mean value and Weibull Modulus for strength and critical stress intensity factor.

	Mean value	**Weibull modulus**
Strength (σ_f)	12. 5 MPa	9
Critical stress intensity factor (K_{IC})	1.0 MPa√m	35

Fracture of the brick for the thirty cases was simulated. Failure of a brick was defined as the appearance of a crack in the FE model and the failure probability of the graphite brick was evaluated as a function of time using Equation 7.3 below.

$$\text{Failure probability (time t)} = \frac{\text{Number of specimens failed uptil time t}}{\text{Total number of specimens}} \qquad (7.3)$$

Results and Discussion

The finite element model was run in Abaqus for each of the thirty sets of fracture energy and strength. Figure 7.5 shows the maximum principal stress distribution in the graphite brick at the end of 5, 10, 15, 20, 25 and 30 years for specimen 1 (σ_f = 14.3 MPa, G_{IC} = 92.6 J/m^2).

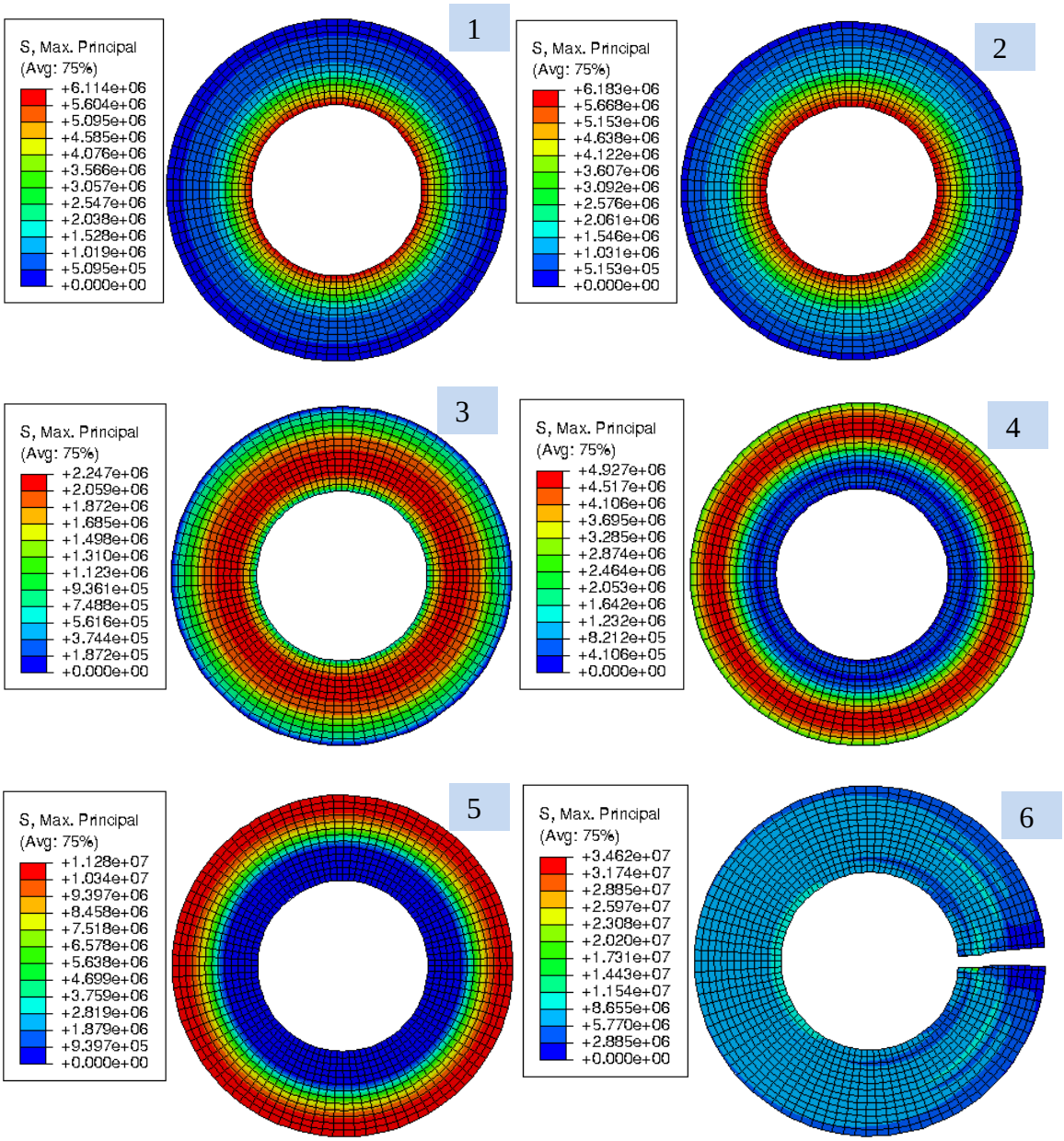

Figure 7.5: Distribution of the maximum principal stress at the end of 5, 10, 15, 20, 25 and 30 years shown in pictures numbered 1, 2, 3, 4, 5 and 6 respectively for case 1 (σ_f = 14.3 MPa, G_{IC} = 92.6 J/m^2).

Figure 7.6 shows the variation of hoop stress at the inner and outer surfaces of the brick with time for the same specimen. It can be seen that the sudden temperature rise at the start of the reactor operation caused development of thermal stresses in the graphite brick. The thermal stresses were compressive at the inner surface and tensile at the outer surface. Due to irradiation creep and irradiation effect the thermal stresses were relieved and at around 2 years the brick was under negligible stress. Then, continued irradiation resulted in tensile stresses in the inner region and compressive stresses in the outer region of the brick. The turn-around of stresses at the inner and outer surfaces took place at the 8^{th} and 10^{th} years, respectively, and at these time points the magnitude of the stresses started decreasing. At the 14^{th} year, the stresses at the inner surface changed from tensile to compressive; and at the 19^{th} year the stresses at the outer surface changed from compressive to tensile and continued to increase.

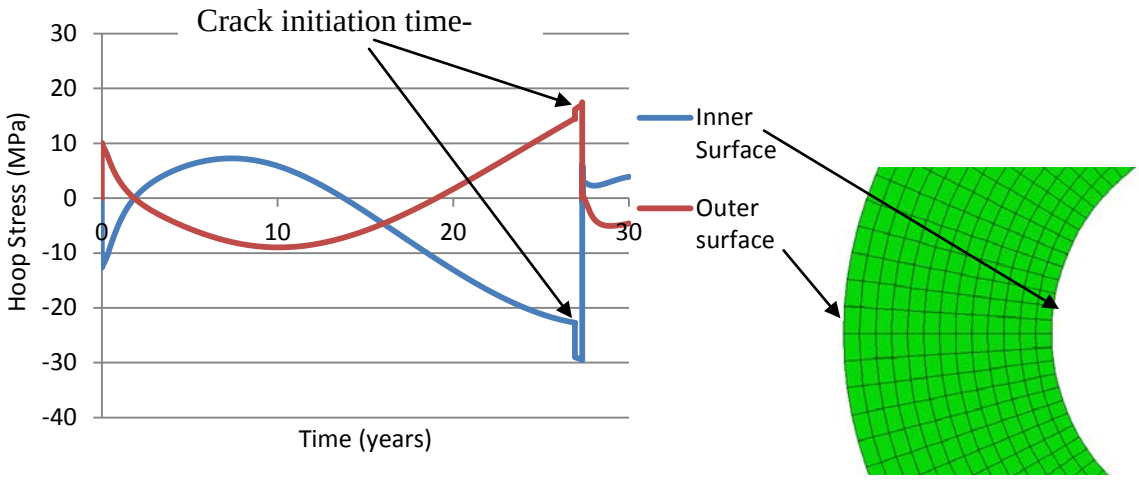

Figure 7.6: Variation of hoop stress with time at the inner and outer surfaces of the brick for specimen 1 (σ_f = 14.3 MPa, G_{IC} = 92.6 J/m^2).

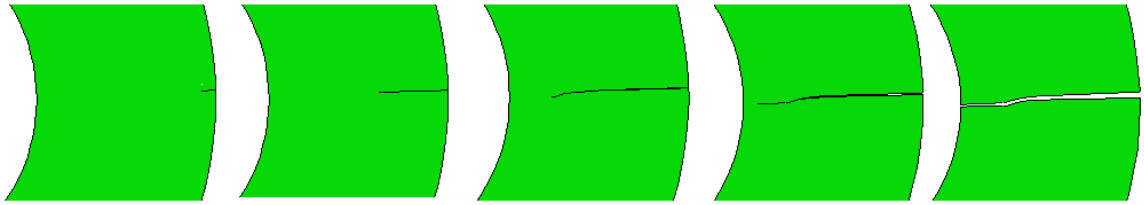

Figure 7.7: Crack propagation with time through the thickness of the cylindrical graphite brick model.

Figure 7.7 shows the crack propagation through the thickness of the cylindrical graphite brick. For each specimen, the times at which crack initiated in the brick, penetrated through half of the thickness and penetrated through all the thickness of the brick were obtained and listed in Table 7.2. Since the crack initiation time was found to be very close to the time at which the crack penetrated through half of the thickness of the brick, the failure time was defined as equal to the crack initiation time. It was found that cracking developed in 2 specimens (specimens 8 and 26) within the first year. Such unusually early failure of these specimens can be attributed to their very low strengths (8.98 and 8.77 MPa), which were lowest within the group. The thermal stresses developed in the graphite bricks during the start of the reactor were about 10 MPa and were greater than the strength of these two specimens. Therefore, it was the thermal stresses that caused the failure of these two graphite bricks.

Table 7.2: The predicted times at which a crack initiated, penetrated through half of the thickness and penetrated through all the thickness in the brick.

Specimen number	**G (J/m^2)**	**Strength (Pa)**	**Crack initiation time (years)**	**Half radial distance penetration time (years)**	**Full radial distance penetration time (years)**
1	92.585	14342646.79	26.92	26.92	27.34
2	110.1351	12852079.07	26.12	26.13	26.39
3	92.1204	14161890.22	26.82	26.83	27.32
4	101.0609	13732899.95	26.62	26.63	26.98
5	110.8948	10419269.28	24.72	24.72	
6	107.1619	11172630.51	25.12	25.13	25.36

7	102.6631	12693836.63	26.02	26.03	26.45
8	88.3286	8981793.07	1		
9	87.3517	14305797.38	26.92	26.92	26.92
10	109.4413	12233736.59	25.72	25.82	26.04
11	86.4567	12448451.15	25.82	25.83	26.16
12	88.3697	10795081.39	24.92	24.93	25.18
13	103.7269	10612426.46	24.82	24.83	25.03
14	96.9803	13239377.72	26.32	26.33	26.6
15	109.7879	12040452.93	25.62	25.63	25.88
16	104.7849	12207989.68	25.72	25.73	26.04
17	91.9684	11400006.43	25.32	25.33	25.55
18	97.2272	11100184.66	25.12	25.13	25.34
19	88.0822	10857574.58	25.02	25.03	25.26
20	100.5854	12855686.94	26.12	26.13	26.37
21	113.1924	11245732.42	25.22	25.23	25.4
22	95.2821	11360276.52	25.22	25.23	25.53
23	90.6435	13357064.47	26.42	26.43	26.76
24	100.0969	13594588.63	26.52	26.53	26.86
25	98.2031	12007471.63	25.62	25.63	25.84
26	98.5844	8767569.468	1		
27	105.2695	12604331.18	25.92	26.02	26.25
28	100.5909	11662426.52	25.43	25.42	25.63
29	109.1556	13073066.26	26.22	26.32	26.59
30	99.4847	10876902.64	25.02	25.03	25.19

Finally, the variation of failure probability of the ATR-2E graphite brick as a function of time was obtained according to Equation (7.3), as shown in Figure 7.8. It can be seen that most of the brick specimens failed during the time range of 24-27 years. Except specimens 8 and 26, whose failure were caused by thermal stresses, in all the specimens cracking occurred at the outer surface of the brick and propagated towards the inner surface. Crack initiation at the outer surface can be explained from Figure 7.6, which shows that the maximum principal stress occurred at the outer surface of the brick, making it most susceptible to fracture. When the maximum principal stress reached the critical limit, a crack developed. It can be noted from Table 7.2 that the brick specimens with higher strengths had longer lives. The failure probability vs. time plot shown in Figure 7.8 shows that the failure probability is low (0.067) up till 24 years and rises steeply thereafter.

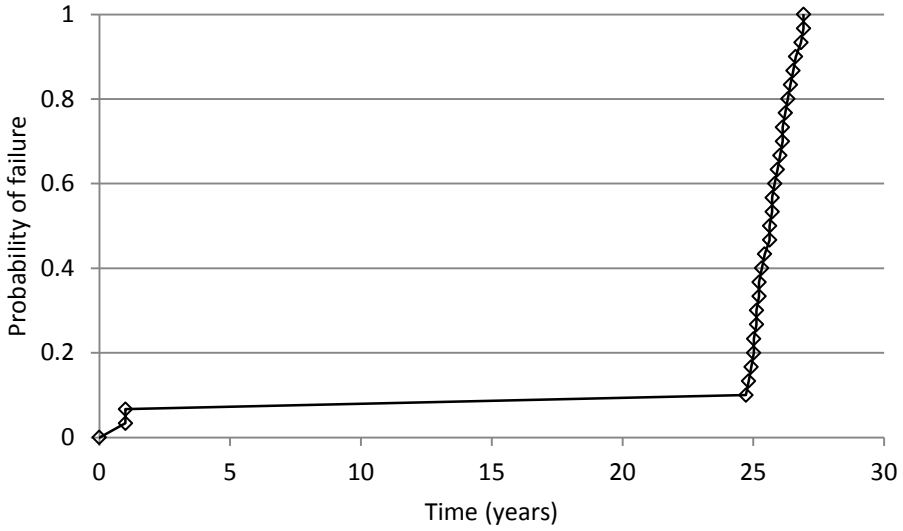

Figure 7.8: Failure probability of ATR-2E graphite brick vs. time.

Summary

Thirty different random values of strength and fracture energy based on the Weibull distribution were generated for ATR-2E graphite. Due to the unavailability of dose and temperature distribution data, assumptions were made regarding their spatial distributions. For each of the thirty cases, stresses and cracking were simulated for the cylindrical graphite brick. For 28 cases, cracking initiated at the outer surface of the brick and propagated rapidly through the thickness towards the inner surface. Most of the bricks failed in the time range of 24-27 years. However, in two cases, the brick failed within the first year due to thermal stresses. The failure probability of ATR-2E graphite bricks was found to be low up till 24 years and rose steeply thereafter.

7.2 MONTE CARLO 3D FAILURE ANALYSIS OF A CYLINDRICAL GRAPHITE BRICK

A cylindrical ATR-2E graphite brick was modeled in 3D using the commercial finite element software Abaqus (see Figure 7.9). The XFEM technique was employed in conjunction with UMAT to simulate crack initiation and propagation which would happen when the internal stresses reached the critical limit.

Monte Carlo failure analysis of the brick was performed in a similar manner as described previously for 2D brick models and probability of failure was evaluated from the analysis results.

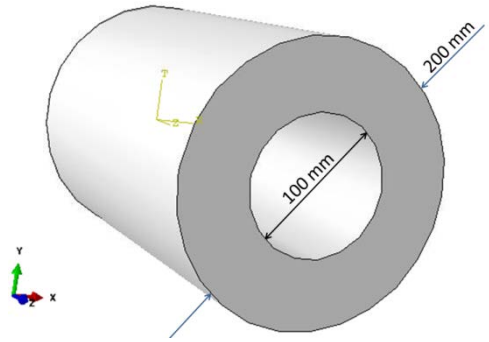

Figure 7.9: Cylindrical graphite brick model.

FE simulation

The brick model was divided into XFEM and non-XFEM domains as shown in Figure 7.10.

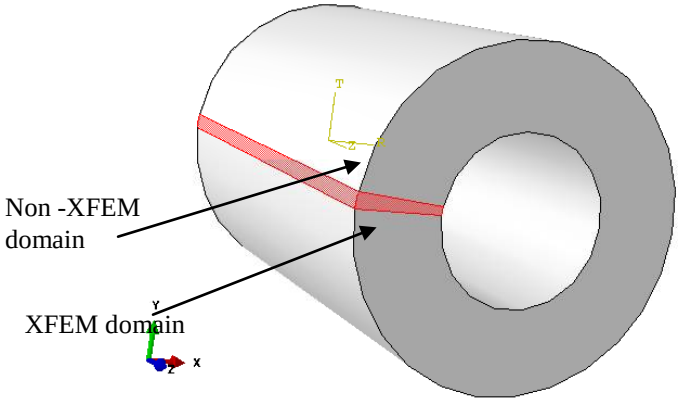

Figure 7.10: XFEM and non-XFEM domains of brick model.

The brick was meshed with 11520 C3D8 (continuum 3D 8-node linear isoparametric) elements as shown in Figure 7.11. Figure 7.11 also shows the boundary conditions on the model.

The temperature and irradiation dose distribution and variation were prescribed in the same way as for 2D cylinder model described earlier in section 7.1. The dose distribution in the graphite brick at the end of 20 years of operation is shown in Figure 7.12.

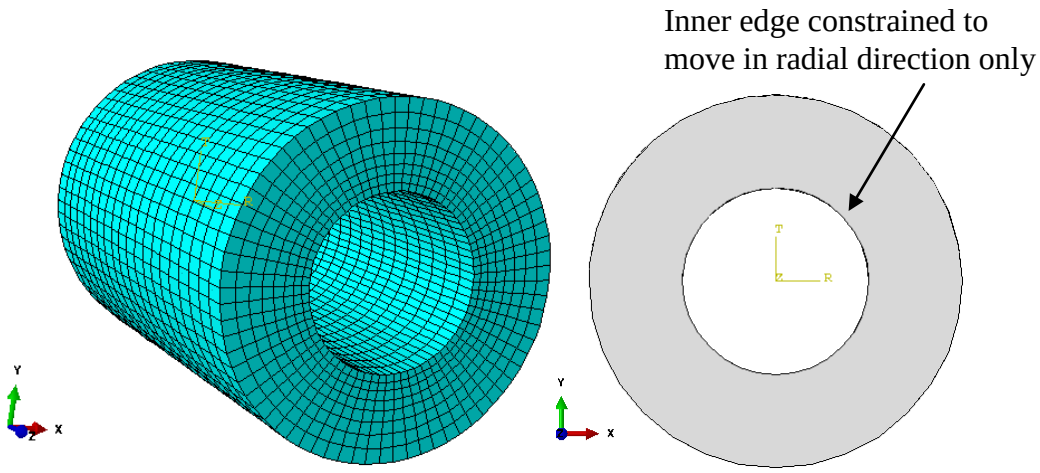

Figure 7.11: Mesh of 3D FE model (left); boundary conditions on the brick (right).

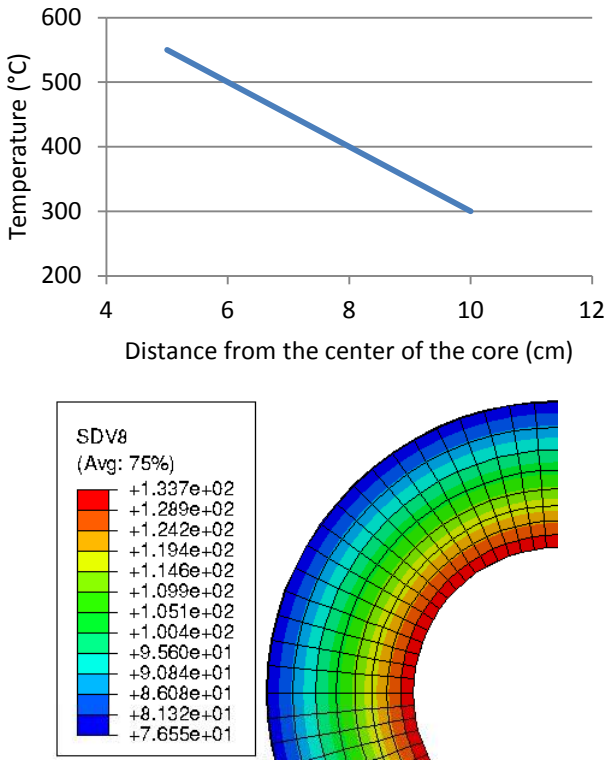

Figure 7.12: Variation of temperature with radial distance from brick center (left); variation of irradiation dose ($x10^{20}n/cm^2$) with radial distance at the end of 20 years (right).

The brick was considered to be made of ATR-2E graphite. The constitutive model for the brick, variation of various strains and physical properties with irradiation dose and temperature, the procedure of Monte Carlo analysis were set up in the same way as described earlier for 2D analysis in section 7.1.

The variation of strength with irradiation dose was incorporated in the 3D analysis. Data about the dependence of strength on irradiation dose for ATR-2E graphite was not available. Therefore, a trend similar to that found for IG-110 graphite [3] was assumed, as shown in Figure 7.13. An Abaqus based user-subroutine, USDFLD, was coded for implementing the irradiation-dependence of strength in the finite element analysis. The variation of fracture toughness with irradiation was not considered.

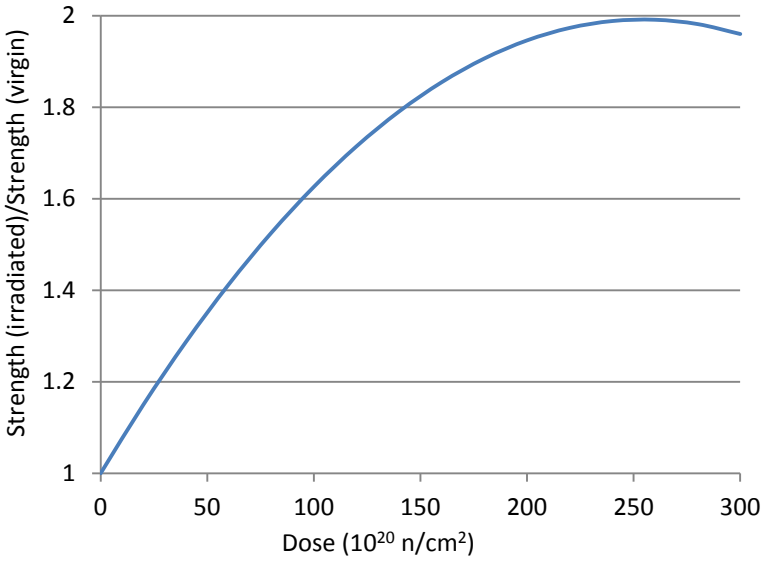

Figure 7.13: Variation of strength with irradiation dose [3].

Results and Discussion

The finite element model was run in Abaqus for each of the thirty sets of fracture energy and strength. Figure 7.14 shows the maximum principal stress distribution in the graphite brick at the end of 5, 10, 15, 20, 25 and 30 years for Case 1 (σ_f = 13.9 MPa, G_{IC} = 102.5 J/m^2).

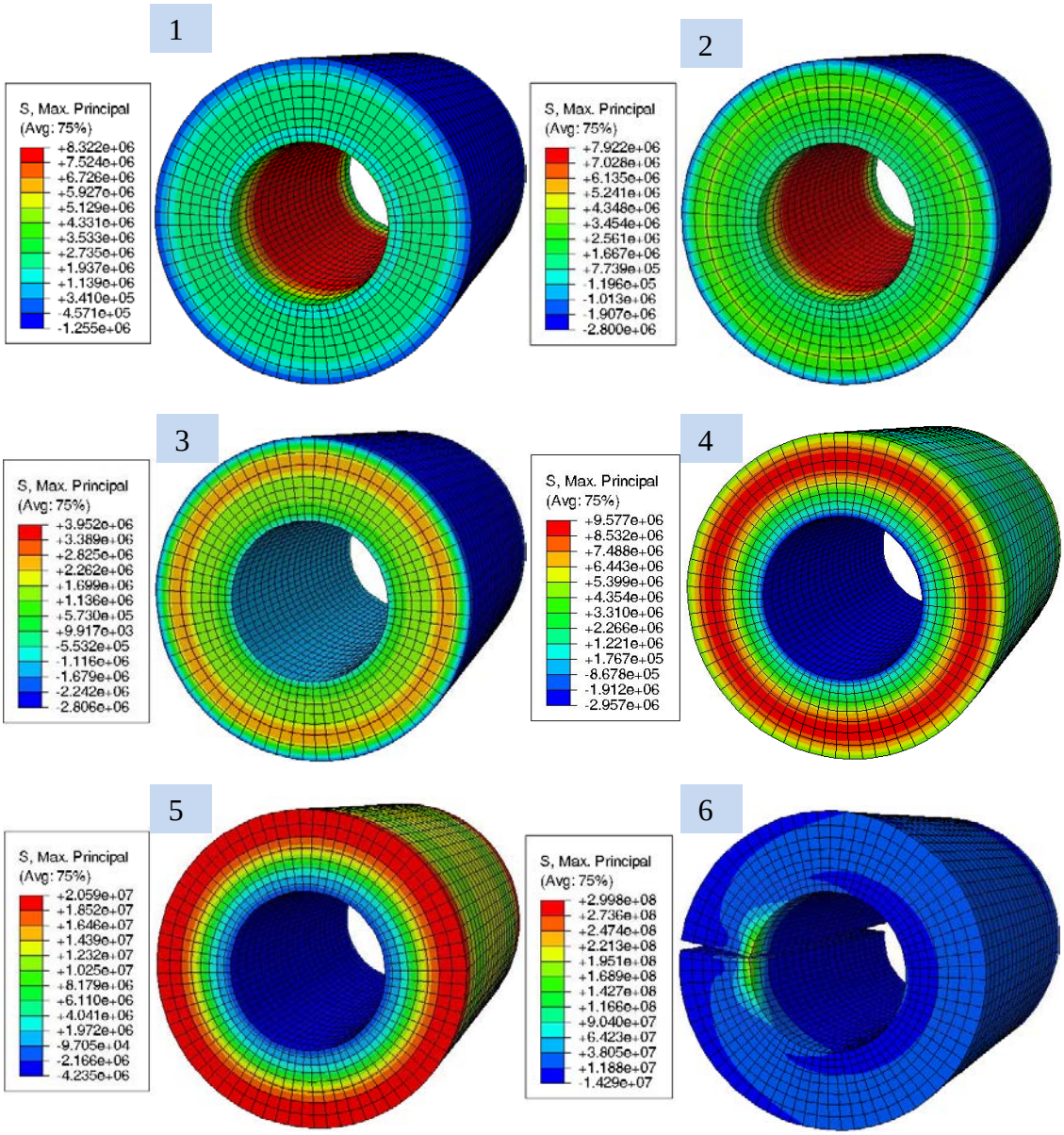

Figure 7.14: Distribution of maximum principal stress at the end of 5, 10, 15, 20, 25 and 30 years, shown in pictures numbered 1, 2, 3, 4, 5 and 6, respectively for Case 1 (σ_f = 13.9 MPa, G_{IC} = 102.5 J/m^2).

Figure 7.15 shows the variation of the hoop stress with time at the inner and outer surfaces of the brick for Case 1. It can be seen that the sudden temperature rise at the start of reactor operation caused the development of thermal stresses in the graphite brick. The thermal stresses were compressive at the inner surface and tensile at the outer surface.

Due to irradiation creep and irradiation effects, the thermal stresses were released and at around 2 years the brick was under negligible stress. Then, continued irradiation resulted in tensile stresses in the inner region and compressive stresses in the outer region of the brick. The turn-around of stresses at the inner and outer surfaces took place at the 6^{th} and 9^{th} years, respectively, and at these time points the magnitude of the stresses started decreasing. At the 12^{th} year, the stresses at the inner surface changed from being tensile to compressive; and at the 17^{th} year the stresses at the outer surface changed from being compressive to tensile and continued to increase until failure.

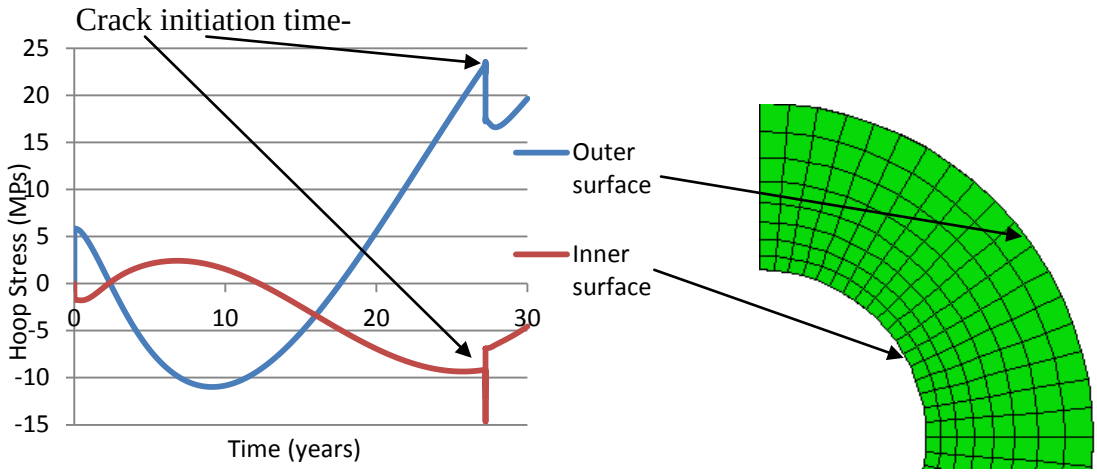

Figure 7.15: Variation of hoop stress with time at the inner and outer surfaces of the brick for Specimen 1 (σ_f = 13.9 MPa, G_{IC} = 102.5 J/m^2).

Figure 7.16 shows the crack propagation through the thickness of the graphite brick. Since the crack initiation time was found to be very close to the time at which the crack penetrated through more than half of the thickness of the brick, the failure time was taken to be equal to the crack initiation time.

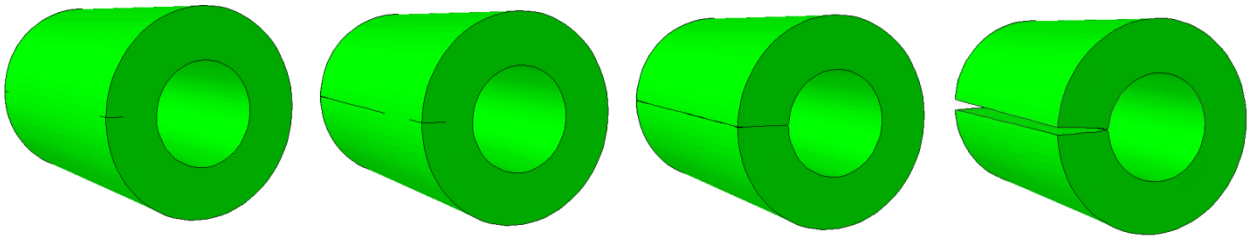

Figure 7.16: Crack propagation with time through a graphite brick model

Table 7.3 lists the crack initiation time for all the specimens. It was found that the specimen 28 shortest crack initiation time, which had the lowest strength in the group. The crack in this specimen initiated at the 7^{th} year at the inner surface. After crack initiation, the stresses at the inner surface decreased and turned compressive later on. Thus, the crack was arrested within the small region where it appeared and did not propagate within the first 30 years. For all the other specimens, cracking occurred at the outer surface of the brick and propagated towards the inner surface. Crack initiation at the outer surface can be explained from Figure 7.15, which shows that the maximum principal stress occurs at the outer surface of the brick, making it most susceptible to fracture. It can be noted from Table 7.3 that the brick specimens with higher strengths had longer lives.

Table 7.3: Fracture toughness, strength and the corresponding crack initiation time for all specimens.

Specimen number	**G (J/m^2)**	**Strength (Pa)**	**Crack initiation time (years)**
1	102.47	13887552.87	27.2
2	112.05	14080373.8	27.3
3	107.68	11881528.27	25.7
4	103.8	10713307.57	24.8
5	97.3	9276372.197	23.8
6	91.779	13531179.51	26.9
7	106.93	11729788.11	25.6
8	114.44	12118053.11	25.8
9	114.19	14748369.47	27.9
10	112.01	12616799.76	26.2
11	99.588	13359223.65	26.8
12	112.07	10618339.73	24.8
13	100.55	12716674.09	26.3
14	112.27	11890412.62	25.7
15	94.808	13341876.42	26.8
16	110.38	11592666.2	25.5
17	113.17	12908567.45	26.4
18	112.13	11364914.11	25.3
19	105.61	11200021.4	25.2
20	108.26	10894350.74	25
21	110.35	12189317.59	25.9
22	99.964	13826740.88	27.1
23	106.21	13050776.05	26.5
24	106.89	9573306.627	24
25	95.701	13409348.67	26.8
26	111.5	10402105.93	24.6
27	102.31	11851814	25.7
28	102.41	6743920.79	6.3
29	109.86	13869423.34	27.2
30	106.55	12218937.04	25.9

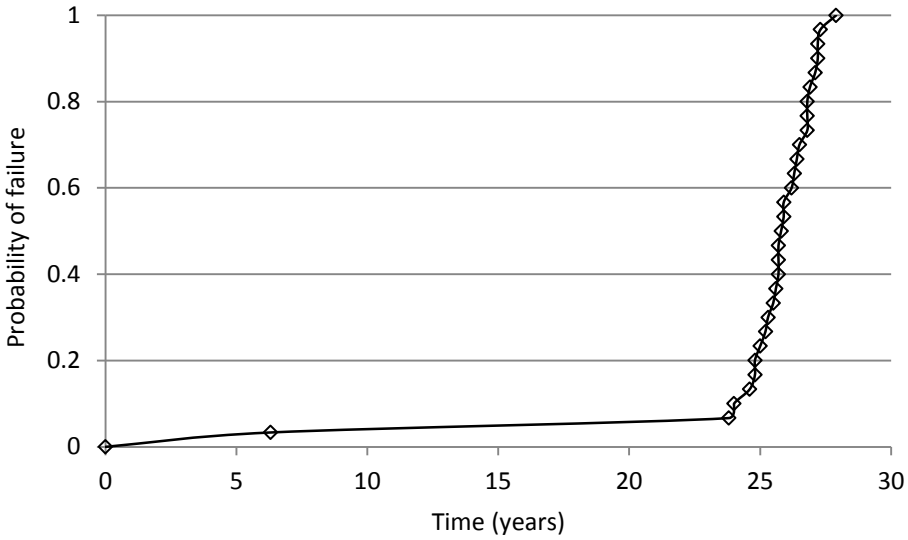

Figure 7.17: Failure probability of ATR-2E graphite brick vs. time.

Finally, the failure probability of the ATR-2E graphite brick as a function of time was obtained according to Equation (7.3), as shown in Figure 7.17. It can be seen that most of the brick specimens failed during the period of 24-27 years and the failure probability was low (0.067) up till 23.8 years and rose steeply thereafter.

These results are in good agreement with the results of 2D failure analysis presented earlier in section 6.1.1 for the same brick. For 2D failure analysis a sudden increment in the temperature was considered which resulted in high thermal stresses leading to failure of two bricks within the first year. However, for the analysis presented herein the rise in the temperature happened over the period of one day. It lead in smaller thermal stresses and consequently no failure occurred due to thermal stresses.

Summary

Thirty different sets of values of strength and critical fracture energy for ATR-2E graphite were randomly generated based on the Weibull distribution. Linear spatial distributions of dose and temperature in the brick were assumed and the dependence of

strength on irradiation dose was considered. For each of the thirty cases, stresses and cracking were simulated for the cylindrical graphite brick. For 29 cases, cracking initiated at the outer surface of the brick and propagated rapidly through the thickness towards the inner surface. Most of the bricks failed between 24 and 27 years. The failure probability of ATR-2E graphite bricks was found to be low up till 23.8 years and rose steeply thereafter. The results for 3D failure analysis were found to be in good agreement with the results for 2D failure analysis.

7.3 MONTE CARLO 2D FAILURE ANALYSIS OF A PRISMATIC REFLECTOR BRICK

A prismatic reflector graphite brick was modeled using the commercial finite element software Abaqus. Figure 7.18 shows the location of the brick in the prismatic reactor core and its dimensional details. Figure 7.19 shows the computer model of the reflector brick used for numerical analysis. Brick was considered to be made of ATR-2E graphite and subjected to high temperature and irradiation conditions. The irradiation data were obtained from reference [2]. Thirty different random values of strength (σ_f) and critical stress intensity factor (K_{IC}) were generated based on the Weibull distribution (Table 7.4) for performing the Monte Carlo analysis. The mean values of the strength and fracture toughness for generating their random values were obtained from the literature [1] and are shown in Table 7.1. Fracture of the brick was simulated for the thirty cases. The failure of a brick was defined as an appearance of crack in the brick and the failure probability of the graphite brick was evaluated as a function of time using Equation 7.3.

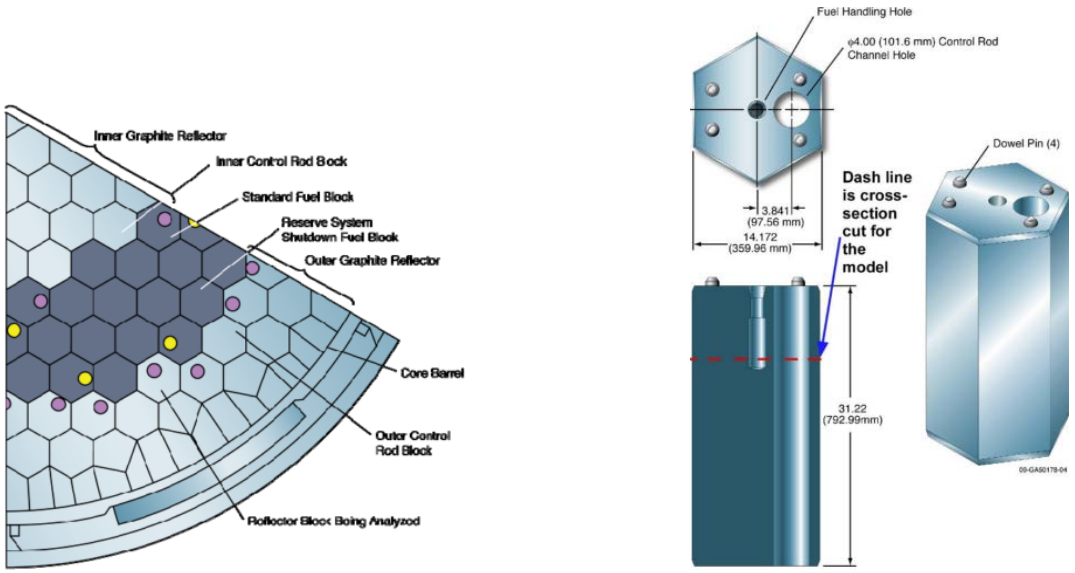

Figure 7.18: Location and dimensional details of prismatic reflector brick considered for failure analysis (source: [2]).

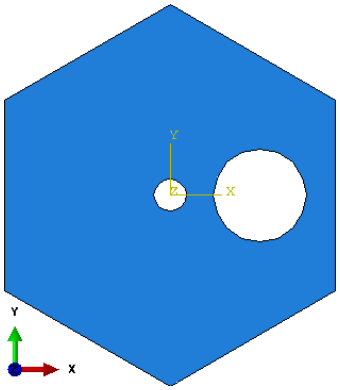

Figure 7.19: Prismatic reactor core brick model.

Stress and Failure Predictions

The model was divided into XFEM and non-XFEM domains as shown in Figure 7.20.

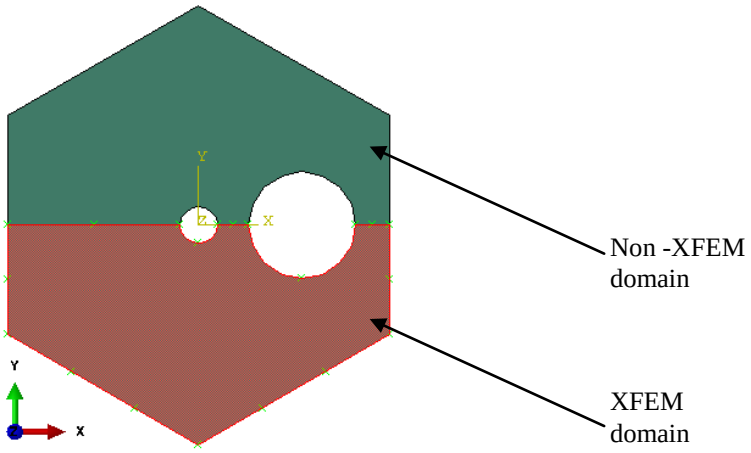

Figure 7.20: Brick model divided into enriched and non-enriched regions.

The model was meshed with 3625 CPS4 elements with 3756 nodes as shown in Figure 7.21. Figure 7.22 also shows the nodes constrained in the x or y directions. The irradiation dose distribution was based on the operating conditions for a reflector brick in the Ft. St. Vrain reactor as presented in [2]. Due to unavailability of temperature distribution data for the prismatic reflector brick, a temperature distribution based on simple assumptions was used for the numerical analysis (see Figure 7.23).

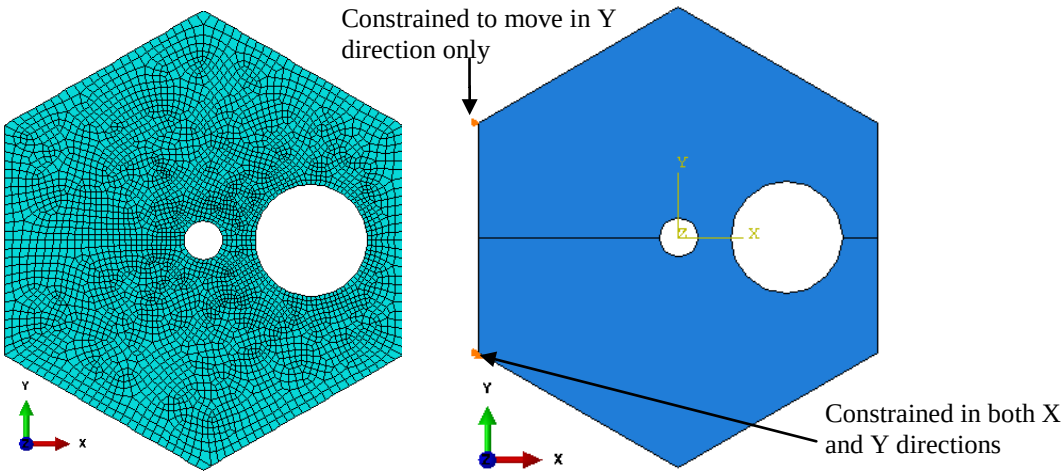

Figure 7.21: Meshed model of the prismatic brick (left); boundary conditions on the brick (right).

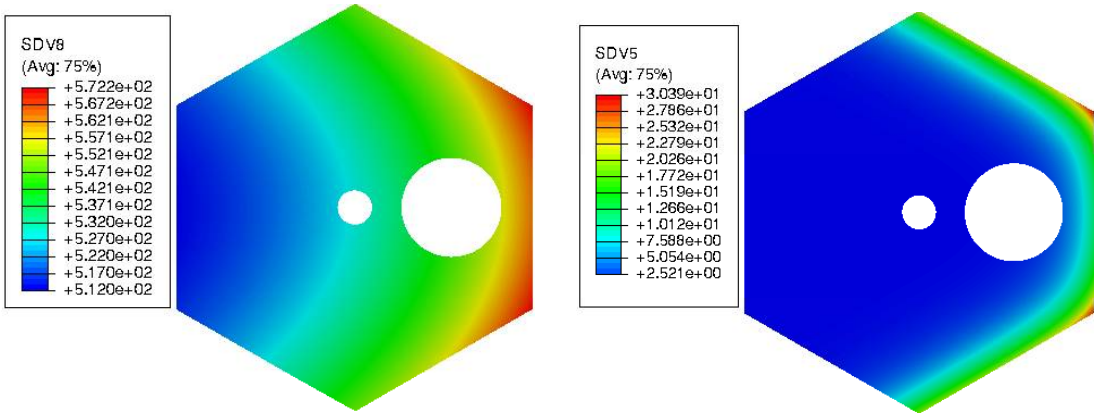

Figure 7.22: Temperature distribution (left) and irradiation dose distribution ($x10^{20}n/cm^2$) (right) in the prismatic reactor core brick at the end of 6 years.

Results and Discussion

The finite element model was run in Abaqus for each of the thirty sets of fracture energy and strength. Figure 7.23 shows the maximum principal stress distribution in the graphite brick at the end of 2, 5, 8, 11, 11.6 and 17 years for specimen 1 (σ_f = 15.1 MPa, G_{IC} = 110.3 J/m^2).

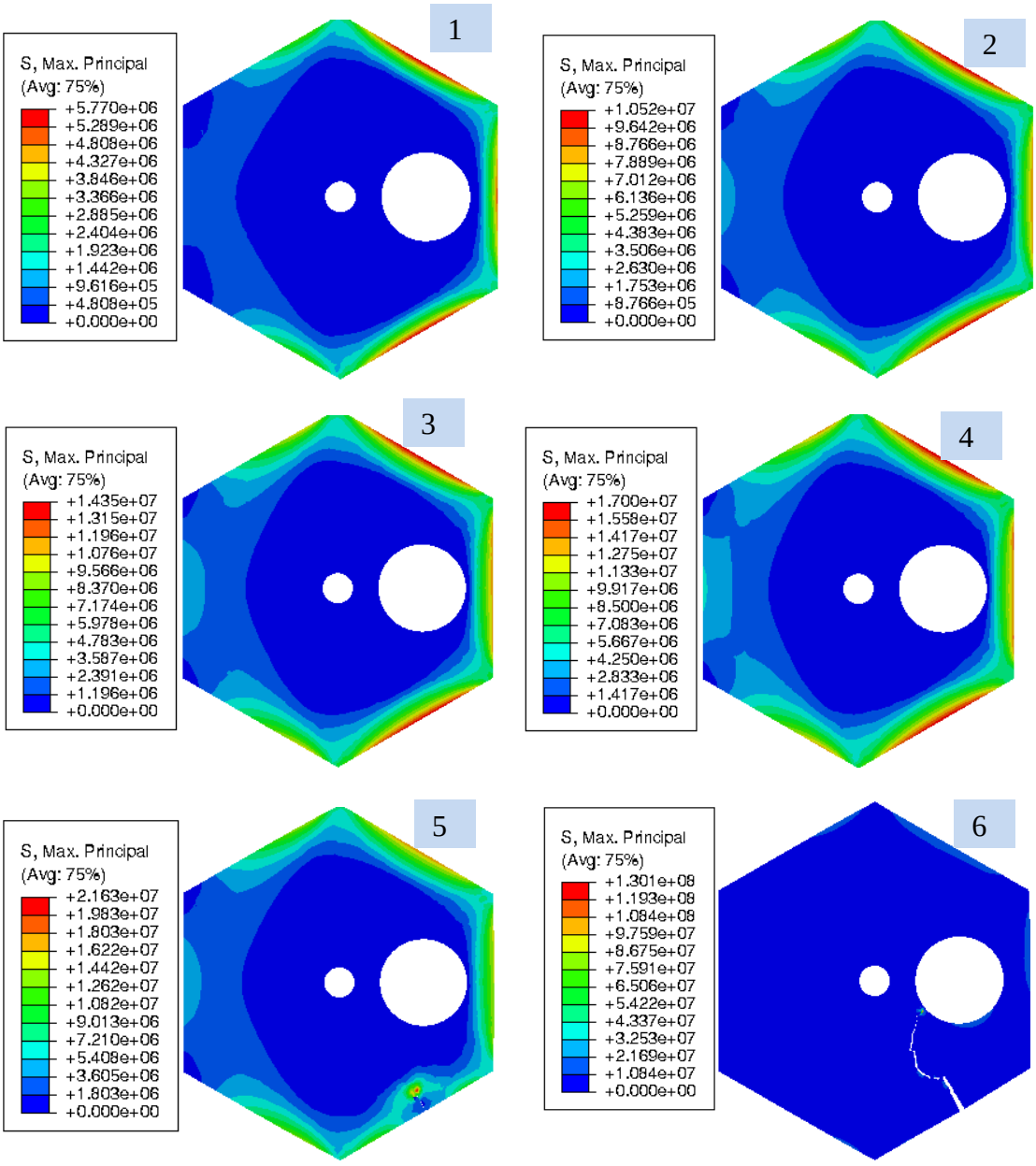

Figure 7.23: Distribution of maximum principal stress with ATR-2E graphite at the end of 2, 5, 8, 11, 11.6 and 17 years shown in pictures numbered 1, 2, 3, 4, 5 and 6 respectively for case 1 (σ_f = 15.1 MPa, G_{IC} = 110.3 J/m^2).

Figure 7.24 shows the variation of the maximum principal stress with time at two different locations in the reflector brick for a specimen. With an increase in irradiation, the maximum principal stress increased until crack initiated. Due to cracking in the brick, stresses were relieved which resulted in decrease in the stresses at the two locations.

Node B was nearer to the crack location and experienced greater stress relaxation. So, the decrease in stress was greater at node B. The crack was arrested and the stresses again increased in magnitude. But as the crack began to propagate again, stresses again decreased in magnitude. The life-time of this particular specimen was found to be 11.6 years.

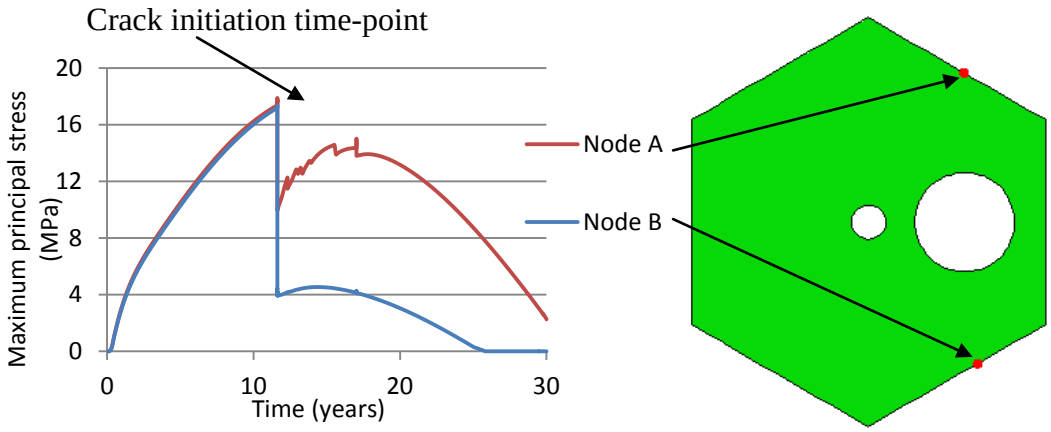

Figure 7.24: Variation of maximum principal stress with time at the inner and outer surfaces of the brick for specimen 1 (σ_f = 15.1 MPa, G_{IC} = 110.3 J/m^2).

Figure 7.25 shows the crack propagation through a reflector brick model. For each specimen the time at which crack initiated was obtained and listed in Table 7.4. It was found that cracks initiated at the right lower edge (see Figure 7.25) of the specimen and propagated towards the control rod channel. Initiation of cracks from this particular location could be attributed to the high dose gradient between the control rod channel and the brick edge which led to the development of high stresses in that location. It indicates that the outer surface of the reflector brick, which is in contact with a fuel brick, is more susceptible to failure than the inner free surfaces of the control rod channel and fuel handling hole. It was also observed that the crack propagation was quite fast initially and most of the path was traversed by the crack shortly after initiation. It indicates that the

prismatic reactor core reflector brick made of ATR-2E graphite will fail as soon as a crack appears in it.

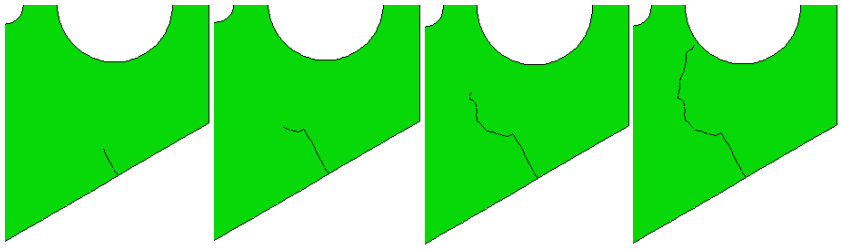

Figure 7.25: Crack propagation with time through the thickness of a graphite brick model.

Table 7.4: The predicted times at which crack initiates in the brick.

Specimen number	**G (J/m^2)**	**Strength (MPa)**	**Crack initiation time (years)**
1	96.52	13.67	9.82
2	92.59	8.71	5.02
3	110.14	15.07	11.6
4	92.12	10.74	6.82
5	101.06	10.46	6.52
6	110.89	10.05	6.22
7	107.16	13.82	10.0
8	102.66	12.38	8.42
9	88.33	12.92	8.92
10	87.35	10.58	6.62
11	109.44	12.26	8.22
12	86.46	9.61	5.82
13	88.37	13.26	9.32
14	103.73	12.91	8.92
15	96.98	13.45	9.52
16	109.79	13.50	9.62
17	104.78	10.05	6.52
18	91.97	11.69	7.72
19	97.23	11.81	7.82
20	88.08	13.45	9.52
21	100.59	10.19	6.32
22	113.19	11.51	7.52
23	95.28	12.56	8.62
24	90.64	11.95	7.92
25	100.10	12.37	8.42
26	98.20	13.89	10.0
27	98.58	13.00	9.02
28	105.27	13.57	9.72
29	100.59	13.25	9.32
30	109.16	13.00	9.02

Failure of the reflector brick specimens was governed mainly by their strength: bricks with higher strength had longer lifetime while bricks with lower strength failed in shorter time. The brick specimen with the lowest strength of 8.7 MPa had the shortest lifetime of 5 years while the brick with the greatest strength of 15.1 MPa had the longest lifetime of 11.6 years. Finally, the variation of failure probability of the ATR-2E graphite brick as a function of time was obtained according to Equation 7.3, as shown in Figure 7.26. There was no failure observed before 5 years, so the failure probability is zero during this initial period. Most reflector brick specimens failed during the time range of 6-10 years, therefore the failure probability rose steeply within this time range. After about 10 years the failure probability was almost equal to 1.

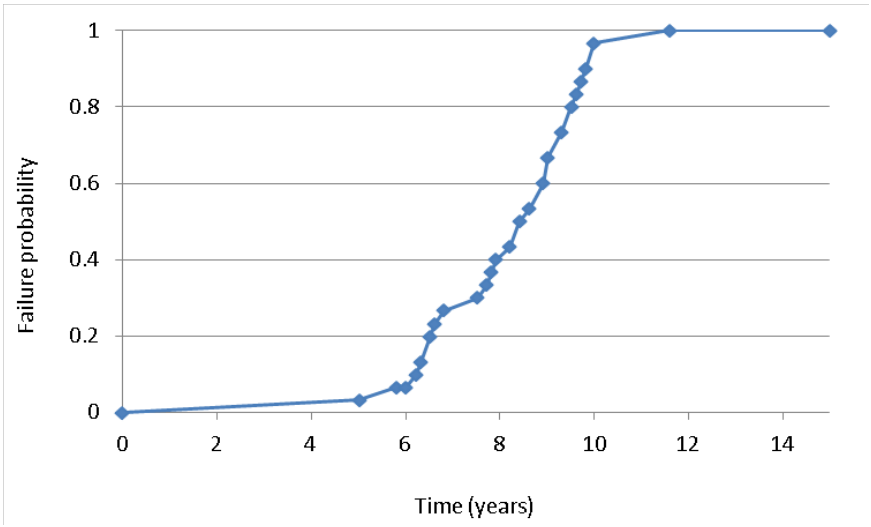

Figure 7.26: Failure probability of ATR-2E graphite brick vs. time.

Summary

A prismatic core reflector brick made of ATR-2E graphite was considered for the failure analysis. Thirty sets of fracture energy and strength were generated according to Weibull distribution and assigned to the brick model. For each of the thirty cases, stresses

and fracture were simulated for the reflector brick. For all the cases considered cracking initiated at the outer surface of the brick and propagated rapidly through the thickness towards the control rod channel. Since no failure was observed before 5 years the failure probability was zero during this time range. Most of the bricks failed in the time range of 6-10 years. Therefore, the failure probability rose steeply after 5 years of reactor operation. All the specimens failed by the end of 11.6 years.

7.4 Monte Carlo 3D Failure Analysis of a Prismatic Reflector Brick

A Prismatic reactor core ATR-2E graphite brick was modeled in 3D using the commercial finite element software Abaqus. For simplification the fuel handling hole and the dowel pin holes were not included in the brick model. The brick model is shown in Figure 7.27. The internal stresses caused by temperature and irradiation and consequent cracking were predicted using the user-defined subroutine UMAT in conjunction with XFEM technique. Monte Carlo failure analysis and evaluation of failure probability as a function of time were carried out as described earlier for 2D analysis in section 7.3.

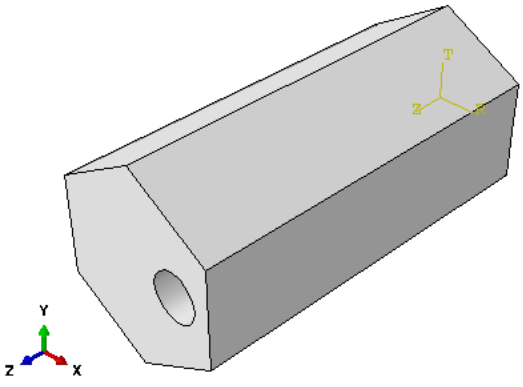

Figure 7.27: A Prismatic reactor core brick model.

FE Simulation

The brick was meshed with 32,224 C3D8 (continuum 3D 8-node linear isoparametric) elements as shown in Figure 7.28. Figure 7.28 also shows the boundary conditions on the model. The irradiation dose distribution was based on the operating conditions for a reflector brick in the Ft. St. Vrain reactor as presented in [2]. Due to unavailability of temperature distribution data for the prismatic reflector brick, a temperature distribution based on simple assumptions was used for the numerical analysis (see Figure 7.29).

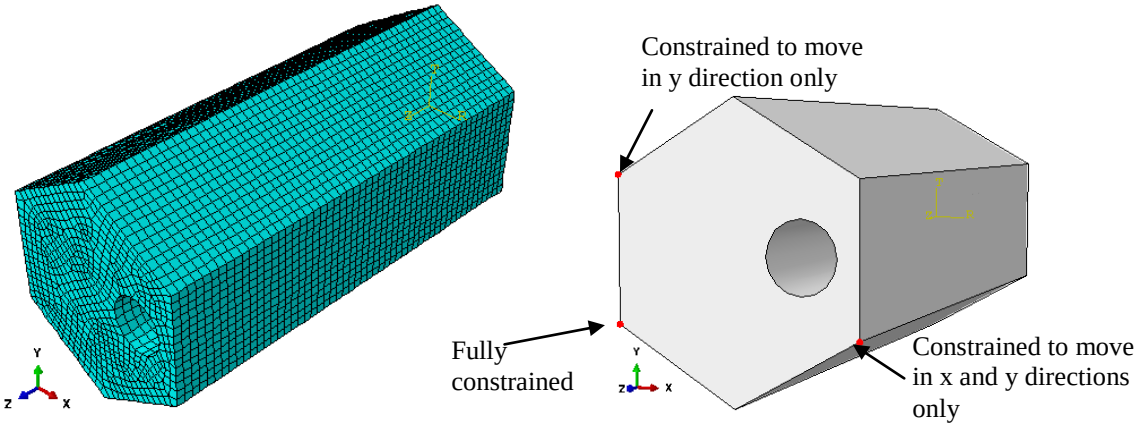

Figure 7.28: Mesh of 3D FE model (left) and boundary conditions on the brick (right).

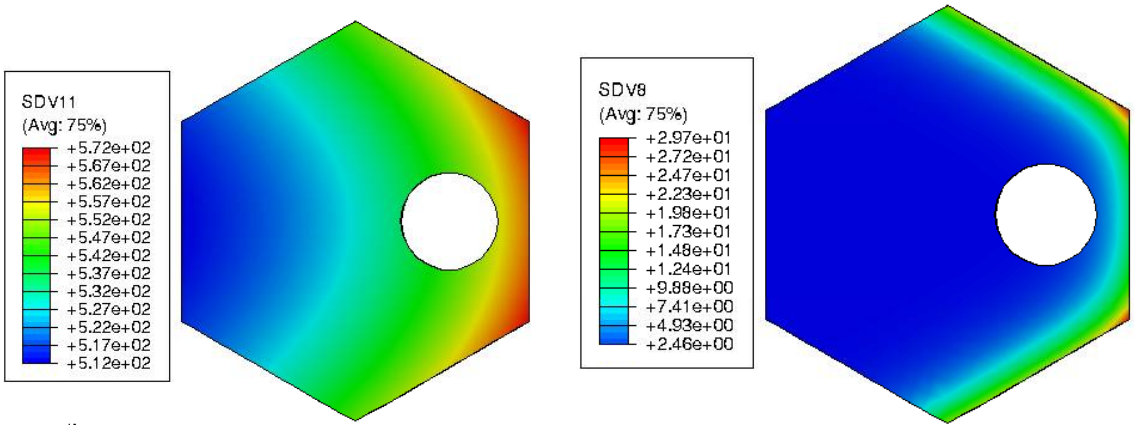

Figure 7.29: Temperature distribution (left) and irradiation dose distribution (x10^{20} n/cm^2) (right) in the prismatic reactor core brick at the end of 6 years.

The variation of strength with irradiation was incorporated in the work presented herein. Data on the dependence of strength on irradiation dose for ATR-2E graphite was not available. Therefore, a trend similar to that found for IG-110 graphite [3] was assumed, as shown in Figure 7.30. An Abaqus based user-subroutine, USDFLD, was coded for implementing the irradiation-dependence of strength in the finite element analysis. The variation of fracture toughness with irradiation was not considered.

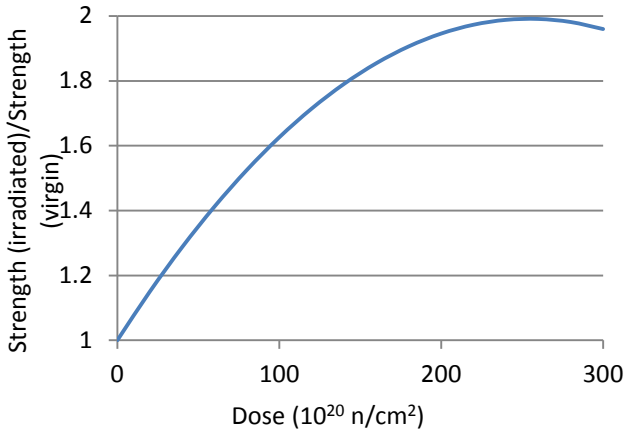

Figure 7.30: Variation of strength with irradiation dose [3].

Results and Discussion

The finite element model was run in Abaqus for each of the thirty sets of fracture energy and strength. Figure 7.31 shows the maximum principal stress distribution in the graphite brick at the end of 1.5, 3.0, 4.5, 6.0, 7.5 and 9.6 years for Case 7 (σ_f = 11.7 MPa, G_{IC} = 106.93 J/m^2).

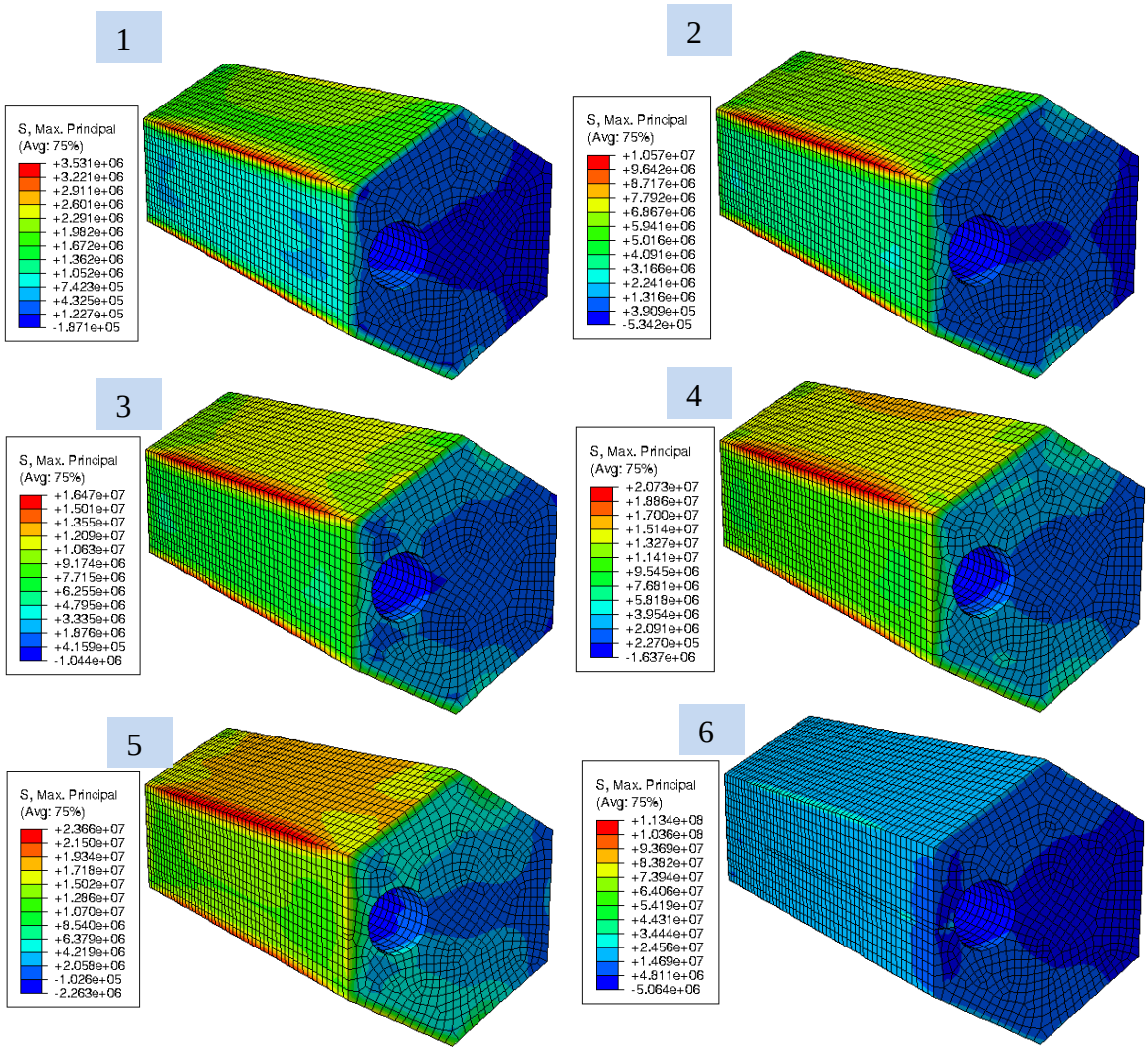

Figure 7.31: Distribution of maximum principal stress at the end of 1.5, 3.0, 4.5, 6.0, 7.5 and 9.6 years, shown in pictures numbered 1, 2, 3, 4, 5 and 6, respectively for Case 7 (σ_f = 11.7 MPa, G_{IC} = 106.93 J/m^2).

Figure 7.32 shows the variation of the maximum principal stress with time at two locations of the brick for Case 7. The maximum principal stress was greater at element A than the stress at element B during the entire reactor operation time. This difference in the stresses can be attributed to the fact that element A is nearer to the fuel brick and therefore receives greater dose of irradiation than element B. Figure 7.32 also shows some kinks in stress-time curve for element A. These kinks are due to crack initiation and

propagation. The stress-time curve for element B does not show such kinks because of the farther location of element B from the crack location.

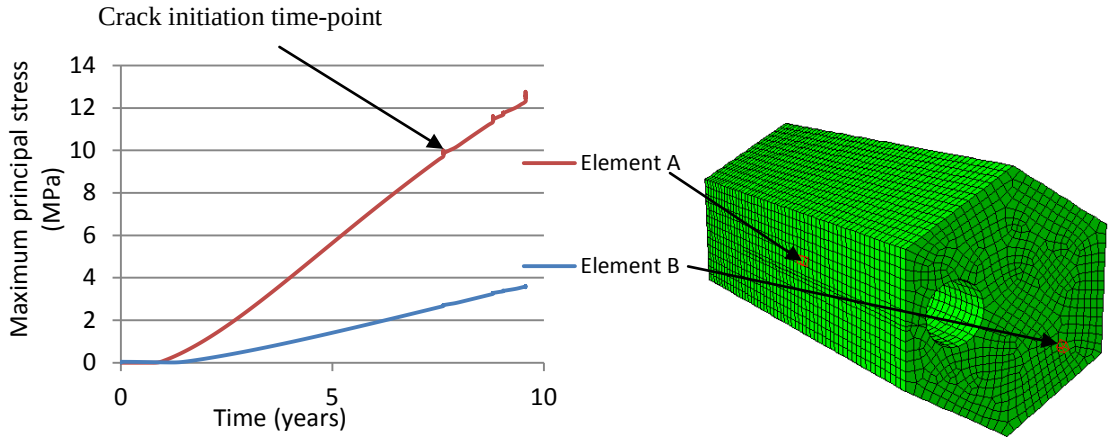

Figure 7.32: Variation of maximum principal stress with time at the inner and outer surfaces of the brick for Specimen 7 (σ_f = 11.7 MPa, G_{IC} = 106.93 J/m^2).

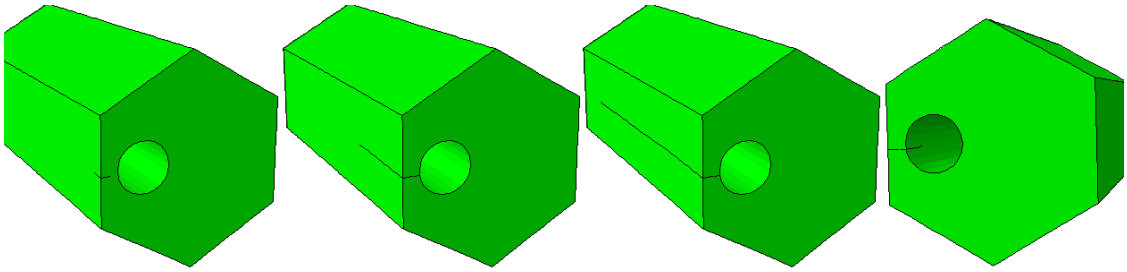

Figure 7.33: Crack propagation with time through a graphite brick model.

Figure 7.33 shows the crack propagation through the length and thickness of the graphite brick. The failure time was taken to be equal to the crack initiation time. Table 7.5 lists the crack initiation time for all the specimens. It was found that the shortest crack initiation time happened with Specimen 28, which had the lowest strength in the group. The crack in this specimen initiated at the 4th year. For all the specimens cracking occurred at the outer surface. For most of the specimens, crack initiated just ahead of the control rod channel of the brick and propagated along the longitudinal and radially-inward direction as shown in Figure 7.33. Crack initiation at the outer surface can be

explained from Figure 7.33, which shows that the maximum principal stress occurs at the outer surface of the brick, making it most susceptible to fracture. In a few specimens, cracking occurred at the outer longitudinal edge of the specimen as shown in Figure 7.34. Such cracks could not have been modeling with 2D FE models.

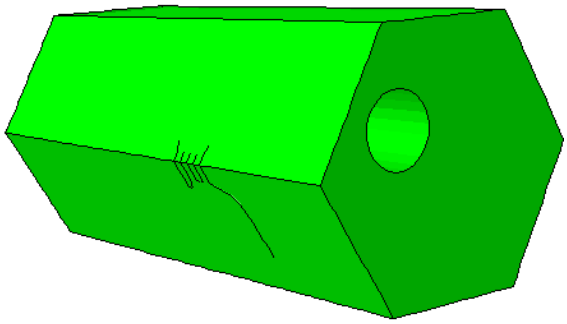

Figure 7.34: Crack on the outer edge of the graphite brick model (Specimen 28).

In the numerical analysis, not only was the variation in strength of the brick specimens incorporated, the strength was also assumed to be dependent on the irradiation dose which was non-uniformly distributed over the brick specimen and also varied with time. Therefore, the different locations of the cracks in some specimens were due to the dissimilar strengths of the specimens. It can be noted from Table 7.5 that the brick specimens with higher unirradiated strengths had longer lives.

Table 7.5: Fracture toughness, strength and the corresponding crack initiation time for all specimens.

Specimen number	G (J/m^2)	Strength (Pa) (un-irradiated)	Crack initiation time (years)
1	102.47	13887552.87	9.4
2	112.05	14080373.8	9.6
3	107.68	11881528.27	7.7
4	103.8	10713307.57	6.7
5	97.3	9276372.197	6.0
6	91.78	13531179.51	9.1
7	106.93	11729788.11	7.5
8	114.44	12118053.11	7.8
9	114.19	14748369.47	10.4
10	112.01	12616799.76	8.2
11	99.59	13359223.65	8.9
12	112.07	10618339.73	6.6
13	100.55	12716674.09	8.4
14	112.27	11890412.62	7.7
15	94.81	13341876.42	8.9
16	110.38	11592666.2	7.5
17	113.17	12908567.45	8.3
18	112.13	11364914.11	7.3
19	105.61	11200021.4	7.2
20	108.26	10894350.74	6.9
21	110.35	12189317.59	8.0
22	99.964	13826740.88	9.4
23	106.21	13050776.05	8.6
24	106.89	9573306.63	5.7
25	95.70	13409348.67	8.9
26	111.5	10402105.93	6.4
27	102.31	11851814	7.7
28	102.41	6743920.79	3.9
29	109.86	13869423.34	9.4
30	106.55	12218937.04	7.9

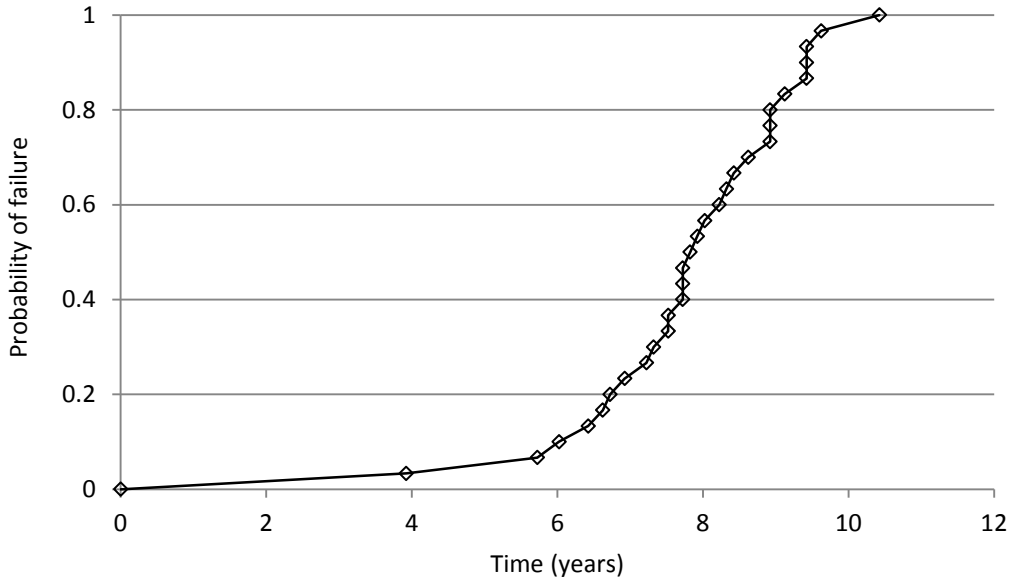

Figure 7.35: Failure probability of ATR-2E graphite brick vs. time.

Finally, the failure probability of the ATR-2E graphite brick as a function of time was obtained according to Equation 7.3, as shown in Figure 7.35. It can be seen that most of the brick specimens failed during the period of 6-10 years and the failure probability was low (0.1) up till 6 years and rose steeply thereafter.

Summary

Thirty different sets of values of strength and critical fracture energy for ATR-2E graphite were randomly generated based on the Weibull distribution. Linear spatial distributions of dose and temperature in the brick were assumed and the dependence of strength on irradiation dose was considered. For each of the thirty cases, stresses and cracking were simulated for the prismatic reactor graphite brick. For most cases, cracking initiated at the outer surface of the brick, near the control rod channel and propagated rapidly along the longitudinal and radially-inward direction of the brick specimen.

However, in some cases cracking occurred at other locations. The occurrence of cracking at multiple sites can be attributed to the different variation of stresses at different locations as shown in figures 7.24 and 7.32. The crack initiation site is the location where the (maximum principal) stress exceeds the strength of the material. Since, the strength vary across the bricks, the crack initiation site may also differ. Most of the bricks failed between 6 and 10 years. The failure probability of ATR-2E graphite bricks was found to be low up till 6 years and rose steeply thereafter.

Conclusion

Crack modeling technique XFEM was used in conjunction with the developed UMAT to estimate failure in simplified AGR and prismatic reflector graphite brick. Due to lack of data regarding properties of VHTR candidate materials the properties of ATR-2E were incorporated. This is a preliminary analysis and to predict the failure characteristics of VHTR graphite bricks more details regarding the material properties, irradiation dose and temperature distribution and their variation with time, boundary conditions on the brick will be needed. However, the work presented herein successfully illustrated an alternate method based on explicit crack modeling for estimating the failure of reflector bricks. The method can also be employed for performing structural integrity assessment of fuel bricks and other components of VHTR core.

The variation of probability of failure with time obtained from 3D analysis was found to be in good agreement with the failure probability evaluated through 2D analysis. For both the analyses crack initiated at the outer surface of the bricks. Compared to the 2D analysis the computation time for 3D analysis was much more (about 6-10 times). However, through the 3D analysis fracture in the longitudinal direction was predicted

which was not possible for 2D analysis. Also, through the 3D analysis different locations of crack occurrence were predicted while 2D analysis predicted only one crack initiation site. Since, the crack propagation along the longitudinal direction was found to be almost instantaneous the failure times for the graphite bricks did not change significantly for the 3D analysis in comparison to those obtained from 2D analysis; also, the variation of failure probability with time was found to be similar. However, this result may not hold true for a brick with more complex geometry. In such case the failure time evaluated through 3D analysis may differ significantly from that obtained through 2D analysis.

7.5 FAILURE ESTIMATION OF BRITISH AGR REACTORS

Several Advanced Gas-Cooled Reactor (AGR) British reactors were reported to have developed cracks in their core made of graphite. The time of occurrence of first cracks was not known but British energy, the company who owned the reactors, voiced concerns about the cracks as early as in 2004 [4]. In 2006 reactors Hinkley Point B, Somerset (switched on in 1976), Hartlepool, Cleveland (1983), Hunterston B, Ayrshire (1976), Heysham 1, Lancashire (1983) were reported to have their core damaged. Besides, there were hints based on documents that new cracks were found in the core of reactors such as Dungeness, Kent (1983), Torness, East Lothian (1988) [5]. Recently, in 2014, there were further reports [6] about keyway-root cracking in Hunterston B reactor. With the motivation to see the effect of stress concentrators on the fracture of a graphite brick fracture simulation was performed for an AGR brick which has keyway roots with sharp corners.

The AGR graphite brick was modeled using the commercial finite element software Abaqus. The geometry of the brick was obtained from reference [7]. Figure 7.36 shows the computer model of the reflector brick used for the numerical analysis. Brick was considered to be made of ATR-2E graphite and subjected to high temperature and irradiation dose. The irradiation dose distribution and its variation were assumed based on reference [8].

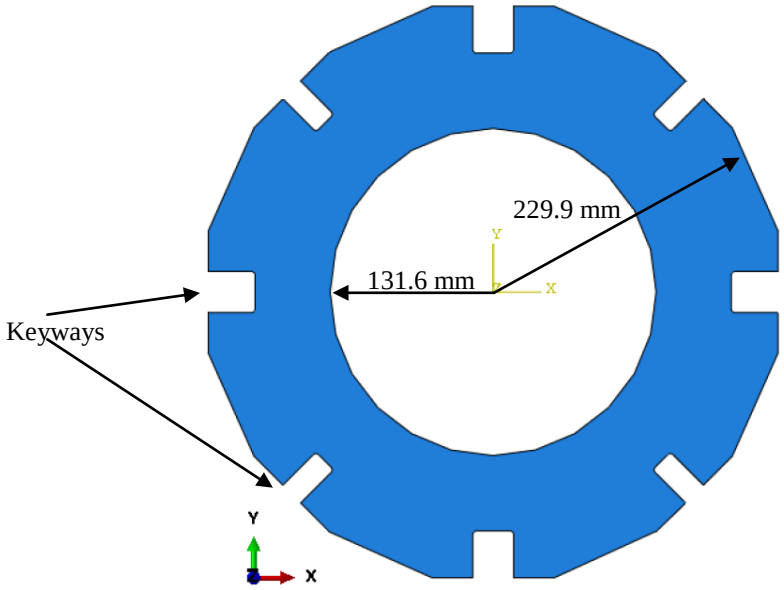

Figure 7.36: AGR reflector brick model.

The model was meshed with 12519 CPS4 elements with 12955 nodes as shown in Figure 7.37. Figure 7.37 also shows the boundary conditions applied to the model. Due to unavailability of temperature distribution data for the prismatic reflector brick, a realistic temperature distribution based on simple assumptions was used for the numerical analysis (see Figure 7.38). Irradiation dose and temperature were assumed to increase linearly with time.

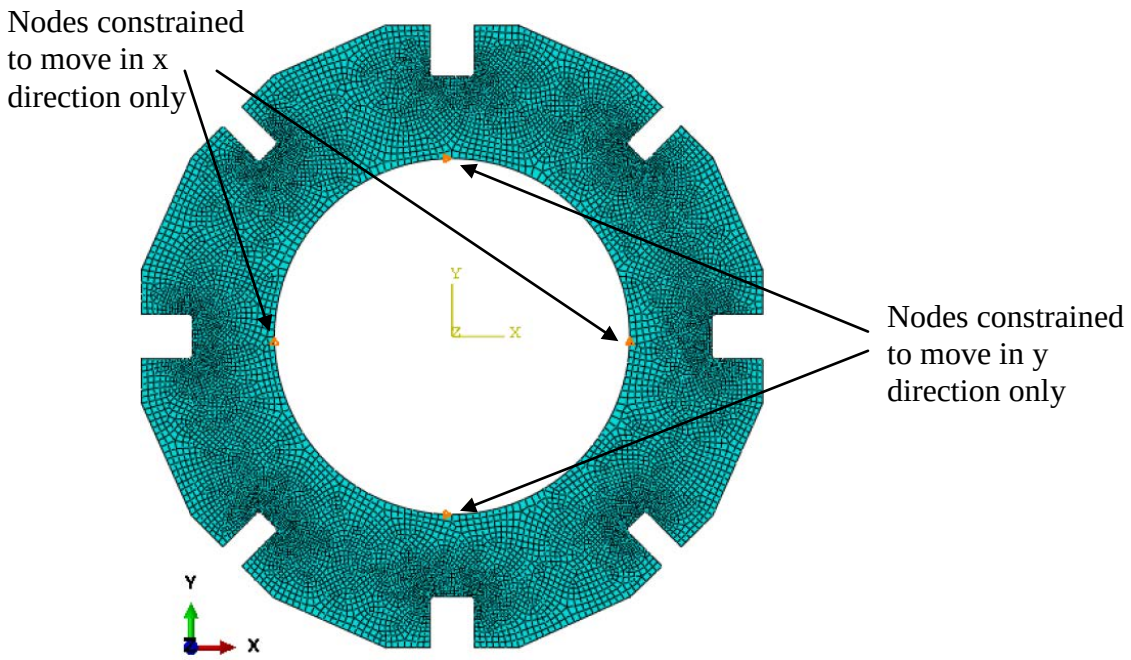

Figure 7.37: Meshed model of the AGR reflector brick with boundary conditions.

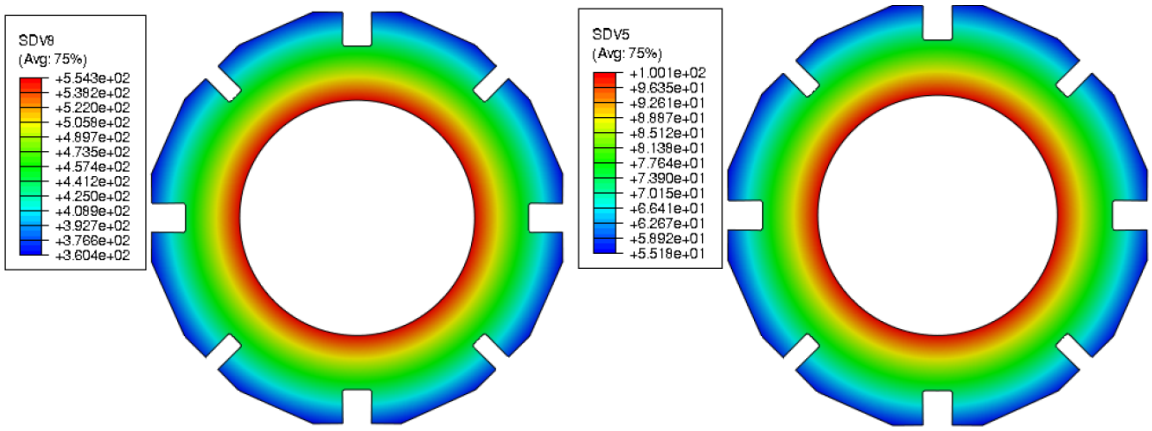

Figure 7.38: Temperature distribution (left) and irradiation dose distribution ($x10^{20}n/cm^2$) (right) in the AGR reactor core brick at the end of 15 years.

Results and Discussion

Figures 7.39 and 7.40 show the distribution of maximum principal stress in the AGR brick at the end of 4 years and 18 years respectively. At the end of 4 years the outer region of the brick was under compression while the inner region was under tension.

However, after 18 years the nature of the stress was found to have been reversed due to turnaround: the outer region was under tension while the inner region was under compression. Figure 7.40 shows the presence of high stresses at the keyway roots.

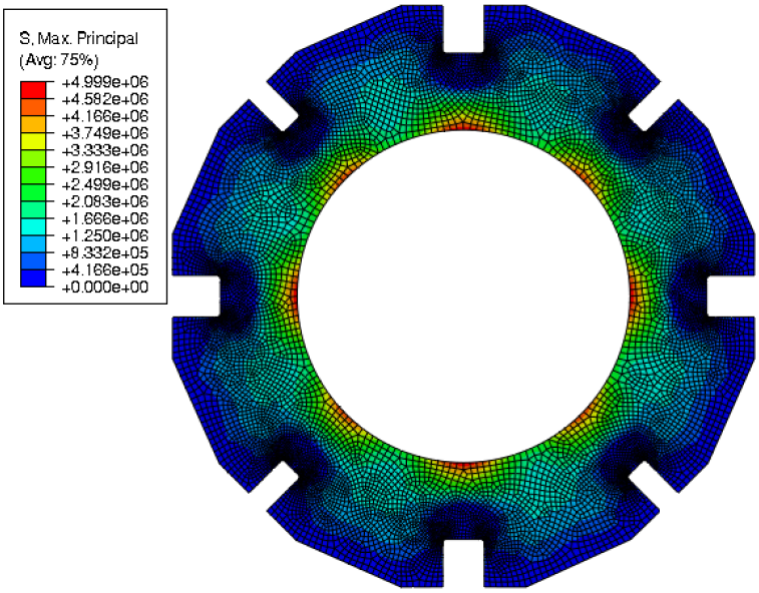

Figure 7.39: Maximum principal stress distribution in the AGR brick after 4 years of operation.

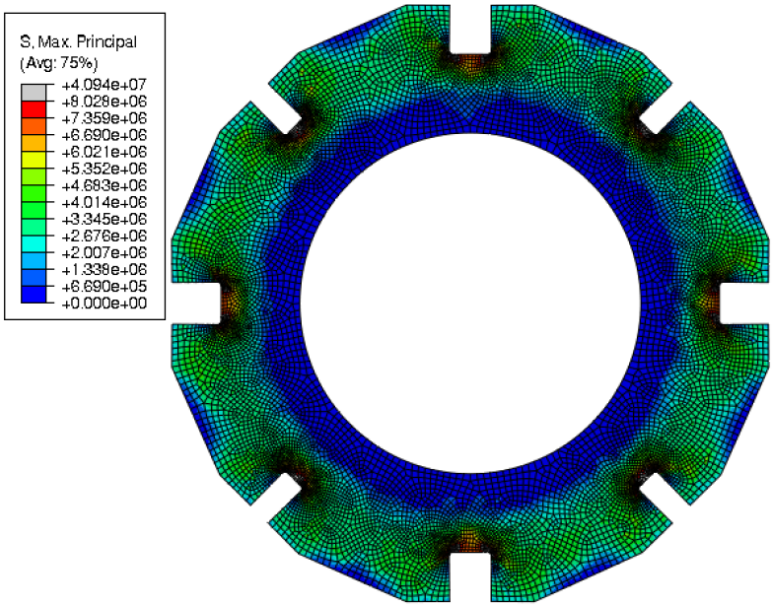

Figure 7.40: Maximum principal stress distribution in the AGR brick after 18 years of operation.

Figures 7.41 shows that a crack occurred in the brick after 18 years of its operation. Figure 7.42 shows crack path after 22 years of operation. From the numerical results the crack was found to have initiated at the keyway root. The location of crack initiation site is in congruence with the cracks found in Hunterston reactors: the cracks were reported to have occurred at the keyway. The initiation of crack at this particular site can be explained on the basis of stress concentration. Due to the presence of sharp corners in the keyway stresses rise in magnitude at this location leading to crack formation.

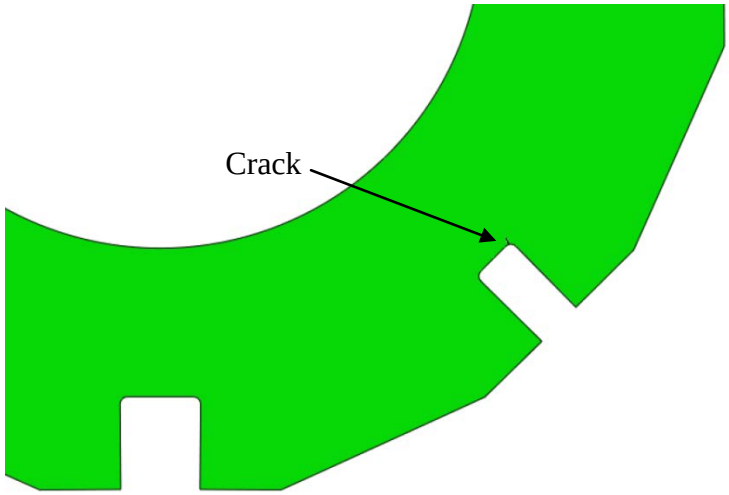

Figure 7.41: Occurrence of crack at the keyway in the AGR brick after 18 years of operation.

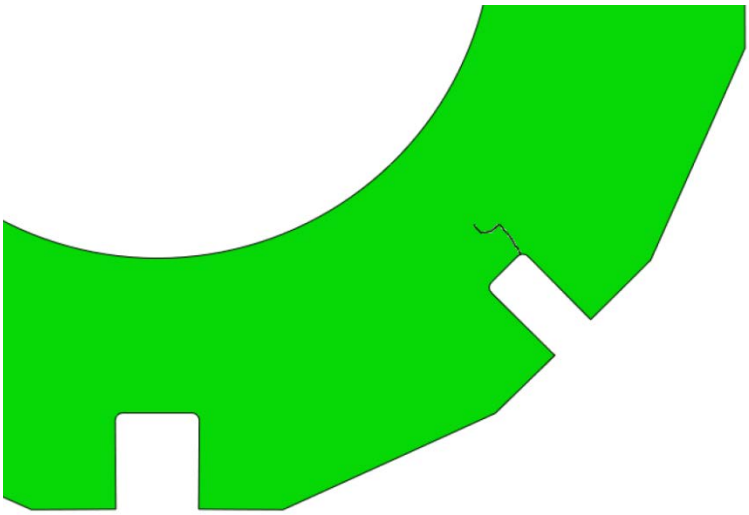

Figure 7.42: Crack path after 22 years of reactor operation.

The results of this analysis are encouraging as the location of occurrence of crack is in agreement with the reports. However, further analysis, which incorporates the precise material properties, irradiation and temperature distribution as those present in British reactor cores, is required along with detailed failure data about the reactors for performing a rigorous validation. Due to lack of this detailed information 2D analysis was not followed by 3D analysis.

7.6 REFERENCES

1. G. Haag, Properties of ATR-2E Graphite and Property Changes Due to Fast Neutron Irradiation, Institute for Safety Research and Reactor Technology.

2. R.L. Bratton, Modeling Mechanical Behavior of a Prismatic Replaceable Reflector Block, Idaho National Laboratory, Next Generation Nuclear Plant Project, INL/EXT-09-15868, 2009.

3. S. Ishiyama, T.D. Burchell, J.P. Strizak and M. Eto, The Effect of High Fluence Neutron Irradiation on the Properties of a Fine-Grained Isotropic Nuclear Graphite, Journal of Nuclear Materials, 230, 1-7, 1996.

4. http://www.theguardian.com/science/2006/jul/05/energy.greenpolitics, last accessed on December 15, 2014.

5. http://www.theguardian.com/science/2006/jul/05/energy.frontpagenews, last accessed on December 15, 2014.

6. http://www.bbc.com/news/science-environment-29481481, last accessed on December 15, 2014.

7. G. Hall, B. Marsden, J.S. Smart and A. Fok, Finite Element Modeling of Nuclear-Grade Graphite, Nuclear Energy, 41(1), 53-62, 2002.

8. H. Li, A. Fok, B. J. Marsden, An Analytical Study on the Irradiation – Induced Stresses in Nuclear Graphite Moderator Bricks, Journal of Nuclear Materials, 372, 164 – 170, 2008.

8. CONCLUSIONS

8.1 CONCLUDING REMARKS

Due to large variations in the fracture properties of brittle and quasi-brittle materials, it is a challenge for engineers and material scientists to accurately predict the failure of components and structures made of these materials. Several models have been proposed in the past for this purpose. The Weibull model is the most extensively used model for estimating the failure probability of brittle components/structures, but it has limitations: a) the model over-predicts the failure probability for structures having stress concentrators, b) an empirical parameter of the model, which should be a material constant, has been found to depend on the strain gradients in the structure and c) size effect trends, contradictory to the trends predicted by the Weibull model, have been found. These shortcomings and limitations lead to inaccuracies in the predictions of failure probability. To accommodate the uncertainties that exist in these predictions, higher design margins must be taken which increase the cost of manufacturing. The work presented herein provides an alternative approach for accurately predicting failure in brittle/quasi-brittle structures and components.

The proposed approach is based on explicit crack modeling (ECM), i.e., failure probability of a structure is estimated through the modeling of cracking in the structure with randomly generated material properties to reflect its heterogeneity. Therefore, the factors which govern fracture in a structure (fracture energy, strength of the material, damage behavior of the material, heterogeneity in the material microstructure) are incorporated in the ECM approach. Being fundamentally based, the proposed approach

has the capability of not only determining the probability of failure more accurately than the currently existing models, it can also predict the statistical variation in the fracture properties and the effect of size on the fracture properties.

Validation of the ECM approach was performed by estimating the failure probabilities of L-shaped specimens subjected to tensile loading. The predictions of failure probability obtained through the ECM approach were compared with 1) the failure probabilities obtained from the Weibull model and also with 2) the failure probabilities determined from the experimental data. It was found that the ECM approach not only predicted the failure probability more accurately than the Weibull model but also correctly predicted the variation in the failure load. The study also demonstrated the ability of the ECM approach to handle stress concentrations.

The ECM approach can be implemented in two ways depending on whether the crack initiation site and crack path in the structure are known or not. If this information about cracking is known beforehand then heterogeneity can be incorporated along the path of the crack in the FE model: cohesive elements are employed along the crack path and assigned varying fracture properties. If this information about fracture is not known then heterogeneity is incorporated by assigning uniform fracture properties to each FE model with properties varying from model to model. In this case, the Extended Finite Element Method (XFEM) is employed for modeling cracking.

The ECM approach was employed to predict the effect of size on the fracture properties and the corresponding variation. The study involved simulating tensile and flexural tests for determining the fracture properties. For each test specimen, models of different sizes were considered. Since the approximate crack path is known for a standard

test, cracking was modeled through the cohesive element method. The predictions were compared with published data. A good agreement demonstrated the capability of the ECM approach to predict the size effect.

The ECM based methodology for predicting the failure of brittle/quasi-brittle components subjected to extreme physical conditions was illustrated through failure predictions of nuclear reactor core components. The work involved construction of a constitutive model for modeling stresses in the graphite components under operating conditions. The constitutive model was implemented through a user material subroutine in the commercial finite element (FE) software Abaqus. Since prior information about cracking in the components, i.e., crack initiation site and crack propagation path, is not known, fracture was simulated using the Extended Finite Element Method (XFEM). For incorporating variation in the fracture properties of graphite, a number of FE models of a component were generated. Each model was assigned a set of fracture properties which varied across the FE models. The fracture properties were generated based on a Weibull distribution. The failure probability was calculated as a function of time from the fracture simulation results. The results show that, in addition to evaluating the failure probability of the components, the ECM approach can reveal crack initiation sites and crack paths possible in the components. Thus the ECM approach has the potential to contribute to the design guidelines and standards for the components and structures.

8.2 CONCLUSIONS

- The explicit crack modeling approach is capable of making more accurate predictions of failure probability in brittle/quasi-brittle components and structures than currently used approach based on the Weibull model.

- The Weibull model overestimates the probability of failure in components/structures having stress concentration but the approach based on explicit crack modeling handles stress concentration well and makes accurate failure predictions.
- As established in literature, the strain-gradient present in a component/structure affects the variation in the failure load: as strain gradient increases the spread in the data decreases. The explicit crack modeling approach is capable of predicting this trend of variation in the failure load with changes in the strain gradient.
- The level of heterogeneity in the intrinsic fracture properties of a brittle material affects the variation in its bulk properties. The explicit crack modeling approach, as presented herein, has the potential to give good understanding of the relationship between the micro and bulk level variation in the fracture properties.
- The explicit crack modeling approach can be used in conjunction with a user-material subroutine on a common computational platform to accurately and efficiently predict failure in components/structures subjected to complex physical conditions such as those present inside a nuclear reactor.
- For components/structures subjected to complex loading the crack initiation site depends on the distribution of fracture properties apart from the stress distribution, and therefore, there can be multiple/different sites of crack occurrence in a component. So, although simulation of cracking in three-dimensional FE models is more expensive than that in two-dimensional FE models, it is worthwhile for brittle and quasi-brittle components/structures subjected to complex loading conditions.

8.3 RECOMMENDATIONS

- The explicit crack modeling approach can be used to take a fresh look at the failure cases of brittle/quasi-brittle specimens in which the variation of the fracture property with size could not be explained though the Weibull model. The explicit crack modeling approach being fundamental in nature is capable of predicting atypical trends in fracture behavior.
- While carrying out this work difficulties were encountered in simulating fracture in heterogeneous FE models (elements having different fracture properties) using the XFEM. It was difficult to achieve convergence for the solution of such models. A study directed towards addressing this issue is recommended.
- In this work heterogeneity was considered separately in the FE models of the specimens employed in standard tests to determine the bulk fracture properties and their variation. The work needs to be extended by incorporating heterogeneity in the VHTR component models to understand its effect on the failure characteristics of these components.

BIBLIOGRAPHY

1. Population Reference Bureau, 2012, http://www.prb.org/pdf12/2012-population-data-sheet_eng.pdf, last accessed on December 21, 2014.
2. GE Energy, http://www.ge-energy.com/nuclear, last accessed on December 21, 2014.
3. A Technology Roadmap for Generation IV Nuclear Energy Systems, US DOE Nuclear Energy Research Advisory Committee, Generation IV International Forum, GIF-002-00, 12/2002.
4. D. Chapin, S. Kiffer and J. Nestell, The Very High Temperature Reactor – A Technical Summary, MPR Associates Inc. Engineers, 06/2004.
5. C. Kadak, A Future for Nuclear Energy – Pebble Bed Reactors, MIT, 04/2004.
6. S. Yu, H. Li, C. Wang and Z. Zhang, Probability assessment of graphite brick in the HTR – 10, Nuclear Engineering and Design, 227, 133 – 142, 2004.
7. P. D. Smith, R.M. Sullivan, A.C. Lewis and H.J. Yu, The Accuracy of Finite-Element Models for the Stress Analysis of Multiple-Holed Moderator Blocks, GA-A16234
8. P. D. Smith and D. Pelessone, Consistent Linearization Method for Finite-Element Analysis of Viscoelastic Materials, International Conference on Structural Mechanics in Reactor Technology, Chicago, USA, August 22-26, 1983.
9. T. Iyoku, M. Ishihara and H. Shirai, Development of Thermal/Irradiation Stress Analytical Code 'VIENUS' for HTTR Graphite Block, Journal of Nuclear Science and Technology, 28(10), 921-931, 1991
10. W. Weibull, A Statistical Theory of the Strength of Materials, Proc. Royal Swedish Academy of Eng. Sci., 151, 1-45, 1939.
11. W. Weibull, A Statistical Distribution Function of Wide Applicability, Journal of Applied Mechanics, 18, 293-297, 1951.
12. W. Weibull, The Phenomenon of Rupture in Solids, Ingeniors Vetenskaps Akademiens, Hadlingar, No. 153, 1939.
13. H. Li, A. Fok, B. J. Marsden, An Analytical Study on the Irradiation – Induced Stresses in Nuclear Graphite Moderator Bricks, Journal of Nuclear Materials, 372, 164 – 170, 2008.
14. D. K. L. Tsang and B. J. Marsden, The Development of a Stress Analysis Code for Nuclear Graphite Components in Gas-Cooled Reactors, Journal of Nuclear Materials, 350, 208-220, 2006.
15. S. Mohanty, R. Jain, S. Majumdar, T. J. Tautges and M. Srinivasan, Coupled Field Structural Analysis of HTGR Fuel Brick Using Abaqus, Proceedings of ICAPP 2012, Paper # 12352, Chicago, USA, June 24-28, 2012

16. W. Haitao, S. Libin, W. Hongtao, S. Li and Z. Zhensheng, Research on Structural Integrity of Graphite Core Internals in HTR-PM, Proceedings of HTR 2010, Paper 251, Prague, Czech Republic, October 18-20, 2010.
17. S. Mohanty, M. Saurindranath and M. Srinivasan, Constitutive Modeling and Finite Element Procedure Development for Stress Analysis of Prismatic High Temperature Gas Cooled Reactor Graphite Core Components, Nuclear Engineering and Design, 260, 145-154, 2013.
18. H. Schiffers, G Keist, G Haag and W. Hammer, Analysis of Stress and Deformation of Reactor Graphite, 1977.
19. B.C. Mitchell, J. Smart, S.L. Fok and B.J. Marsden, The Mechanical Testing of Nuclear Graphite, Journal of Nuclear Materials, 322, 126-137, 2003.
20. H. Li and A.S.L. Fok, An Analytical Study on the Effects of Strain Gradient on the Fracture Statistics of the Quasi-Brittle Materials, Journal of Nuclear Materials, 394, 136-143, 2009.
21. Z. Zou, S.L. Fok, B.J. Marsden and S.O. Oyadiji, Numerical Simulation of Strength Test on Graphite Moderator Bricks Using a Continuum Damage Mechanics Model, Engineering Fracture Mechanics, 73, 318-330, 2006.
22. X.P. Xu and A. Needleman, Numerical Simulations of Fast Crack Growth in Brittle Solids, J. Mech. Phys. Solids, 42(9), 1397-1434, 1994.
23. L. Shi, H. Li, Z. Zou, A.S.L. Fok, B.J. Marsden, A. Hodgkins, P.M. Mummery and J. Marrow, Analysis of Crack Propagation in Nuclear Graphite Using Three-Point Bending of Sandwitched Specimens, Journal of Nuclear Materials, 372(2-3), 141-151, 2008.
24. T.D. Burchell, A Microstructurally Based Fracture Model for Polygranular Graphites, Carbon, 34(3), 297-316, 1996.
25. C. Berre, S.L. Fok, B.J. Marsden, L. Babout, A. Hodgkins, T.J. Marrow and P.M. Mummery, Numerical Modeling of the Effects of Porosity Changes on the Mechanical Properties of Nuclear Graphite, Journal of Nuclear Materials, 352, 1-5, 2006.
26. C. Berre, S.L. Fok, B.J. Marsden, P.M. Mummery, T.J. Marrow and G.B. Neighbour, Microstructural Modelling of Nuclear Graphite Using Multi-Phase Models, 380, 46-58, 2008.
27. C. Berre, S. L. Fok, P. M. Mummery, J. Ali, B. J. Marsden, T. J. Marrow and G. B. Neighbour, Failure Analysis of the Effects of Porosity in Thermally Oxidised Nuclear Graphite Using Finite Element Modelling, Journal of Nuclear Materials, 381(1-2), 1-8, 2008.
28. Z.J. Yang, X.T. Su, J.F. Chen and G.H. Liu, Monte Carlo Simulation of Complex Cohesive Fracture in Random Heterogeneous Quasi-Brittle Materials, International Journal of Solids and Structures, 46, 3222-3234, 2009.
29. F.T. Peirce, “The Weakest Link” Theorems of the Strength of Long and of Composite Specimens, J. Textile Inst., 17, 355-368, 1926.

30. Z. P. Bazant and J. Planas, Fracture and Size Effect in Concrete and Other Quasibrittle Materials, CRC Press, 1998.

31. C. Lu, R. Danzer and F.D. Fischer, Failure Statistics of Brittle Materials: Weibull or Normal Distribution, Physical Review E., 65, 067102, 2002.

32. A. M. Freudenthal, Statistical Approach to Brittle Fracture, Fracture, Academic Press, 2, 591-619, 1969.

33. R. L. Barnett, C. L. Connors, P. C. Hermann and J. R. Wingfield, Fracture of Brittle Materials Under Transient Mechanical and Thermal loading, U.S. Air Force Flight Dynamics Laboratory, AFFDL-TR-66-220, 1967.

34. P. Stanley, H. Fessler and A.D. Sivill, An Engineer's Approach to the Prediction of Failure Probability of Brittle Components, The University of Nottingham.

35. S. L. Fok and J. Smart, The Accuracy of Failure Predictions Based on Weibull Statistics, Journal of European Ceramic Society, 15, 905 – 908, 1995.

36. J.E. Brocklehurst, Fracture in Polycrystalline Graphite, Chemistry and Physics of Carbon, New York, NY, 13, 146–272, 1977.

37. J.P. Strizak, The Effect of Volume on the Tensile Strength of Several Nuclear-Grade Graphites, The Status of Graphite Development for Gas Cooled Reactors, IAEA–TECDOC–690, 233–241, 1991.

38. Z. Zou, S.L. Fok, S.O. Oyadiji and B.J. Marsden, Failure Predictions for Nuclear Graphite Using a Continuum Damage Mechanics Model, Journal of Nuclear Materials, 324, 116-124, 2004.

39. Abaqus Documentation, Dassault Systemes Simulia Corp., Providence, RI, USA.

40. T. Belytschko, and T. Black, Elastic Crack Growth in Finite Elements with Minimal Remeshing, International Journal for Numerical Methods in Engineering, 45, 601-620, 1999.

41. J. Melenk, and I. Babuska, The Partition of Unity Finite Element Method: Basic Theory and Applications, Computer Methods in Applied Mechanics and Engineering, 39, 289-314, 1996.

42. J. J. C. Remmers, R. de Borst and A. Needleman, The Simulation of Dynamic Crack Propagation using the Cohesive Segments Method, Journal of the Mechanics and Physics of Solids, 56, 70–92, 2008.

43. J. H. Song, P.M.A. Areias and T. Belytschko, A Method for Dynamic Crack and Shear Band Propagation with Phantom Nodes, International Journal for Numerical Methods in Engineering, 67, 868–893, 2006.

44. H. Li, J. Li, G. Singh and A. Fok, Fracture Behavior of Nuclear Graphite NBG-18, Carbon, 60, 46-56, 2013.

45. H. Wang, X. Zhou, L. Sun, J. Dong and S. Yu, The effect of stress levels on the coefficient of thermal expansion of a fine – grained isotropic nuclear graphite, Nuclear Engineering and Design, 239, 484 – 489, 2009.

46. S. Ishiyama, T.D. Burchell, J.P. Striazak and M. Eto, The effect of high fluence neutron irradiation on the properties of a fine – grained isotropic nuclear graphite, Journal of Nuclear Materials, 230, 1 -7, 1996.

47. H. Matsuo, Effect of high temperature neutron irradiation on dimensional change and physical properties of nuclear graphite for HTGR. JAERI-M87-207.

48. I.G. Lebedev, O.G. Kochkarev and Y.S.Virgil'ev, Radiation – Induced change in the properties of isotropic structural graphite, Atomic energy, 93(1), 589 – 594, 2002.

49. T. Konishi, M. Eto and T. Oku, High temperature Young's Modulus of IG – 110 Graphite, JAERI-M86-192.

50. G. Haag, Properties of ATR-2E Graphite and Property Changes Due to Fast Neutron Irradiation, Institute for Safety Research and Reactor Technology.

51. R.L. Bratton, Modeling Mechanical Behavior of a Prismatic Replaceable Reflector Block, Idaho National Laboratory, Next Generation Nuclear Plant Project, INL/EXT-09-15868, 2009.

52. The Guardian, http://www.theguardian.com/science/2006/jul/05/energy.greenpolitics, last accessed on December 15, 2014.

53. The Guardian, http://www.theguardian.com/science/2006/jul/05/energy.frontpagenews, last accessed on December 15, 2014.

54. British Broadcasting Corporation, http://www.bbc.com/news/science-environment-29481481, last accessed on December 15, 2014.

55. G. Hall, B. Marsden, J.S. Smart and A. Fok, Finite Element Modeling of Nuclear-Grade Graphite, Nuclear Energy, 41(1), 53-62, 2002.

56. J.E. Brocklehurst and M.I. Darby, Concerning the Fracture of Graphite under Different Test Conditions, Material Science and Engineering, 16, 91-106, 1974.

57. M.J. Holt and G.B. Neighbour, Examining the Issues of Scale in Nuclear Graphite Components, Basic Studies in the Field of High Temperature Engineering, Third Information Exchange Meeting, Ibaraki-Ken, Japan, 153, 2003.

58. J. Amesz, J. Donea and F. Lanza, 11th Biennial Conference on Carbon, Gatlinburg, Extended Abstracts, CONF-730601, 221, 1973.

59. Lanza, F. and Burg, H., 11th Biennial Conference on Carbon, Gatlinburg, Extended Abstracts, CONF-730601, 223, 1973.

60. P.R. Kasten, High-Temperature Gas-Cooled Reactor Technology Development Program, Annual Progress Report for Period Ending December 31, 1987. DOE−HGTR−88272 (ORNL−6502), 1989.

61. R.J. Price, Statistical Study of the Strength of Near-Isotropic Graphite. General Atomic Project 3224 (GA–A13955 and UC–77), 1976.

62. G. Quinn, Advanced Structural Ceramics: A Round Robin, Journal of the American Ceramic Society, 73(8), 2374-2384, 1990.

63. K. Matsusue, K. Takahara and R. Hashimoto, Strength Evaluation of Hot-Pressed Silicon Nitride at Room Temperature, Yogyo Kyokaishi, 90(4), 168, 1982.

64. Y. Katayama and Y. Hattori, Effects of Specimen Size on Strength of Sintered Silicon Nitride, Journal of American Ceramic Society, 65(10), C-164-C-165, 1982.

65. D.S. Dugdale, Yielding of Steel Sheets Containing Slits, Journal of Mechanics and Physics of Solids, 8, 100-108, 1960.

66. G.I. Barenblatt, The Mathematical Theory of Equilibrium of Cracks in Brittle Fracture, Advances in Applied Mechanics, 7, 55-129, 1962.

67. T. Burchell, Neutron Irradiation Damage in Graphite and Its Effects on Properties, Oak Ridge National Lab, Oak Ridge, TN, USA.

68. J.M. Vidal, and T.J. Mays, Mechanical Properties and Oxidation of Nuclear Graphites, University of Bath, UK.

69. ASTM, Standard Test Method for Determination of Fracture Toughness of Graphite at Ambient Temperature, ASTM-D7779-11, 2012.

70. J. Gong and Y. Li, Relationship between the Estimated Weibull Modulus and the Coefficient of Variation of the Measured Strength for Ceramics, J. Am. Ceram. Soc., 82(2), 449-452, 1999.

71. H. Mahiou and A. Beakou, Local Stress Concentration and the Prediction of Tensile Failure in Unidirectional Composites, Composites Science and Technology, 57(12), 1661-1672, 1998.

72. S.B. Batdorf and J.G. Crose, A Statistical Theory for the Fracture of Brittle Structures Subjected to Non-uniform Polyaxial Stresses, Journal of Applied Mechanics, 41(2), 459-464, 1974.

73. S.B. Batdorf and H.L. Heinisch, Weakest Link Theory Reformulated for Arbitrary Fracture Criterion, Journal of the American Ceramic Society, 61(78), 355-358, 1978.

74. J.R. Matthews, F.A. McClintock and W.J. Shack, Statistical Determination of Surface Flaw Density in Brittle Materials, Journal of the American Ceramic Society, 59(7-8), 304-308, 1976.

75. L.Y. Chao and D.K. Shetty, Equivalence of Physically Based Statistical Fracture Theories for Reliability Analysis of Ceramics in Multiaxial Loading, Journal of the American Ceramic Society, 73(7), 1917-1921, 1990.

76. F.M. Furgiuele and A. Lamberti, On the Equivalence of Two Weakest-Link Fracture Statistics Formulations, International Journal of Fracture, 51, R15-R20, 1991.

77. A.M. Freudenthal Statistical Approach to Brittle Fracture, in Fracture 2, Edited by H. Liebowitz, Academic Press, New York, 1969.

78. T. Burchell, T. Yahr and R. Battiste, Modeling the Multiaxial Strength of H-451 Nuclear Grade Graphite, Carbon, 45, 2570-2583, 2007.

79. A.G. Evan and R.L. Jones, Evaluation of a Fundamental Approach for the Statistical Analysis of Fracture, Journal of the American Ceramic Society, 61(3-4), 156-160, 1978.

80. National Aeronautics and Space Administration (NASA) Glenn Research Center, USA, http://www.grc.nasa.gov/WWW/StructuresMaterials/MLP/software/cares-life/index.html, last accessed January 12, 2015.

81. J. Le, Z.P. Bažant and M.Z. Bazant, Unified Nano-Mechanics Based Probabilistic Theory of Quasi-brittle and Brittle Structures: I. Strength, Static Crack Growth, Lifetime and Scaling, Journal of the Mechanics and Physics of Solids, 59, 1291-1321, 2011.

82. J. Le, Z.P. Bažant and M.Z. Bazant, Subcritical Crack Growth Law and its Consequences for Lifetime Statistics and Size Effect of Quasibrittle Structures, Journal of Physics D: Applied Physics, 42, 214008, 2009.

83. Z.P. Bažant and J. Le, Size Effect on Strength and Lifetime Probability Distributions of Quasibrittle Structures, Sādhanā, 37(1), 17-31, 2012.

84. J. Le, J. Eliáš and Z.P. Bažant, Computation of Probability Distribution of Strength of Quasibrittle Structures Failing at Macrocrack Initiation, Journal of Engineering Mechanics, 138(7), 888-899, 2012.

85. J. Le and Z.P. Bažant, Finite Weakest-Link Model of Lifetime Distribution of Quasibrittle Structures under Fatigue Loading, Mathematics and Mechanics of Solids, 19(1), 56-70, 2014.

APPENDIX A

p1	270
p2	385
q1	550
q2	387
a1	-4.00E-5
a2	0.0106
a3	3.35
b1	-2.374E-12
b2	1.88E-9
b3	-5.314E-7
b4	1.704E-4
b5	-3.444E-2
b6	-1.771E-2
c4	-5.081E-7
c5	2.378E-3
c6	-0.2439
d1	1.122E-12
d2	-7.999E-10
d3	-5.522E-7
d4	2.487E-4
d5	2.562E-2
d6	7.498
e1	2.99E-16
e2	-9.169E-13
e3	9.228E-10
e4	-1.938E-7
e5	2.265E-6
e6	0.9998
f1	6.114E-7
f2	-2.999E-4
f3	4.504E-2
f4	-1.7506
f5	1.817E1
f6	9.1029E3

APPENDIX B

The weakest link theory states that the failure of a brittle structure depends on the failure of its weakest link, i.e. the most critical flaw, but in reality multiple cracks, initiating and propagating at different times, are responsible for the failure of the structure. Therefore, predictions of the failure of brittle structures by the Weakest Link theory often differ from experimental observations. To account for multiple fractures occurring in a brittle structure, a numerical technique, the Extended Finite Element Method (XFEM), is used here which can explicitly model crack initiation and propagation. A study focused on the assessment of XFEM for modeling cracking in brittle specimens was conducted. The details of the study are presented here.

XFEM is a relatively new technique which can be used to solve differential equations with discontinuous functions. It has been implemented in Abaqus and other commercial finite element software to model discontinuities including cracks. It was developed by Belytschko et al. [1] in 1999 and is based on the unity partition function [2]. XFEM has significant advantages over the conventional finite element method for modeling crack problems as it obviates the needs of a very fine mesh to capture singular asymptotic fields and remeshing during crack propagation, thus makes the process of crack modeling less cumbersome and cheaper. Also, this technique allows the presence of discontinuities in an element by enriching it with special degrees of freedom which obviate the need to match the mesh with the geometry of the discontinuity [3]. Thus, the XFEM can be used to simulate crack initiation and propagation along an arbitrary, solution-dependent path.

B.1 MODELING CRACK PROPAGATION USING XFEM

The XFEM technique was explored for prediction of failure in brittle materials.

In Abaqus' implementation of the XFEM [3], the approximation for a displacement vector function u is given as:

$$\mathbf{u} = \sum_{i=1}^{N} N_I(x)[\mathbf{u}_I + H(x)\mathbf{a}_I + \sum_{i=1}^{N} F_\alpha(x)\mathbf{b}_I^\alpha] \quad \text{(B.1)}$$

where

$N_I(x)$: nodal shape function

a_I: nodal enriched degree of freedom vector which facilitates crack within element

H(x): discontinuous jump function across the crack surfaces

b_I: nodal enriched degree of freedom vector which accounts for singularity around crack tip

$F_\alpha(x)$: Elastic asymptotic crack tip functions

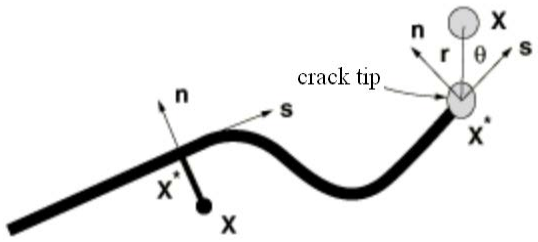

Figure B. 1: Normal and tangential coordinates for a smooth crack.

The discontinuous jump function across the crack surfaces has the form:

$$H(x) = \begin{cases} 1 & \text{if } (x - x^*).n \geq 0 \\ -1 & \text{otherwise} \end{cases} \quad \text{(B.2)}$$

where x is the sample (Gauss) point, x^* is the point on the crack closest to x and n is the unit outward normal to the crack at x^*. Figure B.1 shows the normal and tangential coordinate systems used in Abaqus for a crack.

The elastic asymptotic crack tip functions have the form:

$$F_\alpha(x) = [\sqrt{r}\sin\frac{\theta}{2}, \sqrt{r}\cos\frac{\theta}{2}, \sqrt{r}\sin\theta\sin\frac{\theta}{2}, \sqrt{r}\sin\theta\cos\frac{\theta}{2}] \quad \text{(B.3)}$$

where (r,θ) is the polar coordinate system having its origin at the crack tip and α can take a value from 1 to 4 depending on which of the functional form is chosen in equation B.3.

In Abaqus, the XFEM can be used to model cracking in two ways: 1) using the cohesive segment method [4] and phantom nodes [5] and 2) using the principles of linear elastic fracture mechanics and phantom nodes. Phantom nodes are the nodes which are imposed over the original nodes when there is no crack; these nodes get separated from the original nodes when a crack passes through the element. The cohesive segment method was used for assessing the capability of XFEM. This method can be used to model cracking in both ductile and brittle materials.

The available traction-separation model in Abaqus assumes initially linear elastic behavior followed by damage initiation and evolution. The initial normal, shear and tangential separations are linearly related to the corresponding traction stresses as:

$$\begin{Bmatrix} t_n \\ t_s \\ t_t \end{Bmatrix} = \begin{bmatrix} K_{nn} & 0 & 0 \\ 0 & K_{ss} & 0 \\ 0 & 0 & K_{tt} \end{bmatrix} \begin{Bmatrix} \delta_n \\ \delta_s \\ \delta_t \end{Bmatrix} \quad \text{(B.4)}$$

where t_n, t_s and t_t are the normal, shear and tangential tractions, δ_n, δ_s and δ_t are the corresponding displacements and K_{nn}, K_{ss} and K_{tt} are the stiffness matrix components based on elastic properties. However, once the damage initiation criterion is met the traction separation response of the element can be either linear or non-linear. A non-linear traction-separation response curve is shown in Figure B.2.

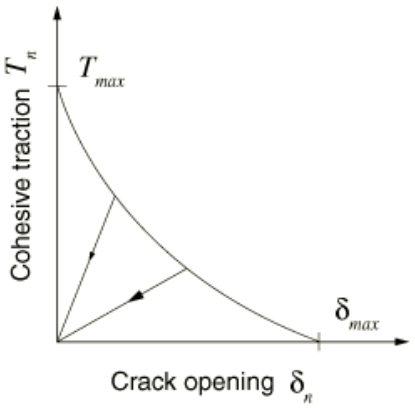

Figure B. 2: A non-linear traction-separation response for crack initiation [3].

A crack is said to be initiated when the cohesive response of the enriched element degrades. There are several criteria for crack initiation defined in Abaqus:

a) the maximum principal stress criterion

b) the maximum principal strain criterion

c) the maximum nominal stress criterion

d) the maximum nominal strain criterion

e) the quadratic traction interaction criterion

f) the quadratic separation interaction criterion

The maximum principal stress criterion was used for crack initiation. It is given as:

$$f = \frac{\langle \sigma_{max} \rangle}{\sigma^o_{max}} \tag{B.5}$$

where

$$\langle \sigma_{max} \rangle = \sigma_{max} \text{ if } \sigma_{max} > 0$$
$$\langle \sigma_{max} \rangle = 0 \quad \text{if } \sigma_{max} \leq 0 \tag{B.6}$$

σ^o_{max} is the maximum allowable principal stress. The crack initiates or extends when f reaches the value 1.0 within the given tolerance: $1 \leq f \leq f_{tol}$. Similarly, other criteria can be specified.

The damage evolution model specifies the rate of degradation of the cohesive stiffness after damage initiation. In Abaqus, it is implemented through a scalar variable D which represents the averaged overall damage at the intersection between the crack surfaces and the edges of the cracked elements. With no damage, its value is 0 and as damage occurs, its value increases up to 1. The normal and shear stresses are dependent on D as:

$$t_n = \begin{cases} (1 - D)T_n, & T_n \geq 0 \\ T_n \text{ (no damage to compressive stiffness)} \end{cases} \tag{B.7}$$

$$t_s = (1 - D)T_s$$

$$t_t = (1 - D)T_t$$

where T_n, T_s and T_t are the traction stresses for the corresponding separations without damage. Figure B.3 shows a crack passing through the enriched elements. The ability of the crack to pass through elements makes crack propagation solution-dependent i.e., crack progresses as the solution evolves; the crack path is not required to be known beforehand.

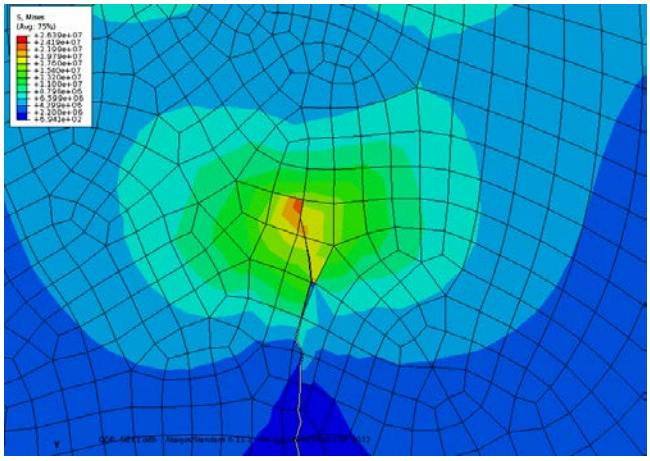

Figure B. 3: Crack propagation through the enriched elements.

B.2 ASSESSING THE VIABILITY OF XFEM

The possibility of using the Extended Finite Element Method (XFEM) for modeling fracture in brittle structures was explored by studying the effect of mesh type and mesh size on crack propagation behavior in 2D specimen models. Using the commercial finite element software Abaqus, the XFEM technique was employed to simulate crack propagation in graphite specimens under three-point bending. The specimen models used in the simulations were assigned same dimensions and material properties as were used in the experimental work conducted by Li et al. [6].

The effect of the mesh (type and size) on the predicted crack propagation behavior was studied using two dimensional models. To understand the sensitivity of the simulation to mesh type, the middle region of the beam through which the crack was expected to propagate was meshed in two ways: a) a structured mesh and b) an unstructured mesh, as shown in Figure B.4.

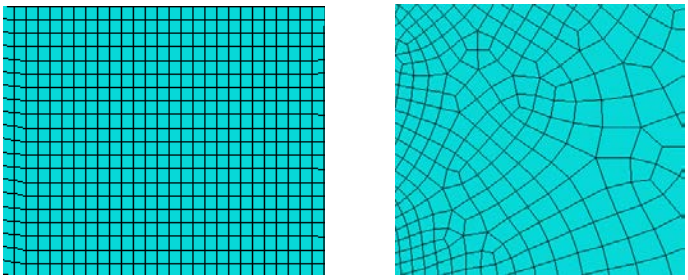

Figure B. 4: FE meshes: (a) structured and (b) unstructured.

To understand the effect of mesh size, the 2D graphite beam model was meshed with three different sized elements. From earlier analysis the structured mesh was found to give more consistent results and was therefore employed for carrying out this part of the

assessment. The simulation results for the three cases of mesh size were compared. All the computational results were compared with the experimental results and the percentage errors evaluated.

Mesh Sensitivity of Crack Propagation Simulation using 2D XFEM

Figure B.5 shows a 2D graphite beam model under three-point bending. An initial crack was built into the beam model using the assembly feature of Abaqus. The initial crack length to beam width ratio (a_o/W) was ≈ 0.4. Three beam sizes were considered. The dimensions of the graphite beams and initial crack lengths are given in Table B.1.

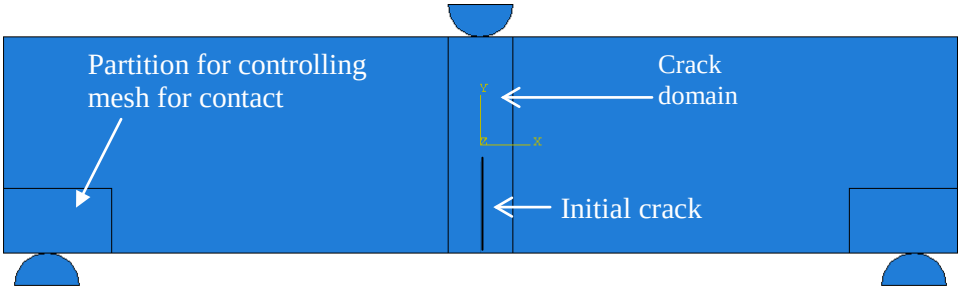

Figure B. 5: A three-point-bend beam model showing the initial crack, supports and loading bar.

Table B. 1: Dimensions of the three different sized graphite beams and their initial crack lengths.

Size	Total length (L/mm)	Span (S/mm)	Width (W/mm)	Thickness (B/mm)	Initial crack length (a_o/mm)
Size 1	220	200	50	25	21
Size 2	110	100	20	10	8
Size 3	45	40	10	5	4

Young's modulus (E) and Poisson's ratio (υ) of the graphite were assumed to be 12 GPa and 0.2, respectively. The maximum principal stress criterion was selected as the damage initiation criterion with the critical maximum principal stress taken to be 21 MPa.

The incorporated damage evolution law was based on fracture energy and the softening was assumed to be linear. The critical fracture energy (G_{IC}) was set as 188 J/m^2. It was calculated using the critical stress intensity factor (K_{IC}), which was experimentally found to be around 1.4 MPa$\sqrt{m}$ for the graphite tested [6], and the Irwin relationship:

$$G = (1-\upsilon^2)\frac{K^2}{E}.$$

Effect of Mesh Type on Crack Propagation Simulation Using 2D XFEM

To understand the effect of mesh type on the crack propagation behavior modeled by the XFEM, two kinds of mesh were considered: a) Unstructured mesh and b) Structured mesh (Figure B.4). Figures B.6 and B.7 show the models with unstructured and structured mesh, respectively, for the graphite specimen under three-point bending. The element type was CPS4R quad-shaped, plane-stress. The tangential behavior of the contact between the beam and the loading and supporting bars was modeled using penalty formulation and included friction with a coefficient of 0.1. Finite sliding was prescribed so as to allow free relative motion between the surfaces in contact. The three different sized beams, as shown in Table B.1, were all modeled using both the structured and unstructured mesh. Table B.2 shows the total number of elements in each model. The number of elements for the structured and unstructured meshes was kept roughly the same for each beam size.

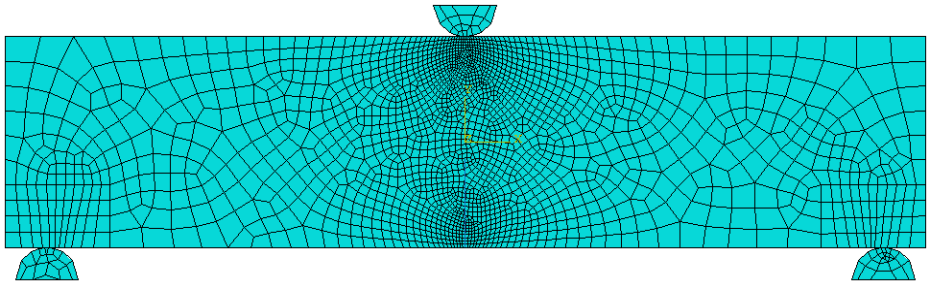

Figure B. 6: A three-point-bending graphite beam model with unstructured mesh in the middle region.

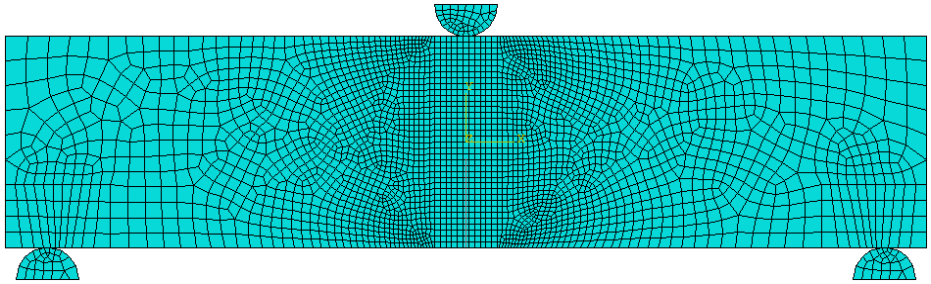

Figure B. 7: A three-point-bending graphite beam model with structured mesh in the middle region.

Table B. 2: Total number of elements in the graphite beam models.

	Unstructured mesh	Structured mesh
Size 1	2932	2910
Size 2	2401	2514
Size 3	2925	2719

The two support bars were fixed and a vertical displacement was applied from the top loading roller. The three-point bending model was solved using Abaqus Standard [3]. The numerical simulation was stabilized using viscous regularization. Viscous coefficient of 1×10^{-5} was assigned. The viscous regularization ensures that the tangent stiffness remains positive definite thereby improving the convergence rates [3]. Figures B.8, B.9 and B.10 show the predicted crack paths with unstructured and structured meshes for beam sizes 1, 2 and 3 respectively.

B.3 Results and Conclusions

Effect of mesh type

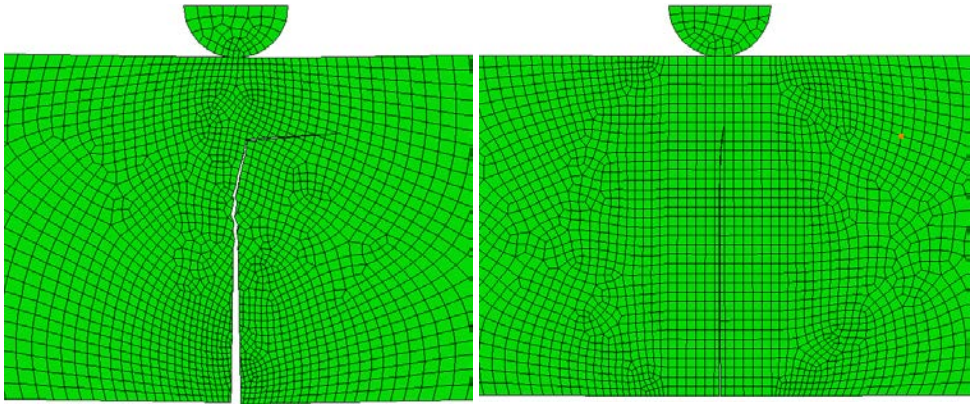

Figure B. 8: Simulated crack paths for size 1 graphite beam with unstructured (left) and structured (right) meshes.

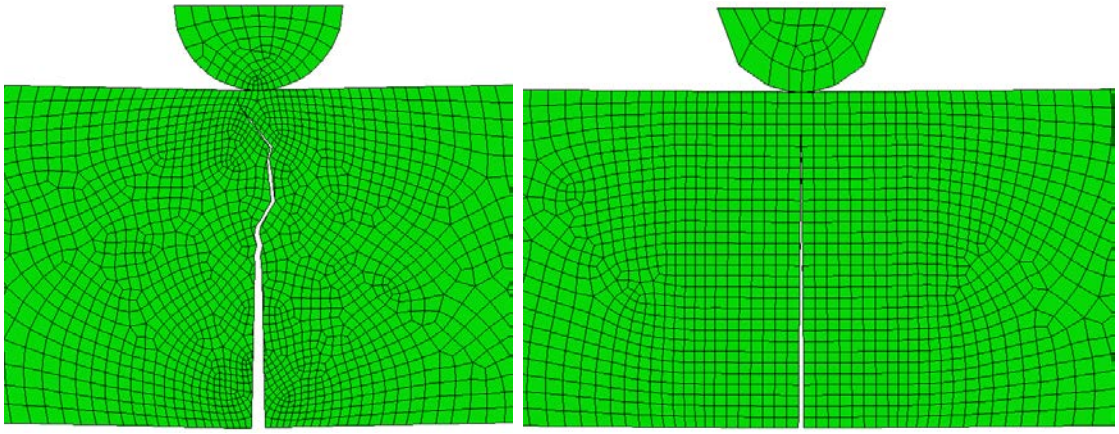

Figure B. 9: Simulated crack paths for size 2 graphite beam with unstructured (left) and structured (right) meshes.

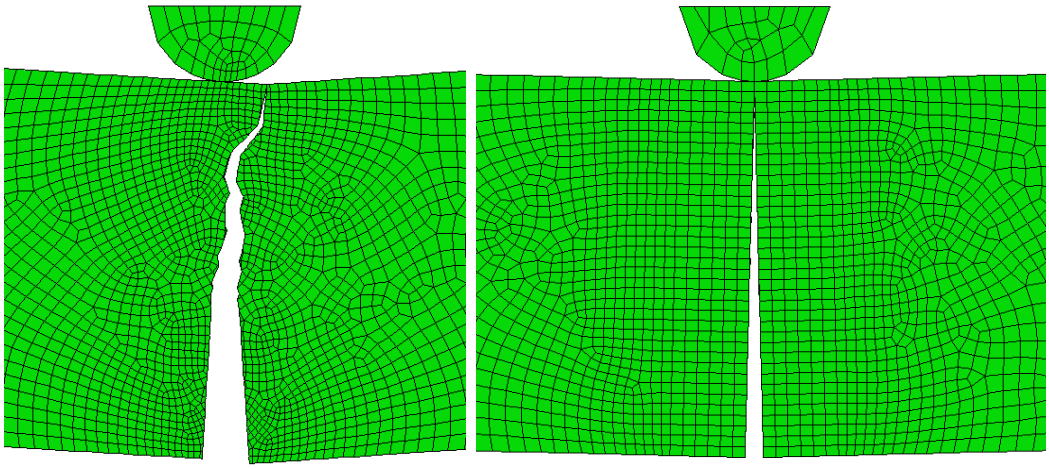

Figure B. 10: Simulated crack paths for size 3 graphite beam with unstructured (left) and structured (right) meshes.

Figures B.8, B.9 and B.10 show that the crack propagated mostly in a straight line with a structured mesh. While with an unstructured mesh the crack did not propagate in a straight path, especially when it approached the loading bar. For the size-1 beam, the crack turned its direction by about 70° with an unstructured mesh, while with a structured mesh there was only a slight change in the direction of the crack.

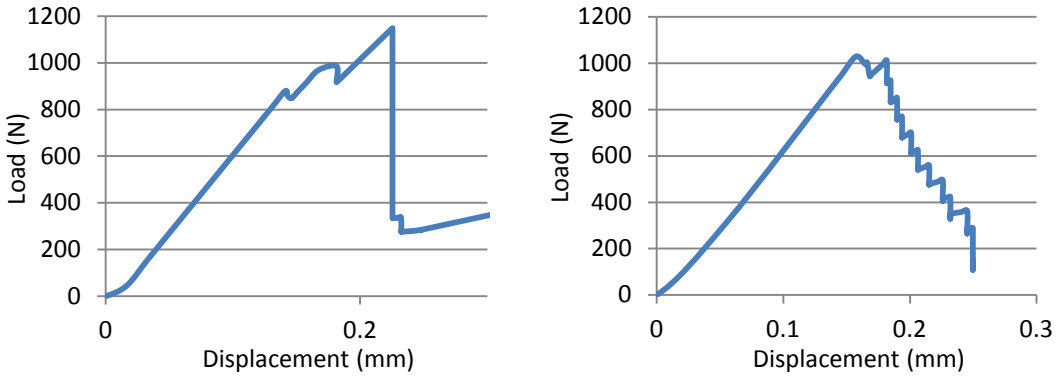

Figure B. 11: Load vs. loading bar displacement curves for size 1 graphite beam with unstructured (left) and structured (right) meshes.

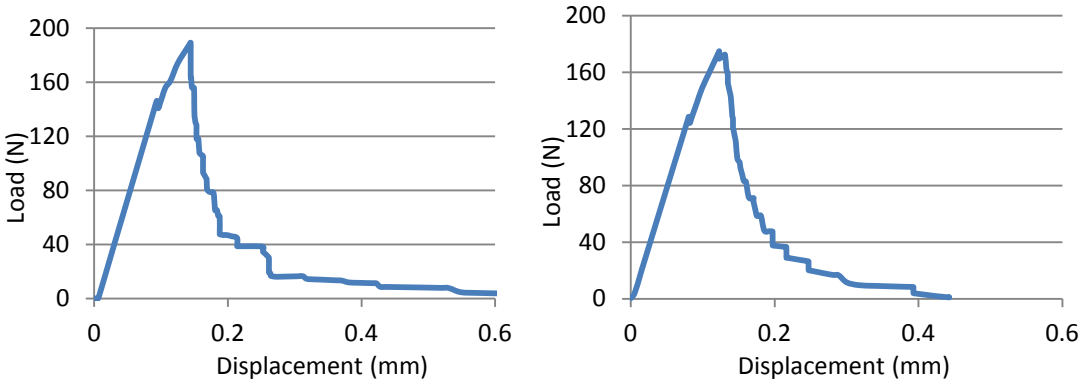

Figure B. 12: Load vs. loading bar displacement curves for size 2 graphite beam with unstructured (left) and structured (right) meshes.

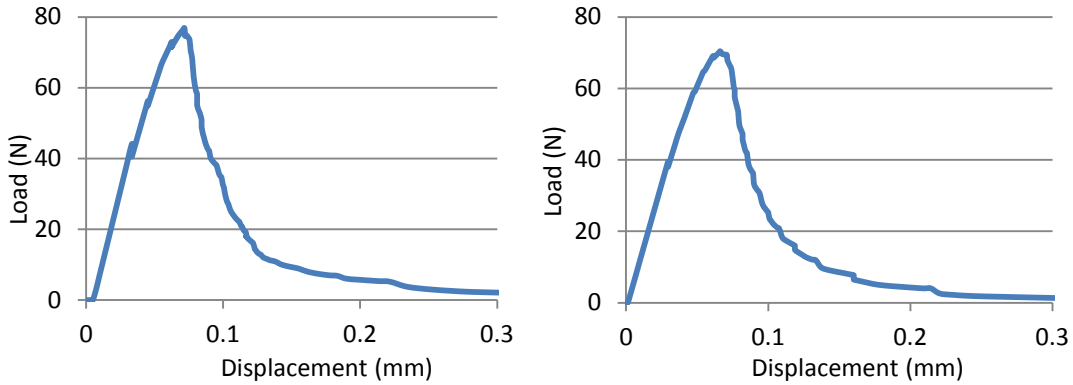

Figure B. 13: Load vs. loading bar displacement curves for size 3 graphite beam with unstructured (left) and structured (right) meshes.

Figures B.11, B.12 and B.13 show the load vs. loading bar displacement curves for all the three different sized graphite beams with structured and unstructured meshes. It can be seen that the pre and post-peak behavior of crack propagation is smoother with the structured meshes. For the size-1 graphite beam with an unstructured mesh, there is a second increase in the load within the post-peak region. This is attributed to the sharp change in crack path towards the horizontal direction (Figure B.8). For all the other cases, the post-peak behavior appears quite reasonable. The predicted peak loads and the corresponding errors, when compared with the experimental peak loads, for both types of mesh are shown in Table B.3.

Table B. 3: Experimental and computational peak loads and the corresponding errors.

	Experimental peak load (N)	Computational peak load (N)		Peak load error (%)	
		Unstructured mesh	Structured mesh	Unstructured mesh	Structured mesh
Size 1	1093	1148	1029	5.0 %	-5.9 %
Size 2	187	189	175	1.1 %	-6.4 %
Size 3	81	77	70	-4.9%	-13.6%

Table B.3 shows that for graphite beams with sizes 1 and 2, the peak load was over-predicted with the unstructured mesh and under-predicted with the structured mesh. For the size-3 graphite beam, the peak load was under-predicted with both types of mesh. The absolute % error was found to be smaller with the unstructured mesh.

Effect of mesh size

To understand the effect of mesh size on the behavior of crack propagation simulated with XFEM, three mesh sizes were considered and structured mesh was employed. Table B.4 shows the number of elements and element size in the middle region of the graphite beam for each of the beam sizes. In mesh2, the element size was about twice that inmesh1, and in mesh3 the element size was about four times the size in mesh1. Thus, mesh1 was finer than mesh2, and mesh2 was finer than mesh3. Figures B.14, B.15 and B.16 show the simulated crack paths with the three different meshes for beam sizes 1, 2 and 3 respectively.

Table B. 4: Number of elements for the 3 different sized beams using 3 element sizes.

	Number of elements in the graphite beam			**Approximate element size in the mid-region of the beam (mm)**		
	Mesh1	**Mesh2**	**Mesh3**	**Mesh1**	**Mesh2**	**Mesh3**
Size 1	6405	2910	970	0.71	1.42	2.78
Size 2	5843	2514	784	0.33	0.67	1.33
Size 3	6736	2719	991	0.14	0.29	0.56

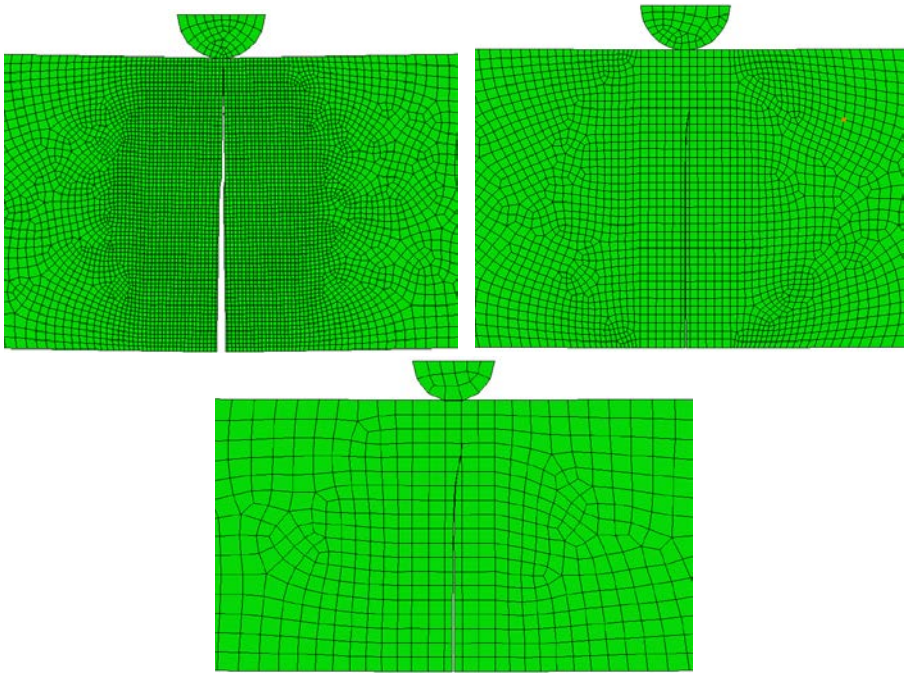

Figure B. 14: Simulated crack paths for size 1 graphite beam with mesh1 (upper left), mesh2 (upper right) and mesh3 (lower).

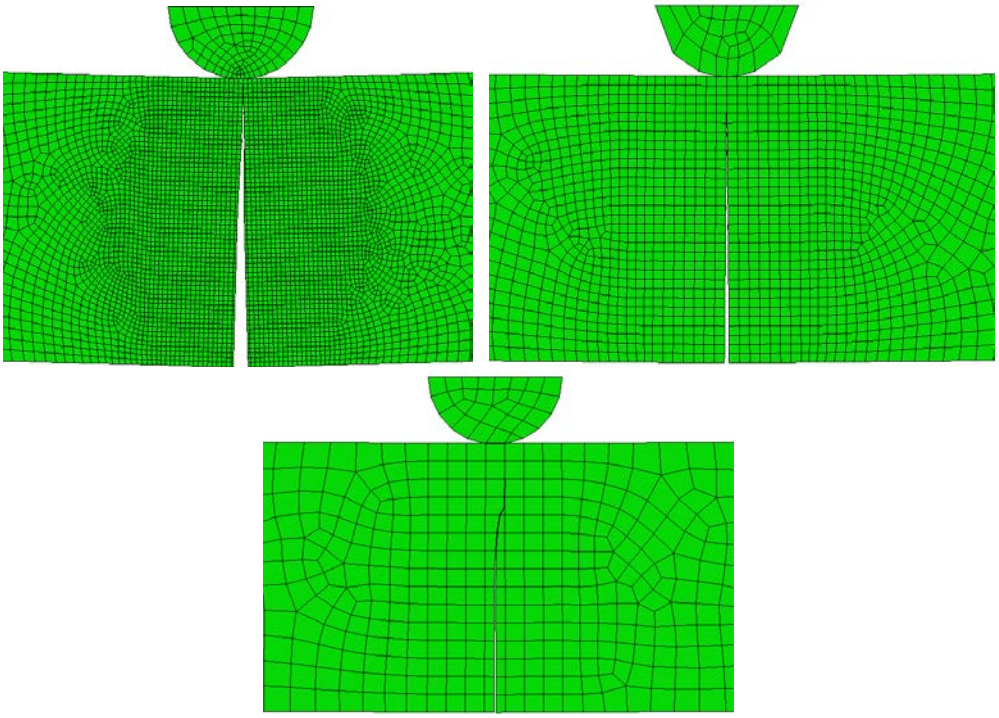

Figure B. 15: Simulated crack paths for size 2 graphite beam with mesh1 (upper left), mesh2 (upper right) and mesh3 (lower).

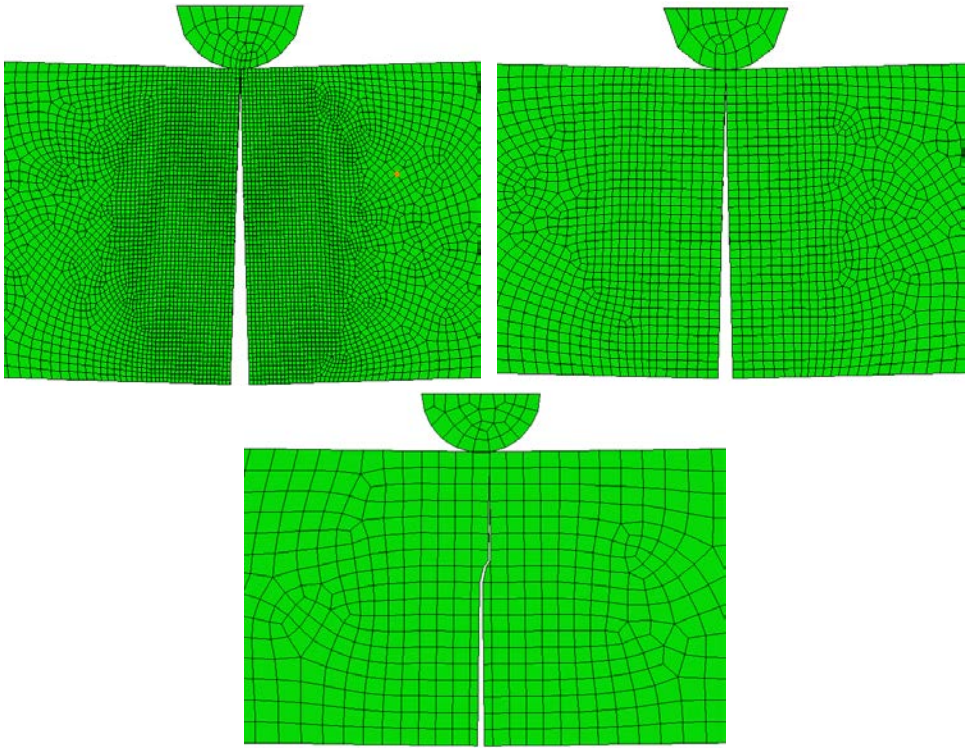

Figure B. 16: Simulated crack paths for size 3 graphite beam with mesh1 (upper left), mesh2 (upper right) and mesh3 (lower).

It can be seen from Figures B.14, B.15 and B.16 that the crack propagation directions were slightly changed in models with coarse meshes (mesh3). While with finer meshes (mesh1 and mesh2) the cracks propagated in an almost straight line.

Figures B.17, B.18 and B.19 show the load vs. loading bar displacement using the three types of mesh for beam sizes 1, 2 and 3, respectively. It can be seen from the figures that the load vs. loading bar displacement curves were smoothest for the finest mesh (mesh1) and the curves became jagged as the mesh coarsened. With mesh3, which was the coarsest mesh, the load-loading bar displacement was found to be most jagged.

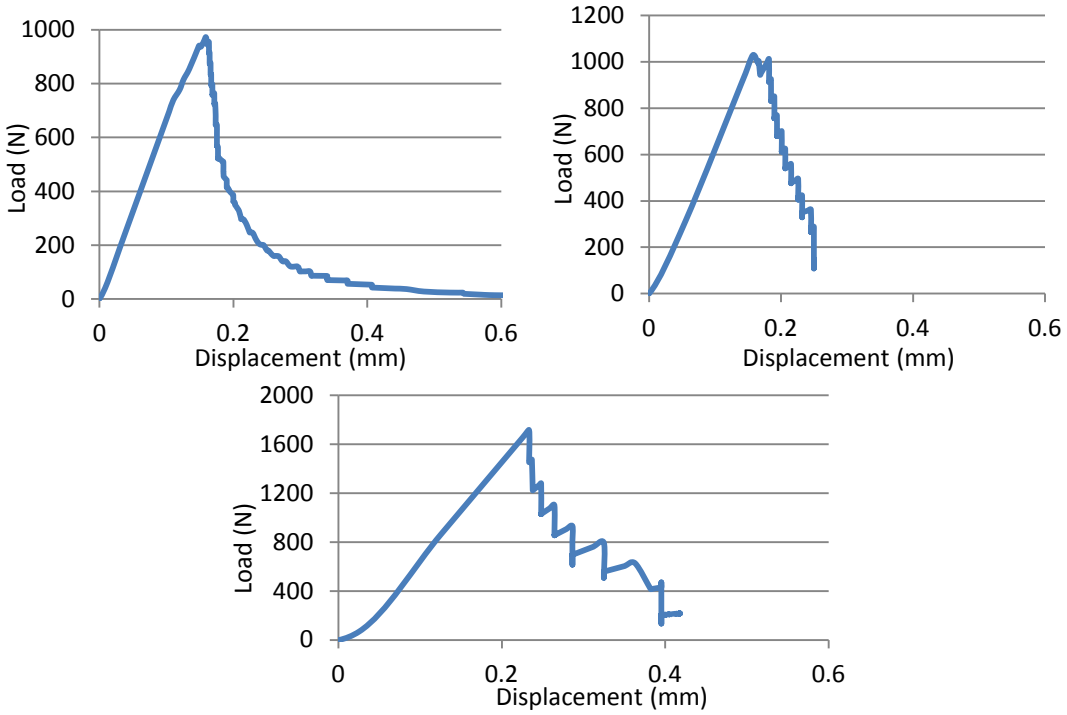

Figure B. 17: Load vs. loading bar displacement curves for size 1 graphite beam with mesh 1 (upper left), mesh 2 (upper right) and mesh 3 (lower).

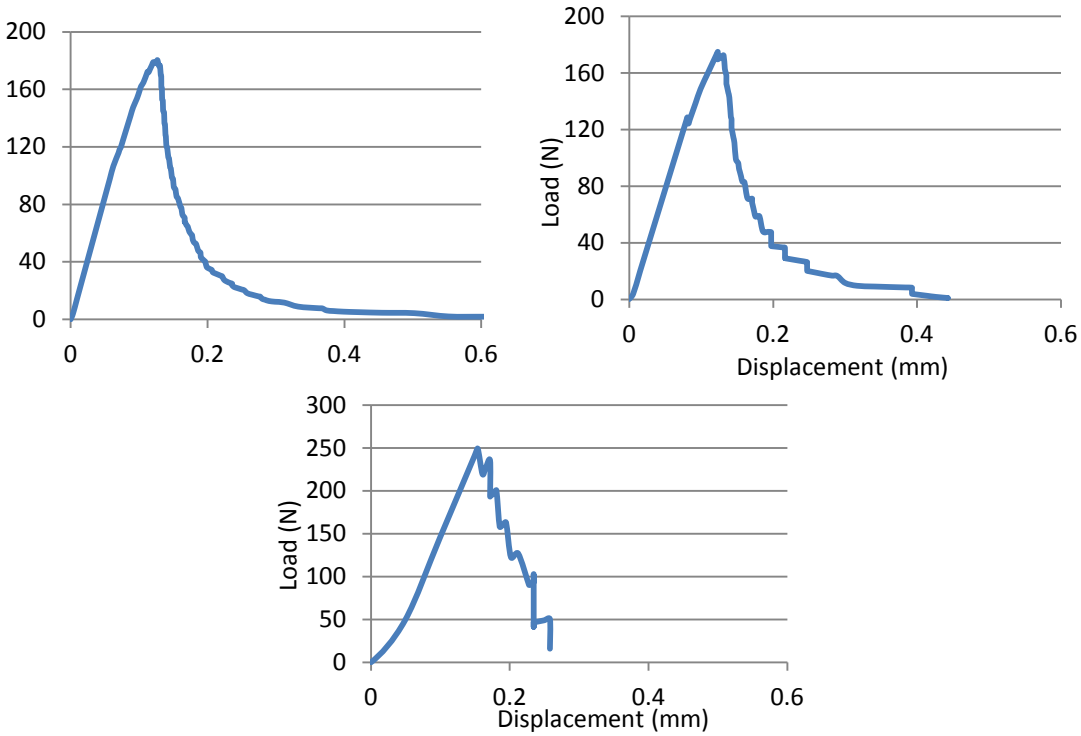

Figure B. 18: Load vs. loading bar displacement curves for size 2 graphite beam with mesh 1(upper left), mesh 2 (upper right) and mesh 3 (lower).

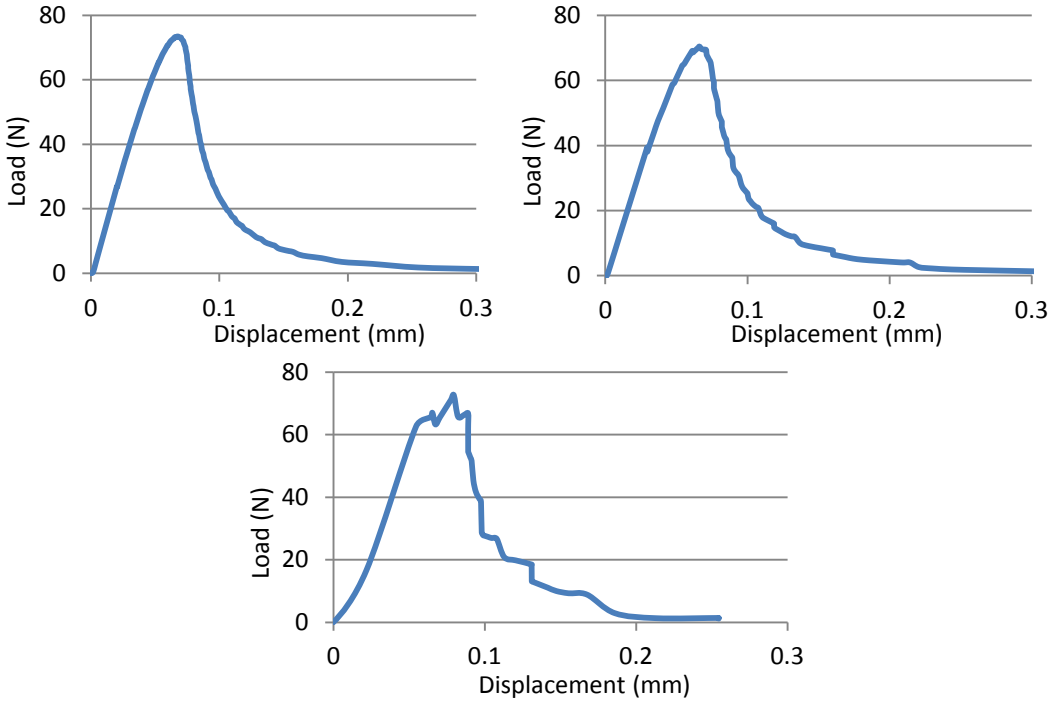

Figure B. 19: Load vs. loading bar displacement curves for size 3 graphite beam with mesh 1(upper left), mesh 2 (upper right) and mesh 3 (lower).

Table B.5 gives the experimental and predicted values of the peak load for beam sizes 1, 2 and 3 with the different meshes. For size-1 and 2 beams, the finer meshes (mesh1 and mesh2) gave much smaller % errors compared to the coarse mesh (mesh3). While for the size-3 graphite beam, the % error was similar among the 3 meshes. It can be concluded that a finer mesh is required to ensure the accuracy of XFEM crack simulation.

Table B. 5: Experimental and computational peak loads, together with the corresponding errors, for the 3 different sized beams using different meshes.

	Experimental peak load (N)	Computational peak load (N)			Peak load error (%)		
		Mesh1	Mesh2	Mesh3	Mesh1	Mesh2	Mesh3
Size 1	1093	972	1029	1716	11.1	5.9	-57.0
Size 2	187	180	175	249	3.7	6.4	-33.2
Size 3	81	74	70	73	8.6	13.6	9.9

Comparison with Experimental Results

Figures B.20, B.21 and B.22 show comparisons of numerically predicted load-displacement curves for the graphite beam models of three different sizes with the corresponding load-displacement curves found experimentally [6].

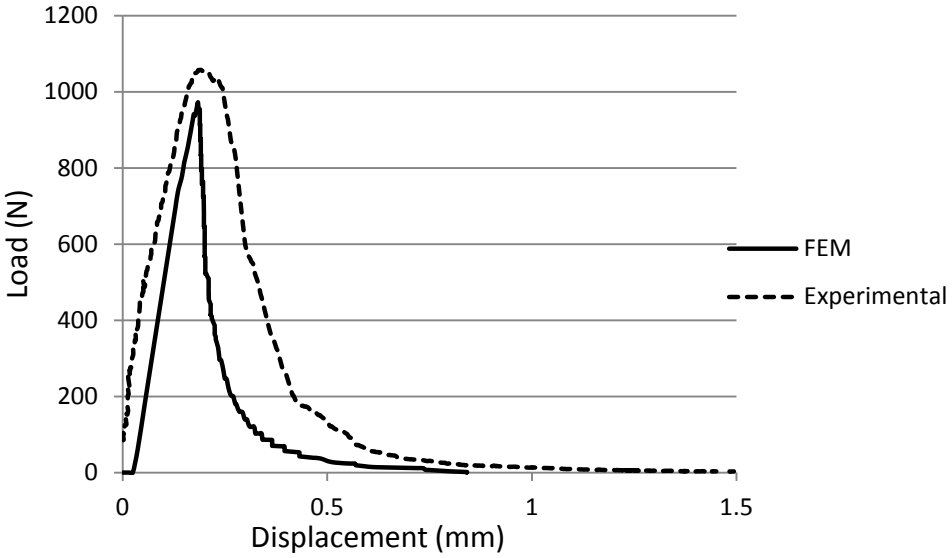

Figure B. 20: Experimentally observed and numerically predicted load-displacement curves for size-1 (largest size) graphite beam.

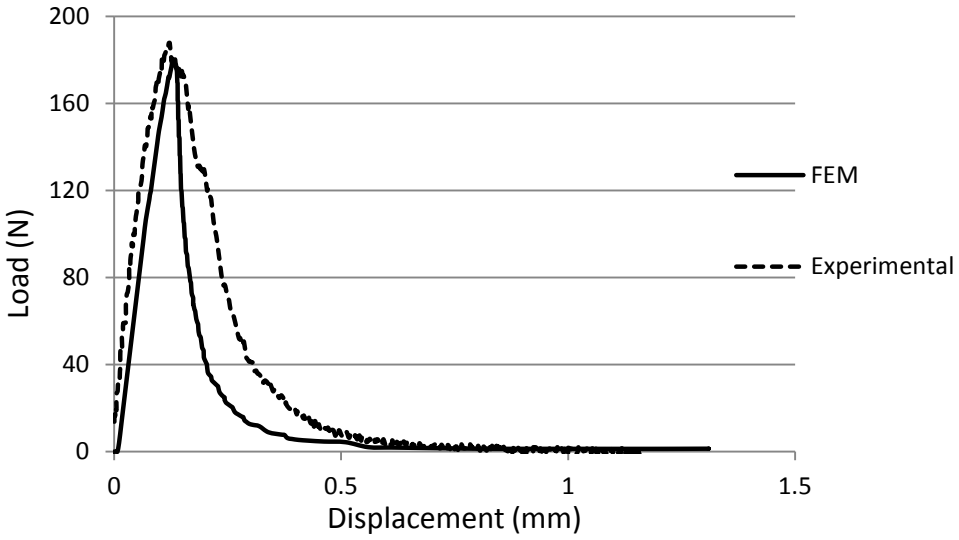

Figure B. 21: Experimentally observed and numerically predicted load-displacement curves for size-2 (mid-size) graphite beam.

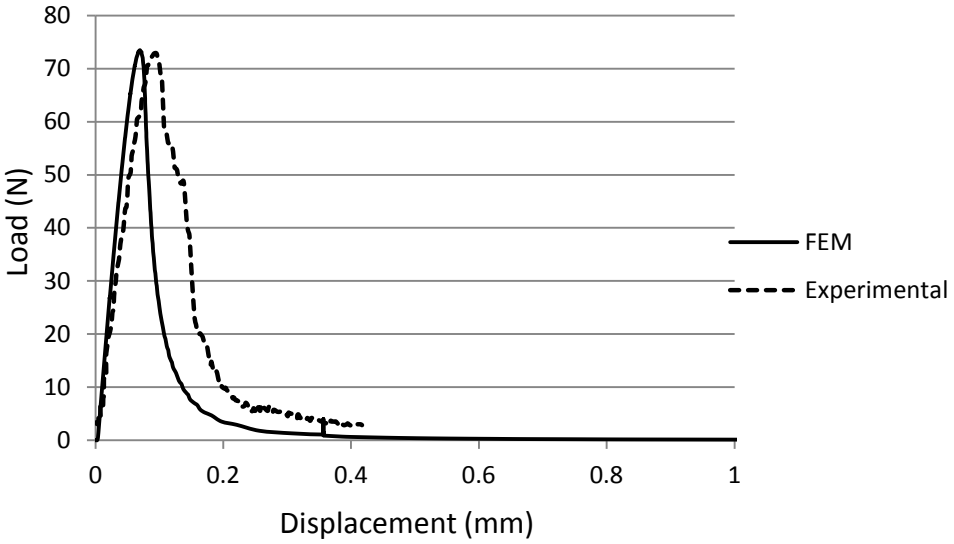

Figure B. 22: Experimentally observed and numerically predicted load-displacement curves for size-3 (smallest size) graphite beam.

Conclusions

By studying the beam under 3-point bending, it was found that the type of mesh affects the direction of the XFEM-predicted crack propagation. For a structured mesh the crack propagation was found to be more or less in a straight line, while for an unstructured mesh the crack changed its direction as it propagated. Also, it was found that the load-displacement curves were smoother with structured meshes. Thus, structured mesh led to more consistent results for simulation of crack propagation.

The effect of mesh size on crack propagation modeled by XFEM was studied. It was found that the load-displacement curves were smoother for the finer meshes (mesh1 and mesh2) compared to those for the coarse mesh (mesh3). The errors in peak load were also smaller for the finer meshes (mesh1 and mesh2) than for the coarse mesh (mesh3). However, the differences between mesh1 and mesh2 were found to be small, indicating that the solution had converged. This is an encouraging result considering that non-linear

problems such as fracture may not necessarily converge upon increasing the mesh density. Thus, XFEM was found to be a capable numerical technique for modeling failure in brittle materials.

B.4 REFERENCES

1. T. Belytschko, and T. Black, Elastic Crack Growth in Finite Elements with Minimal Remeshing, International Journal for Numerical Methods in Engineering, 45, 601-620, 1999.
2. J. Melenk, and I. Babuska, The Partition of Unity Finite Element Method: Basic Theory and Applications, Computer Methods in Applied Mechanics and Engineering, 39, 289-314, 1996.
3. Abaqus Documentation, Dassault Systemes Simulia Corp., Providence, RI, USA.
4. J. J. C. Remmers, R. de Borst, and A. Needleman, The Simulation of Dynamic Crack Propagation using the Cohesive Segments Method, Journal of the Mechanics and Physics of Solids, 56, 70–92, 2008.
5. J.H. Song, P.M.A. Areias and T. Belytschko, A Method for Dynamic Crack and Shear Band Propagation with Phantom Nodes, International Journal for Numerical Methods in Engineering, 67, 868–893, 2006.
6. H. Li, J. Li, G. Singh and A. Fok, Fracture Behavior of Nuclear Graphite NBG-18, Carbon, 60, 46-56, 2013.